H. H. Schwartz,

An Ion Tracer Technique for Measuring Air Velocities

Electrical Engineering SCHWARTZ, H. M.Eng.

ABSTRACT

An instrumentation method, belonging to the tracer technique class, is presented for the continuous measurement of supersonic air velocities. The air is periodically ionized by an alpha particle source and the 'flight time' of the ionized packet, between two fixed reference positions downstream from the source, is measured. The ions are detected, external to the airstream, by the induced potential on a capacitive transducer. The 'flight time' is determined electronically and recorded by a pulse width modulation technique. The ionization frequency determines the transient phenomenon that may be observed. Application of the measurement technique is demonstrated in an intermittent wind tunnel with a mach 1.8 nozzle. The instrument had a discrepancy of 5% relative to the standard method over a 1 inch measuring length.

INVESTIGATION OF AN ION TRACER
TECHNIQUE FOR THE MEASUREMENT
OF SUPERSONIC AIR VELOCITIES

by

H. H. Schwartz, B. Eng.

A thesis submitted to the Faculty of Graduate Studies and Research in partial fulfillment of the requirements for the degree of M. Eng.

Department of Electrical Engineering ,
McGill University,
Montreal, Quebec,
May, 1971 .

ACKNOWLEDGEMENTS

I would like to thank my Director, Dr. G. L. d'Ombrain, for suggesting this thesis problem, and who acted as my mentor throughout the work.

To Dr. J. H. T. Wu, the author is sincerely grateful for the extended use of the supersonic facilities, as well as his helpful comments.

My thanks to Dr. E. L. Adler and Mr. J. E. Michalski for their kind assistance in some of the editing.

A special acknowledgement is due to the Defence Research Board for their patience and financial support of this work.

I would also like to thank Mrs. P. Hyland for having started the typing of this thesis, and to my wife for completing the typing under the most adverse conditions.

TABLE OF CONTENTS

CHAPTER I

INTRODUCTION

1.1 General

In recent years considerable interest has been generated in extremely high speed flight, of the conventional and non-conventional types. This has led to a phenomenal increase in the number of research, developmental and test centers to carry out the necessary investigations relating to the characteristics of aerodynamic surfaces. Most of these investigations are carried out in a wind tunnel facility. The instrumentation required at these facilities for measuring fluid flow parameters, such as, pressure, temperature, etc., though much improved over the years, still leaves much to be desired with regard to accuracy, disturbance free measurement and dynamic range.[1,2,3,4] One such parameter of importance is the velocity of the gas. Ideally, the instrumentation for measuring gas velocities should be precise, disturbance free with infinite dynamic range and be independent of temperature, density and gas composition.

A survey of available methods indicates that the techniques employed generally fall into one of the following categories :

(a) Utilization of the gas stream's Kinetic Energy. The Pitot-Static tube is typical.[1,2,4]

(b) Utilization of Thermal Energy transfer. The Hot Wire Anemometer[1,2,5] is an example.

(c) Utilization of changes in propagating waves within the gaseous medium. The Acoustic Anemometer[2] is such a device.

(d) Utilization of Tracer Technique. Luminous particles, ions or radioactive gas would be typical.[2,6]

Considering the desired ideal characteristics of an anemometer for supersonic flow, it is obvious that the items listed in categories (a) and (b) can be eliminated for identical reasons, namely disturbance free measurement and dynamic range. For example, with the Pitot-Static System, the pressure probes project into the free stream and while being more suitable for localized measurements, create a disturbance in the flow field. Under certain conditions this imposes a severe limitation on their use. In particular, for a supersonic jet-stream shock waves are formed ahead of the probes and the velocity upstream will be higher than downstream, leading not only to disturbance in the flow pattern but also to measurement error. Furthermore, the Pitot-Static measurements are quasi-static and thus have a long response time.[1,4] This eliminates their use for observing the transient or high speed phenomenon found in these test facilities. Similarly, the Hot Wire Anemometer[1,5] requires the projection of a probe into the gas stream and has a relatively long response time. The third category can be dispensed with due to its temperature and density dependence. This leaves only the Tracer Technique as a valid avenue of investigation.

The purpose of the present investigation is to develop a method for measuring the velocity of a supersonic gas stream which is free from one or more of the above-mentioned deficiencies. That is, it should not require the projection of any probe into the flow field, it should not create any disturbance in the free stream but, it should be capable of larger dynamic range, and should be independent of temperature, density and gas composition. Having these objectives, it was decided to determine the feasibility of an Ion Tracer Technique for measuring the velocity of the gas and to develop this into a suitable research tool for basic gas dynamic measurements.

1.2 The Tracer Technique

There are numerous methods available which can be classified as Tracer Techniques in the measurement of velocity. However, each of these can be simply described as a 'time of flight' measurement involving only the following three basic items :

(A) The introduction into the stream of a 'tracer' element, assumed to acquire the same velocity as the fluid, or to be directly related to that velocity.

(B) The detection of this 'tracer' element as it passes each of two fixed stations separated by a distance, Δs .

(C) The determination of the time, Δt, taken by the tracer in traversing the distance between the two stations.

From the above, it is seen that the average velocity over the distance Δs is given by

$$U = \frac{\Delta s}{\Delta t} \qquad (1)$$

Item (A) above can be broken down into two distinct classes : (i) externally introduced foreign elements and (ii) externally controlled modification of a constituent element. Class (i) tracer elements, for example, radioactive gas, or luminous particles give rise to several problems. The two most formidable are the method of introduction to render them individually distinguishable from the actual gas, and the identification of their velocity with that of the host medium. This leads to class (ii) elements as the more suitable choice since the latter difficulty is automatically eliminated and the former easily overcome. Further, since it is desired to modify the constituent element, which already has the desired velocity characteristic, and since it is a gaseous medium, then the simplest method of tagging or modifying is by ionization.

The specific methods that can be included within the framework of 'Tracer Techniques' are the means by which A, B and C above-mentioned are accomplished. Applying the simple restriction that the tracer be an ionized constituent element, then Table 1 gives an outline of how each of A, B, and C can be

TABLE I

METHODS FOR GENERATING IONS, DETECTING IONS AND DETERMING TIME OF FLIGHT

	A	B	C
	Source of Ions	Detection of Ions	Determining Time of Flight
1.	Electrical Discharge	Collection of Charge	Pulse Delay on an oscilloscope.
2.	Electron Gun	Induction	Frequency Counter which is triggered on and off.
3.	X-Ray Gun	Gas Discharge Counters	Numerous Electronic Methods e.g. Modulation Techniques.
4.	Ion Gun	Ion Multiplication Devices	
5.	Radioactive Source α, β and γ Emitters	Optical Observation	
6.	Photoelectric Emission	Microwave Interaction	
7.	Thermionic Emission	Radiation	
8.	Microwave Breakdown of Gas	Doppler Shift of R.F.	
9.	Chemical Reaction		
10.	Ultraviolet Illumination		
11.	Laser Beam		

attained. If we combine only one element from each column, then Table 1 also indicates the various schemes possible. (11 x 8 x 3). For example, $A_2 B_2 C_1$ is a system incorporating an electron gun for ion generation, utilizes the induction principle for detection and the pulse delay on an oscilloscope for the time determination.

By various combinations of only A and B in Table 1 a considerable number of schemes (11 x 8) could theoretically be devised without including C, which obviously would offer a further multiplication to the number of methods. The work reported herein is limited to a system designated as $A_5 B_2 C_3$. A radioactive source produces the ions ; these ions are then detected by induction ; and the timing is determined by a modulation technique.

1.3 Previous Research

Mellen[7] and Lawrence[8] at the National Research Corporation have developed the methods utilizing the schemes $A_1 B_2 C_2$ and $A_1 B_1 C_2$ of Table 1. This system uses a spark source for the production of ions which is repeatedly triggered by the arrival of ions at the downstream station. The air velocity is then directly proportioned to the repetition frequency. More recently, Lienfeld et al[9] has utilized a system identical to Mellen and Lawrence's for practical measurements at high altitudes. Lawrence[8] reports further that the method employing $A_2 B_2 C_2$ had been tried and appeared to be particularly promising at low densities.

The work of Mellen and Lawrence was carried out under subsonic conditions and they speculated that it could be extended to supersonic flow. Obviously the inclusion of any probe or projection into supersonic flows is objectionable due to formation of shock waves which the discharge electrodes would create. Secondly, the discharge itself creates an extreme disturbance due to the very dense ionization taking place in a relatively large volume. Further, the induction detection scheme left wide latitude as to the exact arrival time of the ions. The dynamic range is limited by the discharge and readout schemes.

The methods designated as $A_1 B_1 C_1$ and $A_1 B_2 C_1$ have been described by Kunkel and Talbot[10] at the University of Calfornia Institute of Engineering Research. Their method involves the use of a probe - discharge for the generation of the ion tracers and two electrodes one inch apart as detectors. The detection methods were either ion collection or induction. The signals from the electrodes were displayed on an oscilloscope whose sweep was triggered by the pulse discharge. The separation of these signals as seen on the oscilloscope is the transit time of the ion cloud between the upstream and downstream electrodes. In this scheme as in the previous one, the necessity of having electrodes within the flow boundary imposes a severe limitation due to the disturbances created. The detection by induction even though attempted was not successful and was used for qualitative rather than quantitative results. As it is a single event display, it is difficult to quantitatively determine the velocity transient even through repeated discharges.

Cooley[11,12] at Massachusetts Institute of Technology, developed a technique that can be listed as $A_{1,5} B_2 C_1$. The source of ions is a corona discharge initiated by the passage of an α - particle near the tip of a positively charged electrode placed in the air stream. The ions are detected downstream by an induction probe. Here, the corona discharge is used to trigger the sweep of an oscilloscope and the output from the detector probe is then displayed as a delayed pulse. Cooley reports that the method is very good with accuracies of 2 % for a 1" measuring length at speeds of approximately 1700 fps. This scheme suffers from the same defect as the previous ones, namely, the inclusion of a probe within the flow boundary. Further, his claim of a 2 % accuracy in the mach 2 range is open to question since the results are based on the implied supposition of an average velocity throughout the test section, whereas the measurements were carried out in a specific measuring length having a different average velocity. Also, the measurement is somewhat irregular since it depends upon the singular chance of an α - particle travelling across the test section and coming sufficiently close to the tip of the discharge electrode to cause a corona burst. As with the others his readout scheme leaves much to be desired. For example, a time reference was not defined for the detected pulse. Cooley also attempted to use a radioactive α - emitter as his source but was unsuccessful in this endeavour.

Lawrence[8] and others, have attempted to use an electron gun for the generation of ions as a tracer element in velocity measurements. Very little has been reported of this investigation except its usefulness at very low densities. The electron gun certainly appears to be a fruitful avenue for investigation, except that it is only suitable for very low density tunnels due to the large beam dispersion at any pressure much above vacuum, and the high cost of the complete system.

Aside from the above-mentioned work which is of direct interest, Wright[13] at the California Institute of Technology used a method $A_5 B_1$- for the measurement of flame speed and turbulence in combustion studies. He suggested that a radioactive source could be used to generate ions as a tracer element for high velocity measurements, though his own work was at relatively low speeds.

1.4 Present Investigation

The present approach to the problems of measuring supersonic air velocities has been influenced by :

(i) the desire to have all the necessary instrumentation outside the flow boundary,

(ii) the necessity to exclude any radical disturbance within the flow field,

(iii) the requirement that the response of the instrument should be extremely fast.

With respect to (i) the imposition of this condition is necessary in order to eliminate the formation of shock waves with their detrimental effects whether the probes are included for either the production or detection of ions. Condition (ii) must be imposed for the same reasons as (i), but also, to limit any flow disturbance due to the presence of excessive numbers of ions. Since the gas velocities are high (supersonic) and in some instances of very short duration, the method must have incorporated within it a means of following rapid velocity fluctuations, which is Condition (iii).

A solution to the first requirement may be obtained by using an electrodeless ion source, e.g. radioactive source, electron gun, etc. As ionizing agents each of these may be placed outside the flow boundary. Similarly, the necessity of having the detector outside the boundary requires that the detector be of the induction type, for example, microwave interaction. For item (ii) a remedy would be to minimize the degree of ionization present, that is, by using a weaker source. The overall system should have a large bandwidth with good transient response in order to obtain a reasonable dynamic range.

The basic characterization of the measurement system under investigation is described in Chapter II. It serves as a unifying description to the component parts discussed in the succeeding chapters. Chapter III deals with the various aspects associated with ion generation, such as, the source, its form and the physical processes involved. The mechanism whereby the ions are detected is discussed in Chapter IV. The circuitry for the detection and timing is given in Chapter V. The experimental arrangement and results are left to Chapter VI. Chapter VII is the concluding chapter.

CHAPTER II

THE MEASUREMENT TECHNIQUE

2.1 General

This chapter, intended as a broad outline of the method for measuring air velocity, has two objectives; to present the principle of operation and the basic error analysis of the system. The first allows the reader to place the balance of the work in its proper perspective, and the second indicates the reasoning and necessity for the particular direction taken and the basic limitations of the technique.

2.2 Principle of Operation

Referring to Figure 2.1, the airstream whose velocity is to be determined flows in a non-conducting cylindrical structure. A collimated beam of alpha particles is projected across the air perpendicular to the flow direction. The beam is periodically interrupted by a rotating shutter external to the flow. Each burst or pulse of alpha particles injected into the flow ionizes the air in the immediate vicinity of their path. The ions,being an integral part of the air flow, then proceed downstream with the velocity of the gas towards the detectors.

The detectors are thin silver rings deposited upon the insulated tube wall together with a surrounding grounded metal shield. A polarizing voltage exists between the ring and shield supplied by the preamplifier. As the ion pulse

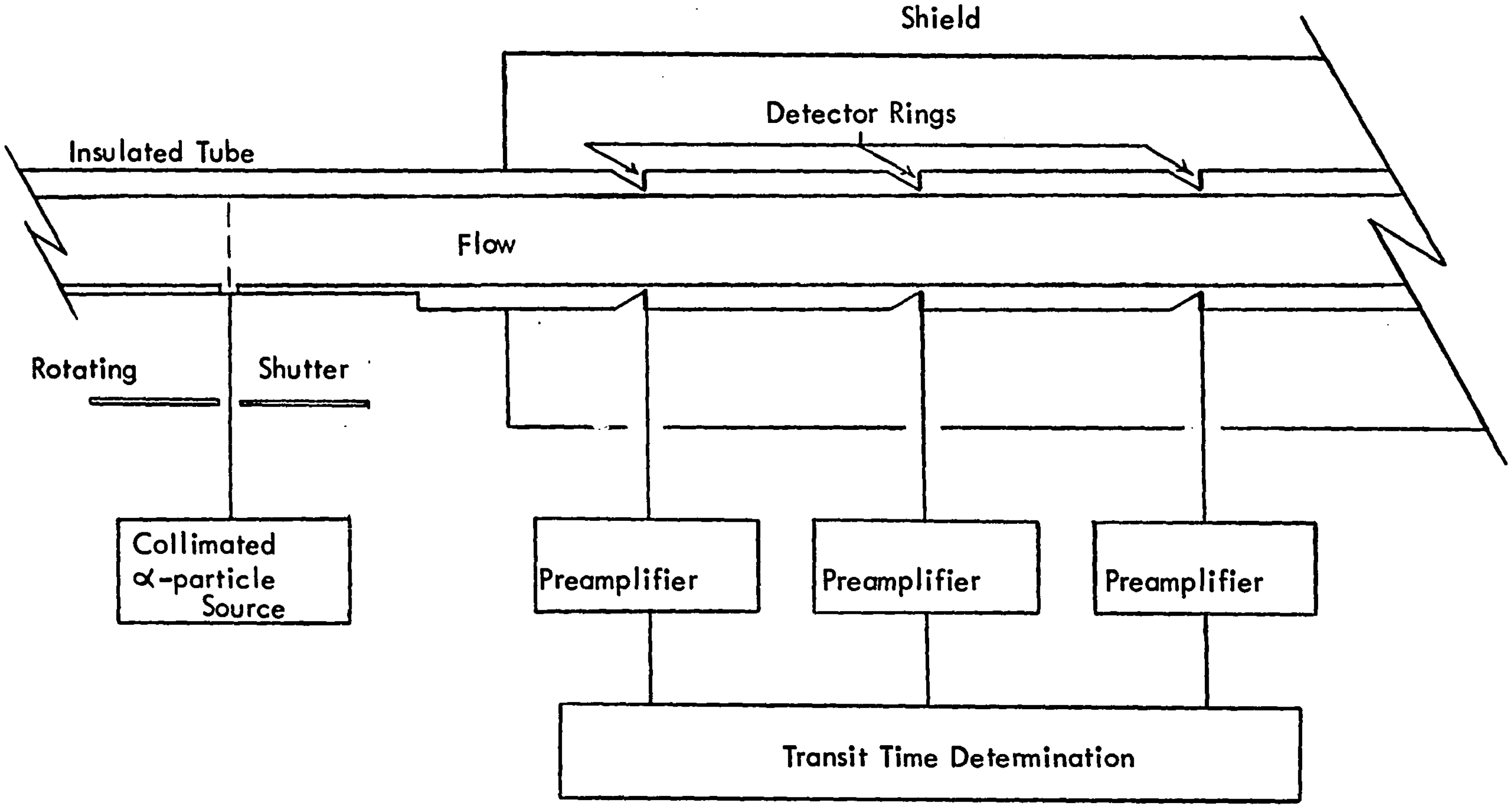

FIGURE 2-1 GENERAL SCHEME

approaches toward and recedes from a particular ring, a voltage pulse is generated between the ring and the shield. These same ions, at some later time, then generate a similar pulse in the adjacent downstream detector. This voltage pulse is measured and amplified by the preamplifier. It then goes to the transit time determination circuitry.

Considering the chronological order of events of a single ion cloud from the time it approaches the first ring to the time it recedes from the second ring, the following results. The ions, upon approaching the first detector, induce a voltage into it which is amplified, shaped and then triggers a bistable switch. At some later time, the ion transport time, a similar pulse induced in the second detector with identical circuitry causes the bistable switch to return to its initial state. This sequence of events occurs repetitiously at the interrupting frequency of the alpha particle beam. Consequently, the duration of the '1' state of the switch is the transit time of the ions over a known fixed distance. Hence, the output from the bistable switch is a series of pulses, whose width is the ion transit time and whose frequency is the injection frequency of the alpha particles.

The pulse train is now passed through a low pass filter for demodulation. The demodulated signal is amplified and recorded by a chart recorder. The general arrangement is shown in Figure 2.2 for two measuring stations, also the corresponding waveforms are indicated.

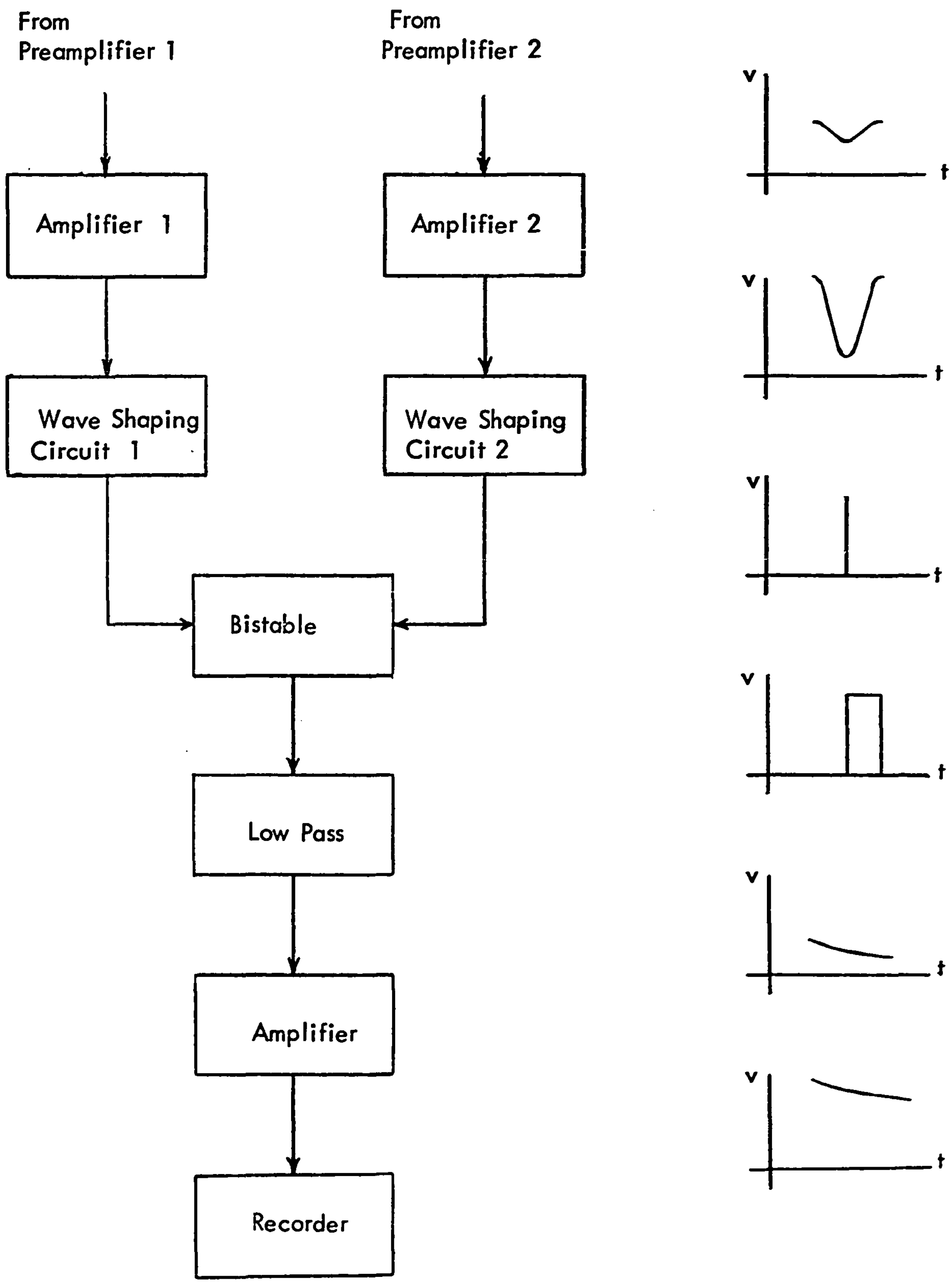

FIGURE 2-2 BLOCK DIAGRAM OF CIRCUITRY

2.3 Error Analysis

2.3.1 Digital System

Consider an idealized velocity measuring system in which α-particles are used as a source of ions. An ion pulse train is generated in the flowing air as follows : An α-particle beam allowed to project perpendicularly across the airstream creates ions within it. In order to obtain an ion pulse this beam is interrupted periodically. The selection of this interrupter is quite critical. It depends upon two main factors. The first and perhaps the more important one is the interrupting speed, and second, the frequency with which it is carried out. Upon the first depends the essential accuracy of the method, whereas the second determines the sampling rate.

Let us assume that the following conditions prevail in this idealized system :

(1) The free stream velocity, U is constant.

(2) The air stream has the ion concentration, n, illustrated in Figure 2.3 generated as described above.

(3) The ion pulses Figure 2.3 are an integral part of the air, having the same velocity.

(4) The ion concentration is completely unaffected by diffusion, recombination, and coulomb or other forces are negligible.

(5) Downstream from the ion formation point several ideal detectors are placed. By ideal is meant they are of infinitesimal size, and

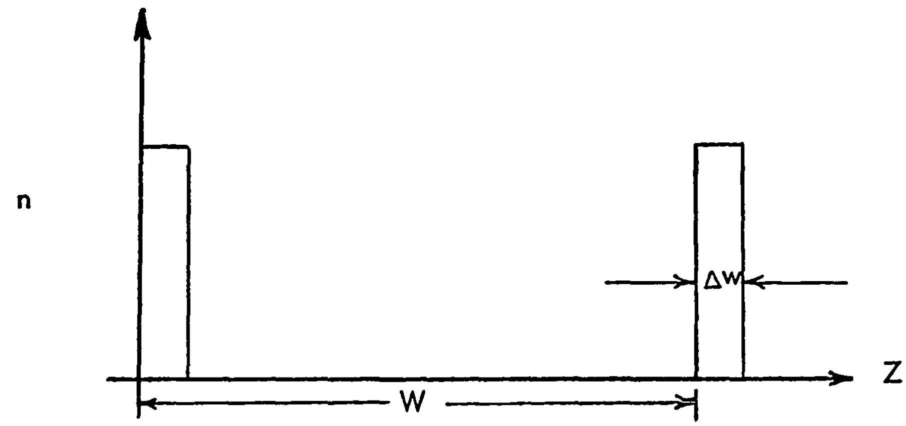

FIGURE 2-3 AIR STREAM ION CONCENTRATION

their output at any time is directly proportional to the ion density existing within the plane of the ring detector.

If provision is made for observing the output from these detectors as a function of time, then it would appear as shown in Figure 2.4 for the propagation of one pulse past three such detectors. The waveform shown is a qualitative picture of the ion density, as the detector output is directly proportional to the density. Also, under the ideal conditions assumed it is an exact replica of the α-particles injected. The transit time, T_i, the time taken for the ion cloud to travel from detector i to the $i + 1^{th}$ one is given by

$$T_i = \frac{L_i^{i+1}}{U} \tag{2-1}$$

where L_i^{i+1} is the distance between the detectors and U is the air velocity.

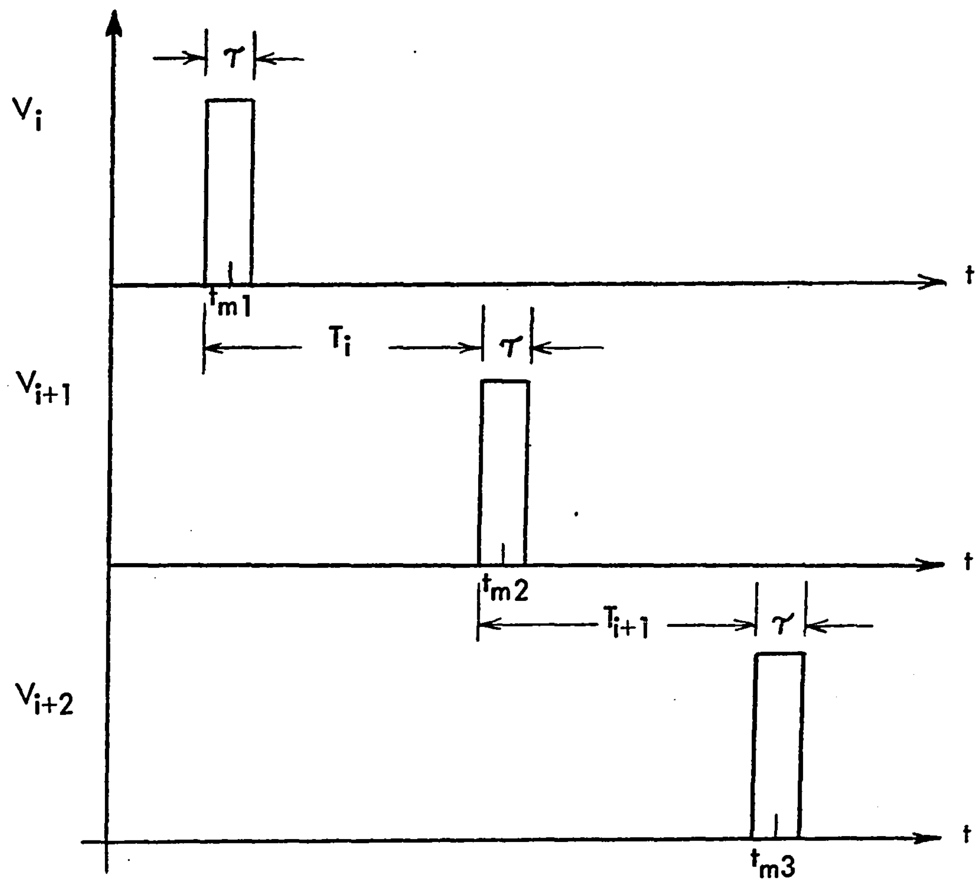

FIGURE 2-4 OUTPUT FROM IDEAL DETECTORS

The output of any detector is concentrated within the time interval

$$t_m - \frac{\tau}{2} < t < t_m + \frac{\tau}{2} \tag{2-2}$$

where t_m is the time at which the ion cloud is exactly centred in the detector ring and τ ($\tau = \Delta w/U$) is its width. That is, τ is the exposure time of the air to the a-particle beam. Obviously, a suitable reference time would be either the leading or trailing edge of the detector output. The error then would be twice the resolution of this reference time. However, if one uses digital detection, that is, the presence or absence of ions, then the possible error in measuring T_i, is τ. This digital approach being relatively simple could only be used if τ were negligible compared to T_i. The significance of the last statement is that one uses short shutter times or long measuring lengths in order to obtain a reasonable degree of accuracy. For example, if T_i is 100 μs and the desired accuracy is 1 % then the shutter opening should be 1 μs.

If the detectors are less than ideal, which is the usual case, then the output is concentrated in the interval

$$t_m - \frac{\tau}{2} - \frac{\Delta l}{U} < t < t_m + \frac{\tau}{2} + \frac{\Delta l}{U} \tag{2-3}$$

assuming that the detector reacts to the net ion density in its immediate vicinity, and Δl defines the influence distance of the detector. Only at t_m is the output at a maximum having the possible waveform illustrated in Figure 2.5. For the digital scheme, the error in T_i would be

$$\text{error} = \pm 2\left(\frac{\tau}{2} + \frac{\Delta l}{U}\right) = \pm 2\left(\frac{\tau}{2} + \tau_l\right) \tag{2-4}$$

In order to minimize this error both τ and τ_l should be negligible compared to T_i. Both of these are parameters of the system, the first associated with the shutter and the second with the detector. If τ_l is 0 then τ, the shutter time could be obtained from the desired accuracy as above. τ is a controlled parameter whereas τ_l is a fixed parameter.

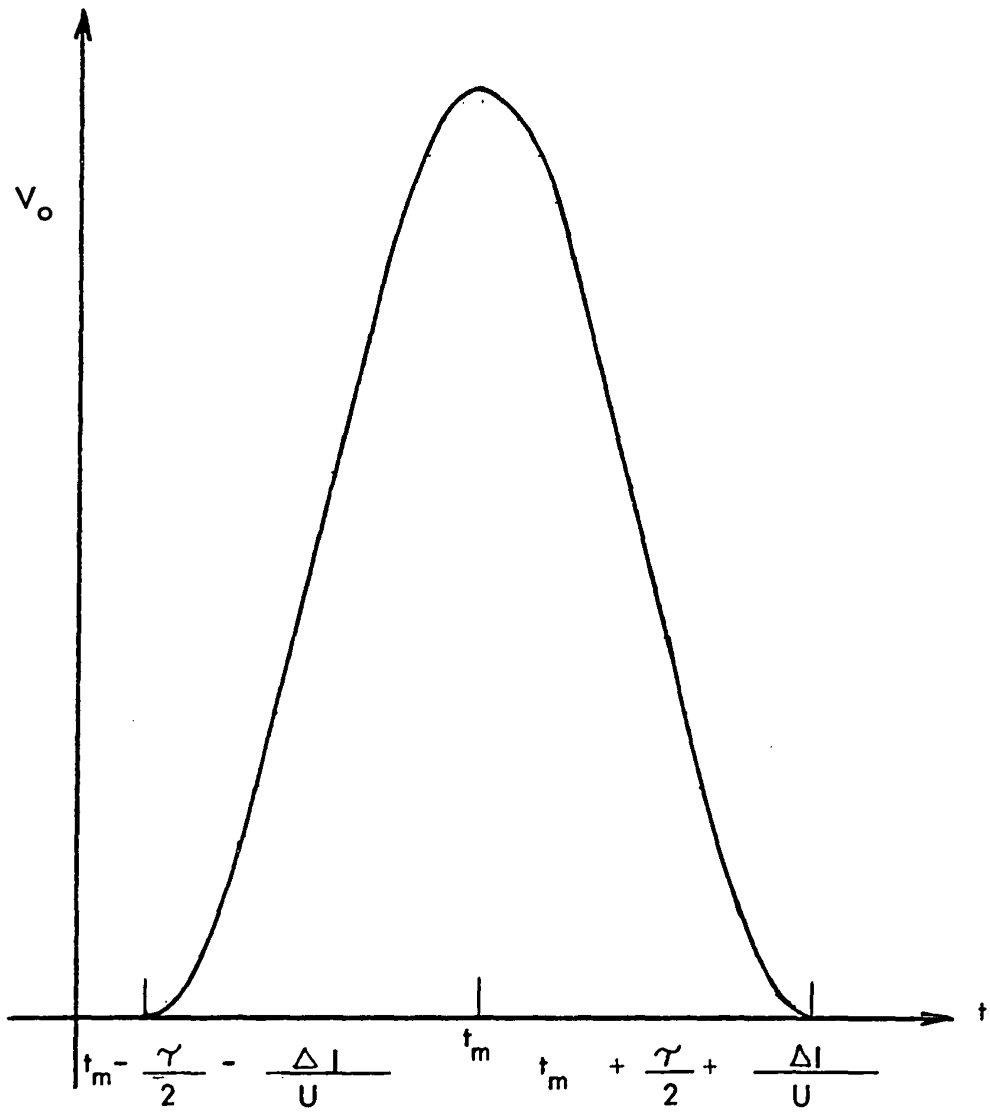

FIGURE 2-5 OUTPUT FROM NON-IDEAL DETECTOR

The range of transit times for various velocities, with measuring length as a parameter, is shown in Figure 2.6. It is readily apparent from Figure 2.6 that an extremely fast shutter is necessary for a short (1") measuring length and small error (1%). Unfortunately, the electromagnetic methods of shuttering would require prohibitively large fields. This leaves only the mechanical means for which the most suitable dimensionally is a dental turbine. The particular turbine selected had the capacity to rotate a one inch diameter disc at 4,000 R.P.S.

The inclusion of a shutter precludes the possibility of obtaining the ion concentration in Figure 2.3. The actual computed ion density distribution is shown in Figure 2.7 for several typical experimental values of K, the ratio of air to shutter speed. The derivation is given in Appendix I. From Figure 2.7 it is seen that the maximum concentration increases with decreasing K, or, decreasing air speed as the shutter speed is constant. The higher the air speed, the wider is the distribution. It should be noted that the K=15 and K=20 distributions are amplitude normalized with respect to K=10, thus the K=15 and 20 values are scaled by $T_e(15) / T_e(10)$ and $T_e(20) / T_e(10)$ respectively. Hence, if the air velocity is kept constant and the shutter speed varied, then the maximum concentration for all three K values is approximately the same. For K=20, the distribution is 43 m.m., or 108.5 μs (U=1300 f.p.s.) wide. Thus, the application of digital detection to such a waveform is impractical. Therefore, waveshaping circuitry was necessary to define a suitable reference measuring point - the peak of the ion concentration. This peak point is now associated with the arrival time t_m in the measurements.

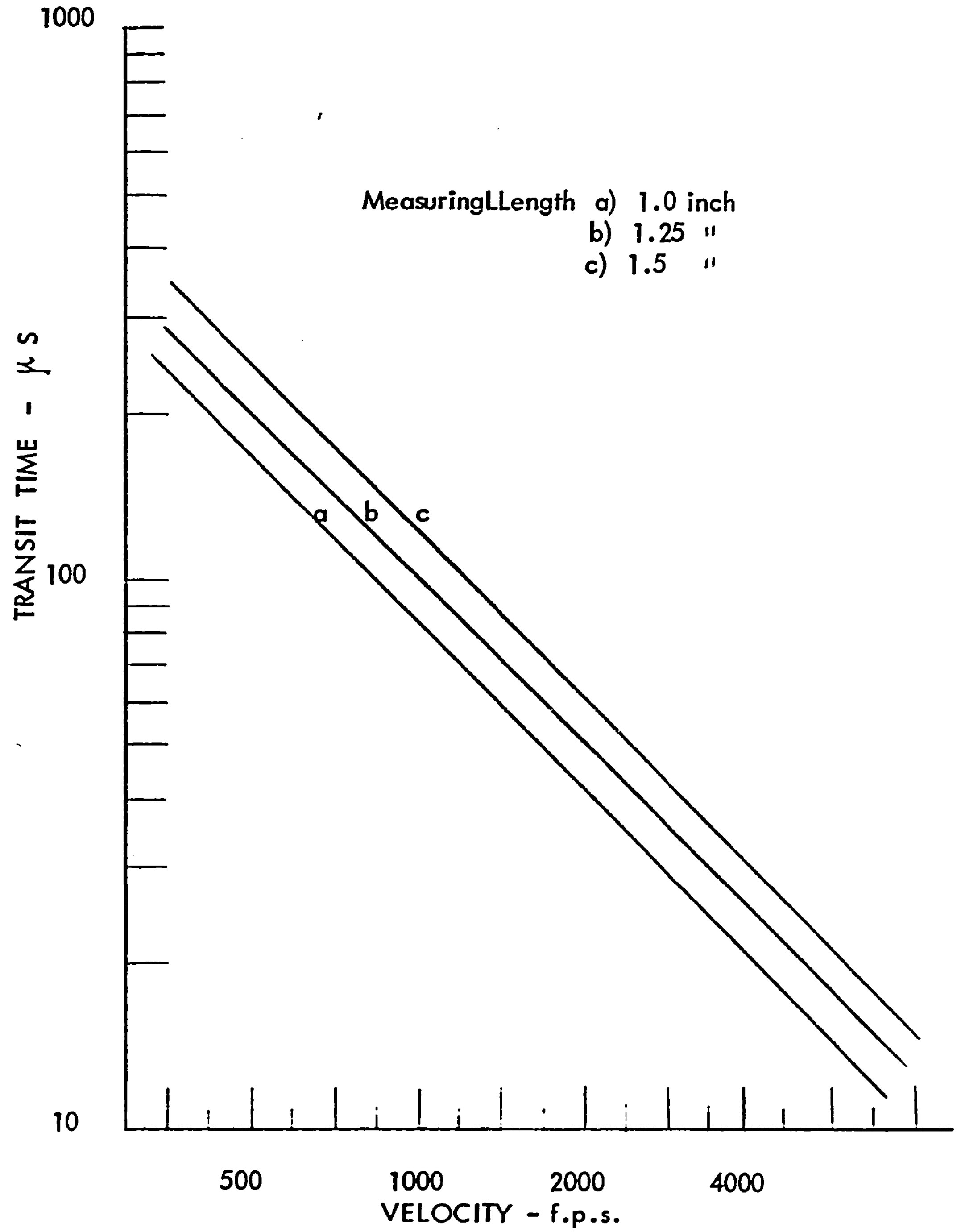

FIGURE 2-6 RANGE OF TRANSIT TIME

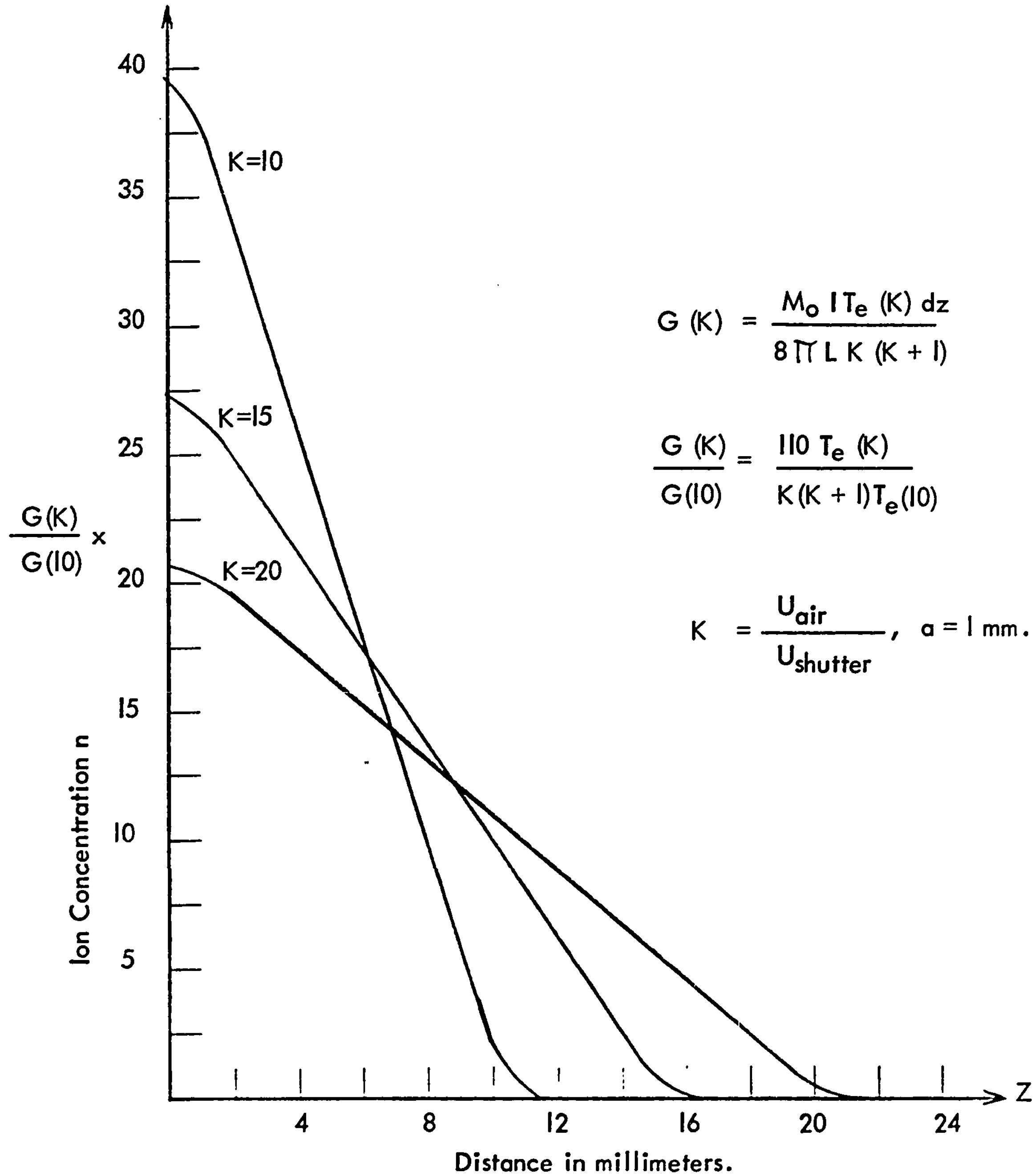

$$G(K) = \frac{M_o \, I \, T_e(K) \, dz}{8 \pi L K (K+1)}$$

$$\frac{G(K)}{G(10)} = \frac{110 \, T_e(K)}{K(K+1) T_e(10)}$$

$$K = \frac{U_{air}}{U_{shutter}}, \quad a = 1 \text{ mm.}$$

FIGURE 2-7 ION DENSITY DISTRIBUTION IN AIR

2.3.2 Velocity Effects

The main problem of interest here is to measure the velocity field. It is usually found that the velocity, to a greater or lesser extent, is a function of position in most test facilities. The possible effect of such a velocity field on the Ion Tracer Technique is twofold: It can effect the ion pulse fidelity during transport, thereby causing a relative shift in the defined reference, located at the peak ion density. The tracer technique gives the time average velocity, whereas the velocity required is the space average.

A graph showing the velocity as a function of position for the system under investigation is shown in Figure 2.8. The velocity continuously decreases in the flow direction. Its effect on the ion pulse density distribution would be to continuously reduce the width and simultaneously increase its amplitude such that the total number of particles in any section is conserved. As a direct consequence, the reference peak point has a relative shift. Appendix II examines this effect and shows the relative shift to be

$$z = -H^2 T\, b^2 / 2U \qquad (2\text{-}5)$$

and negligible for the experimental values.

Similarly, Appendix II shows that the difference between the time and space average velocity is negligible, being of second order.

It would thus appear that this type of measuring system is particularly attractive for use in such test facilities. The accuracy is only limited by the resolution of the peak ion density arrival time.

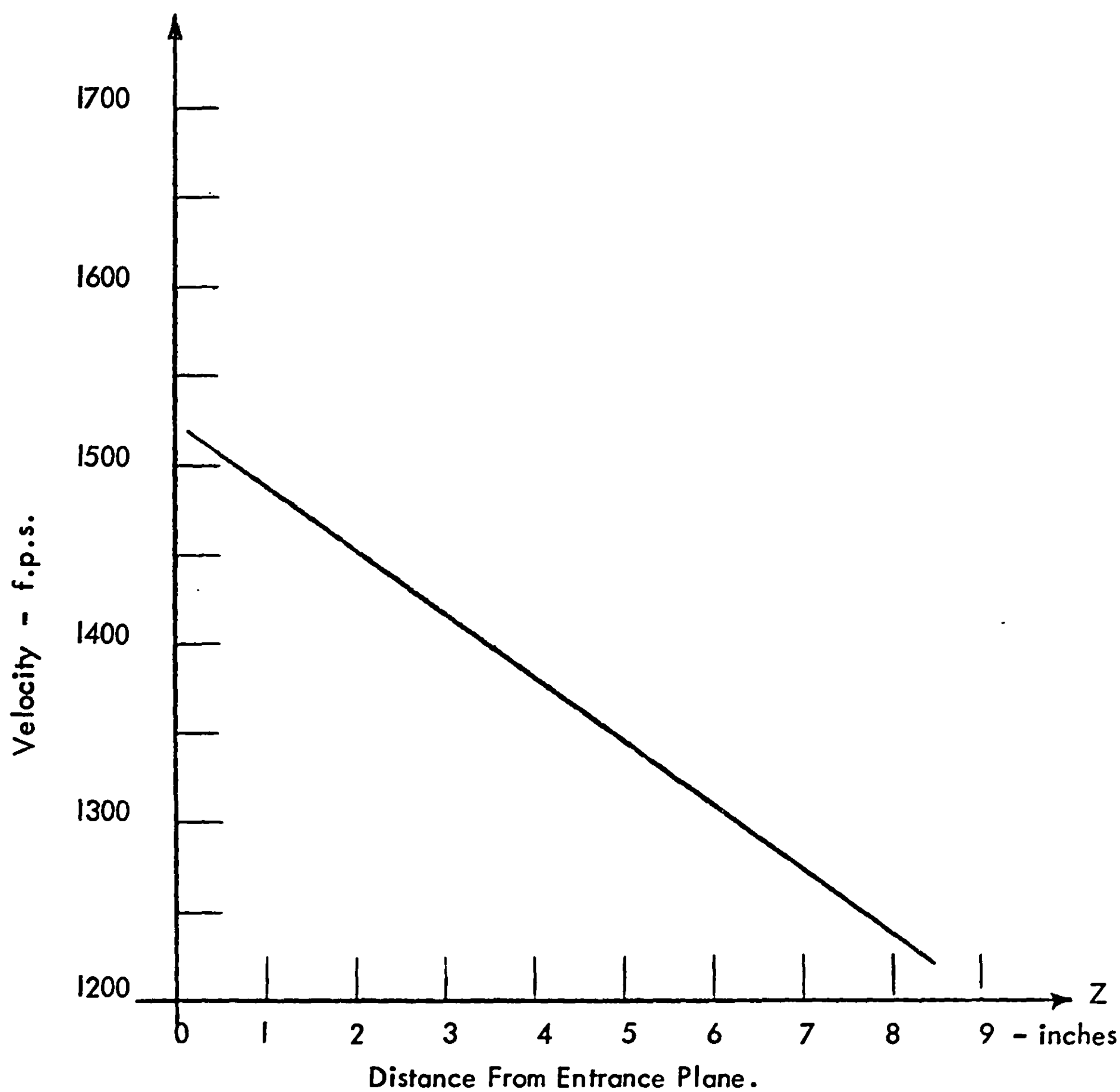

FIGURE 2-8 VELOCITY IN THE TEST SECTION

CHAPTER 111

ION GENERATION

3.1 General

This chapter is devoted to the detailed analysis of ion generation and the suitability of ions as a tracer element. In the course of this examination, it is necessary to consider the physical processes involved which have an ordered structure. The arrangement of the topics follow this order. It begins with the means of ion production, it then deals with the actual creation of ions, and lastly, the processes of diffusion, attachment and recombination are considered.

3.2 Ion Production

3.2.1 The Source

The means whereby ions can be produced are listed in Table I column A. The selection of a particular method from this list is governed by several factors, some of which have already been stated such as; it should be electrodeless, capable of producing sufficient quantities of ions at medium gas densities, readily available, of reasonable size and complexity and economically viable.

In view of these requirements it is readily apparent that the discharge technique is unsuitable. The electron, x-ray and ion guns are similarly eliminated, the first because it operates at low densities, the second for its low ionization cross-section, and the third, together with the first and second, for size, complexity and cost. Photoelectric emission, thermionic emission, chemical reaction and ultraviolet illumination all have too low an ion production rate. Microwave techniques are unsuitable as they produce fully ionized gases in fairly large volumes. The laser, on the other hand, is probably the most attractive method; it can produce sufficient quantities of ions in a localized volume and it is electrodeless. However, at the outset of the present investigation the laser was not available. This leaves the radioactive sources, of which there are α, β and γ emitters. The β and γ emitters not only have low ion production rates but also require considerable shielding. Thus the best source for creating ions is a radioactive α-emitting type.

There are numerous alpha particle emitters in the collection of radioactive substances. At present, approximately one hundred alpha emitting elements are known, some of which are found naturally, and the others are artificially produced. From these, the element Polonium 210 was chosen as the source of alpha particles. The selection of Po-210 was made on the basis of energy, half-life, purity, availability in sufficient quantity and well established properties.

According to Jesse, et al[14] for ionization, it is desirable to use α-particles whose energy is in excess of 5 mev. The reason cited is that the average energy W required to create an ion pair in air is not constant for α-particles having an initial energy less than 5 mev. Since W is not constant, this would add an undesirable nonlinearity. Furthermore, the range of the alphas, which is integrally related to the energy, must be sufficient in order to traverse the test section, or alternatively, penetrate sufficiently into the air stream to enable a meaningful measurement to be taken. In the present experimental setup the maximum width of the test section is 0.615" (1.56 cm.), consequently, the range should exceed 1.56 cm. which is the case for alphas having an energy in excess of 5 mev.

Perlman, et al[15] in their Systematics of Alpha-Radioactivity list 79 α emitting nuclides. According to their Table 111, 14 of these do not meet the minimum energy requirement stated above. The remaining 65 have sufficient energy but various half-lifes. If the source selected is to have practical application, it must have a sufficiently long half-life. Otherwise, considerable time and effort will be consumed in ensuring the source activity. Hence an arbitrary cut-off was considered as one month, which reduces the number of nuclides available to 45.

In the remainder, it is found that some emit β and γ as well as α-particles. Though the emission of small quantities of β and γ may be tolerated from the ionization viewpoint (negligible ionization) they should be avoided due to the radiation hazard. This further reduces the list to 29. Now, applying a more rigid boundary, the accessability of sufficient quantities, then the list is almost exhausted. The final selection of Po-210 as a source from the few remaining was made on the basis of its well known properties.

The properties of Po-210 have been established and have been catalogued(16)(17), (18), since its discovery by Madame Curie. It decays to lead upon the emission of an alpha particle with a disintegration constant of 5.80×10^{-8} (sec.$^{-1}$) giving a half life of 138.3 days[19]. The alpha is emitted with a velocity of

1.6×10^7 m/s and an energy of 5.3 mev. having a mean range of 3.83 cm. in air at ntp[20]. The alpha particles emitted from this source travel in straight lines to essentially the end of their range, at which point they might deflect slightly. This is well illustrated in the Wilson cloud chamber photos of Rutherford, et al[21]. For all practical purposes they are not deflected by a moving airstream of 16 00 fps. as their own speed is very high, 1.6×10^7 m/s.

Initially, a standard Po-210 source of 100 mc. was used. This source was in the form of a disc of 7 mm. active diameter contained in an aluminum holder, covered with a thin mica window. The intensity was far in excess of that required, but was made necessary due to its geometry. Actually, a narrow rectangular beam of 1 x 7 mm. was collimated from this source. In use, it was found that the mica window was extremely fragile and had a tendency to fracture. This left the source exposed and, although operative, made it hazardous because of its high toxicity.

In view of the above findings, the source structure and geometry were changed to that shown in Figure 3-1. The source holder is still aluminum, however, the geometry of the source as well as the holder is rectangular. As is seen in Figure 3-1, the source is 1 x 10 mm. , its strength is 15 mc. at formation, and covering the source now is a stainless steel window of 3 mg. per square centimeter.

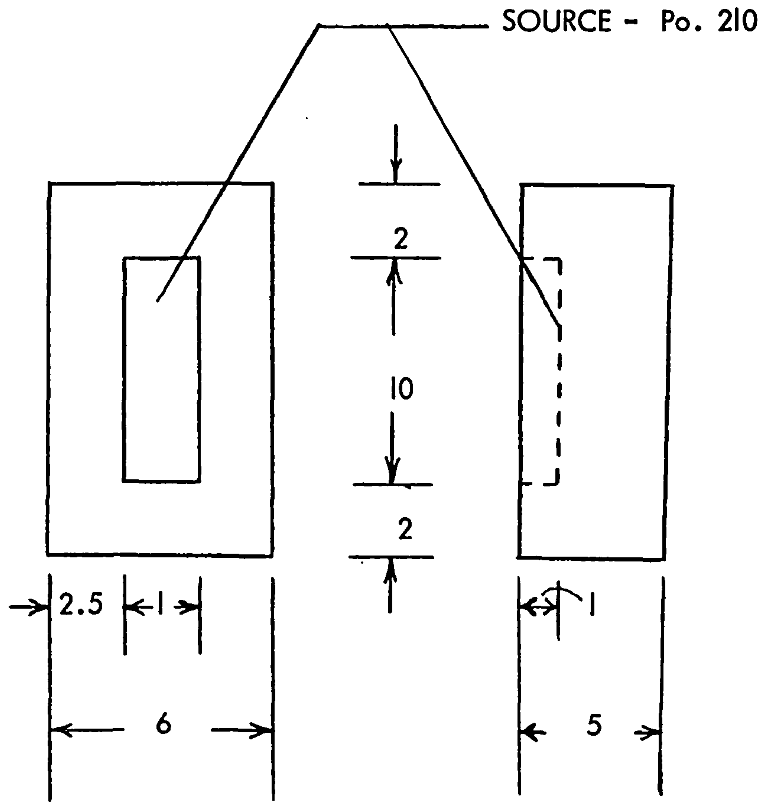

NOTE: ALL DIMENSIONS IN MILLIMETERS.

FIGURE 3-1 SKETCH OF SOURCE HOLDER

3.2.2 Beam Formation

An alpha particle beam formed from the source projects across the air stream. The beam traverses the entire test section, being narrower at the entrance and widening thereafter. Its average width in the test section is approximately 3 millimeters. The beam intensity along the test section axis is shown in Figure 3-2, and its derivation is given in Appendix I.

3.2.3 Ion Generation

Initially, the formation of ions will be treated as related to a single alpha particle injected into the air stream. There are approximately 15×10^4 ion pairs produced along the track of an alpha particle at ntp. These are not produced uniformly, but follow the Bragg curve. In the first two-thirds of its range, the rate of ion production is uniform, however, in the last third the rate begins to increase fairly quickly, reaching a maximum within a few millimeters of the end point. The alpha particle, in traversing this path, essentially loses energy only by ionization. The loss in energy is accompanied by a decrease in velocity. Hence, in the last few millimeters, the particle tends to veer away from its straight line path due to its lower velocity. Therefore, the useful portion of the path should not include the extreme end of the range, where straggling takes place. Excluding this extreme range, the average specific ionization is approximately 3×10^4 ion pairs per centimeter of path at ntp. The specific ionization varies directly with the density of the gas, whereas the range varies inversely. For example, if the density were half

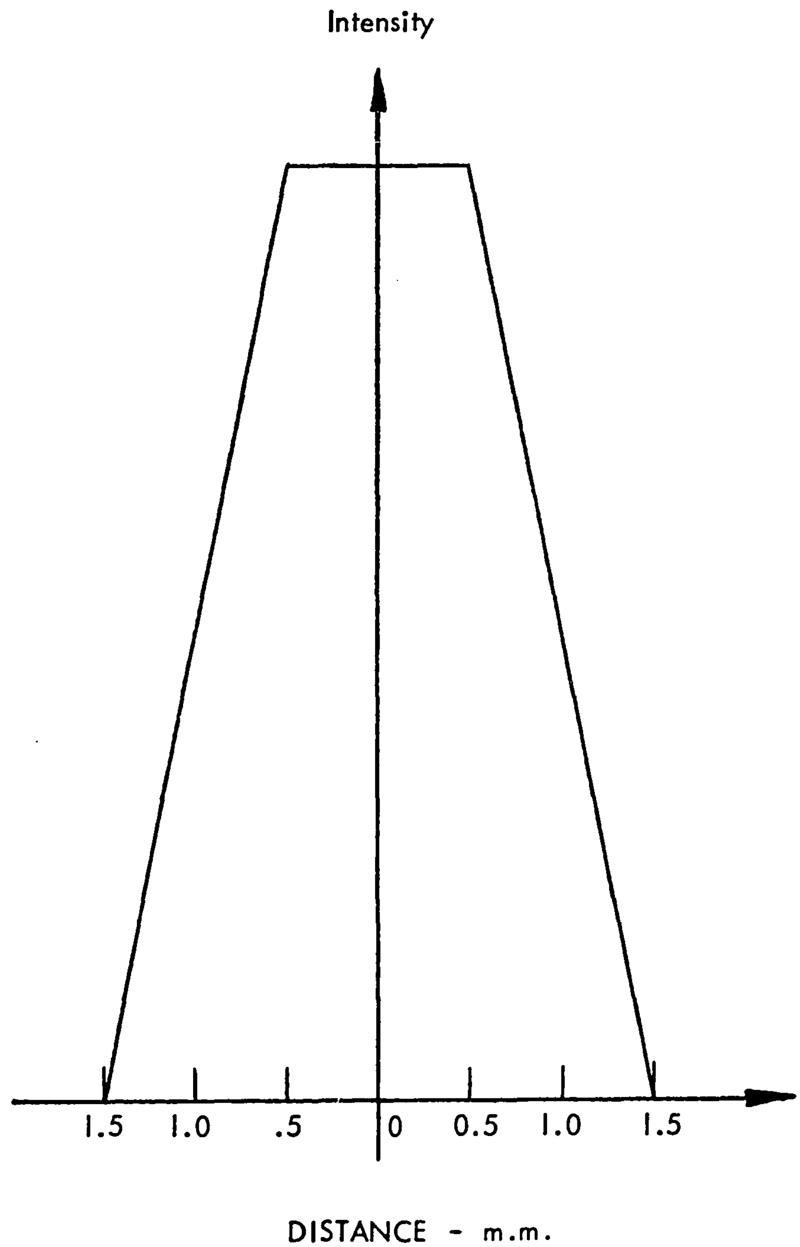

FIGURE 3-2 BEAM INTENSITY

that of ntp. the average specific ionization would be 1.5×10^4 ion pairs per cm. and the mean range would be 7.66 cm.

Assuming the useful portion, as specified above, of the Bragg curve is used, a detailed examination of a single α-particle track results in the following; the formation of a cylindrical column, containing equal numbers of electrons and ions centred on the α-particle track. The distribution of ions or electrons within this cylinder is not uniform, it is higher in the centre and declines exponentially with increasing radial distance. The distribution within the cylinder at formation, for either the electrons or ions is given by the function

$$n_{i,e}(r) = \frac{N_o}{\pi b^2} \exp - \left(\frac{r^2}{b^2}\right) \tag{3-2}$$

where $n_{i,e}(r)$ is the number of ions or electrons per unit volume, N_o the number of ions produced per unit length of the column, r is the distance from the column axis and b is a constant related to the average displacement R_o of the distribution from the column axis by

$$b = 2/\pi^{\frac{1}{2}} R_o \tag{3-3}$$

In Figure 3- 3a graph of this ion distribution is shown for both standard conditions as well as for test conditions.

That the ions are distributed as represented by (3-2) can best be understood in the following manner; the ionization is most intense adjacent to

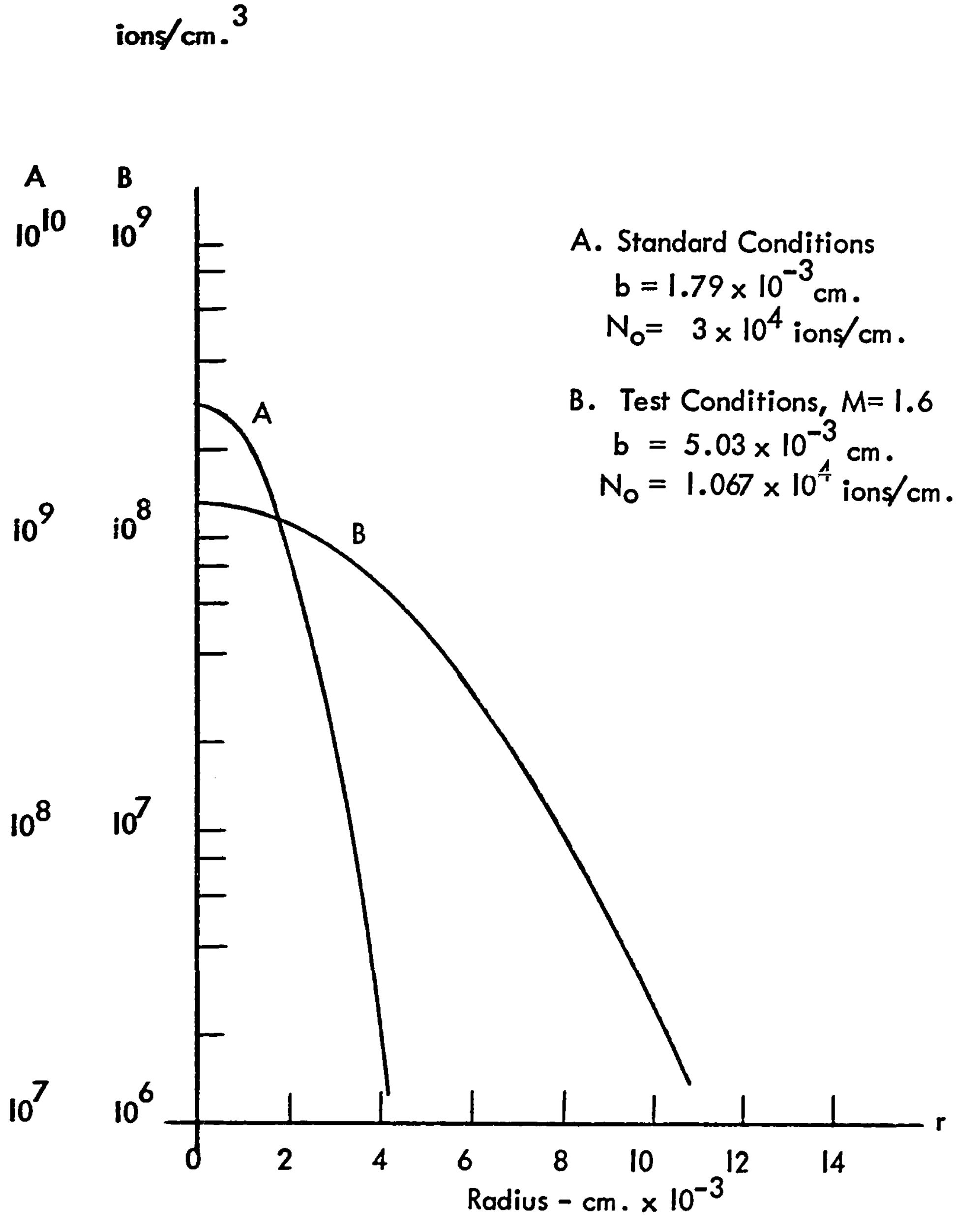

FIGURE 3 - 3 ION OR ELECTRON DISTRIBUTION ABOUT AN α - PARTICLE TRACK

the path of the nucleus of the α-particle as the ions are produced by a coulomb action on the outer electrons of the atoms. Thus, atoms further removed from the alpha's path are much less affected. These electrons are freed with some initial energy, thereby causing additional ionization and increasing the width. A very small number of these electrons have sufficient energy to form their own ionization track which jut out from the primary track at random. These effects are well illustrated in the photographs of Rutherford[21]. The constant b was evaluated by Jaffe[22] to give

$$b = 1.79 \times 10^{-3} \frac{P_o}{P} \text{ cm.} \tag{3-4}$$

where $\frac{P_o}{P}$ is the pressure ratio taken at normal temperature. However, the ion distribution depends upon density rather than pressure and since at normal temperature the density ρ is proportional to the pressure p so (3-4) can be written as

$$b = 1.79 \times 10^{-3} \frac{\rho_o}{\rho} \text{ cm.} \tag{3-5}$$

3.3 Diffusion, Recombination and Attachment

The ionic cylinder formed from the free air stream is bodily transported with it. Simultaneous with this directed motion the ions in the column undergo some change due to diffusion, recombination and attachment. These processes are somewhat involved and interacting. A suitable starting point would be the consideration of the electrons. The electrons in the column tend to diffuse outward according to the relation

$$\frac{\partial n_e}{\partial t} = D_e \nabla^2 n_e \tag{3-6}$$

where n_e is the electron density and D_e the diffusion coefficient for electrons. They also recombine with the positive ions to form neutrals according to

$$\frac{dn_e}{dt} = -\alpha_e n_i n_e \tag{3-7}$$

where α_e is the coefficient of recombination of electrons with positive ions and n_i is the density of positive ions. Electrons attach to O_2 molecules to form negative ions. The loss of electrons by attachment is given by

$$\frac{dn_e}{dt} = -\beta n_e \tag{3-8}$$

and β is the coefficient of attachment.

Combining these three effects and using a coordinate system centered on the column axis, the differential equation for electrons is then

$$\frac{\partial n_e}{\partial t} = D_e \nabla^2 n_e - (\alpha_e n_i + \beta)\, n_e \tag{3-9}$$

Since $\beta \gg \alpha_e n_i$ as shown in appendix 3 for the experimental values, then the electron distribution at any time t is determined from

$$\frac{\partial n_e}{\partial t} = D_e \nabla^2 n_e - \beta n_e \tag{3-10}$$

Using a cylindrical coordinate system due to the symmetry, equation (3-10) becomes

$$\frac{\partial n_e}{\partial t} = D_e \left(\frac{\partial^2 n_e}{\partial r^2} + \frac{1}{r} \frac{\partial n_e}{\partial r} \right) - \beta n_e \tag{3-11}$$

This equation is to be solved for n_e, with the necessary boundary and initial conditions. The method used to solve equation (3-11) follows that of Jaffe[23] and (12). A solution is assumed as the product of two functions

$$n_e\ (r,t) = N'(t)\ n'\ (r,t) \tag{3-12}$$

where $N'(t)$ is a function of time t only and $n'\ (r,t)$ is the exact solution of (3-11) for diffusion alone, i.e. $\beta = 0$. Hence (3-12) becomes

$$n_e(r,t) = \frac{N'(t)}{\pi(4D_e t + b^2)} \exp -\left(\frac{r^2}{4D_e t + b^2} \right) \tag{3-13}$$

Substituting (3-13) into (3-11), (3-11) is transformed into an ordinary differential equation for $N'(t)$ namely

$$\frac{dN'(t)}{dt} = -\beta N'(t) \tag{3-14}$$

which is readily solved to give

$$N^{I}(t) = g \exp - (\beta t) \tag{3-15}$$

As n_e for $t = 0$ is given by equation (3-2), the constant g is N_o.

The complete solution of (3-11) is

$$n_e(r, t) = \frac{N_o \exp - (\beta t)}{(4D_e t + b^2)\pi} \exp - \left(\frac{r^2}{4D_e t + b^2} \right) \tag{3-16}$$

If (3-16) is rearranged into the form

$$n_e(r, t) = \exp - (\beta t) \left(\frac{N_o}{\pi(4D_e t + b^2)} \exp - \left(\frac{r^2}{4D_e t + b^2} \right) \right) \tag{3-17}$$

Then the loss factor of electrons by attachment is $\exp - (\beta t)$, where β is the coefficient for attachment. Assume for the present that the term enclosed in brackets is constant, which is a 'worst' case condition as actually it is decaying, then at the end of $t = \frac{4}{\beta}$ sec. (equivalent to 12.85 μs) approximately 2% of the electrons remain, or at the end of $t = \frac{7}{\beta}$ (22.5 μs) less than 1% are left. For all practical purposes it can be stated that from $t \geq 30 \mu s$ no electrons exist and that they have been lost by attachment to form negative ions.

At this point it is advisable to have some indication, or estimate of the spatial dispersion of the ions. The reason is to determine the time when the individual expanding columns merge to form a larger distribution. The average column separation is readily obtained from the beam intensity and shutter speed. As the negative ions are created by attachment, then an estimate of the electron displacement in the absence of attachment gives an upper bound to the negative ion displacement, and the lower bound by assuming the electrons attach instantaneously. The root mean square displacement due to diffusion only is,

$$d\,(\mathrm{rms}) = \sqrt{4Dt} \tag{3-18}$$

Since the estimated distance between columns is .014 cm., $D_e = 477\ \mathrm{cm}^2/\mathrm{sec.}$ and $D_{\mathrm{neg.\ ion}} = .0995\ \mathrm{cm.}^2/\mathrm{sec.}$, then the columns overlap in less than 123 μs forming a larger distribution of positive and negative ions. This distribution is shown in Figure 2-7, and its derivation given in Appendix I.

The only items associated with the positive and negative ions to be considered are diffusion and recombination. Assuming that both the diffusion constant and density distribution for positive and negative ions are identical, then the following equation applies for either the positive or negative ions

$$\frac{\partial n}{\partial t} = D \nabla^2 n - \alpha n^2 \tag{3-19}$$

where n is the ion density, D the diffusion constant and α the recombination coefficient. Equation (3-19) is a nonlinear partial differential equation for which a solution is not readily available. However, the overall diffusion and recombination effects can be obtained by examining each individually. Thus, (3-19) for diffusion and recombination separately becomes

$$\frac{\partial n}{\partial t} = D \nabla^2 n \tag{3-20 a}$$

and
$$\frac{\partial n}{\partial t} = - \alpha n^2 \tag{3-20 b}$$

The solution of (3-20 a) for the one-dimensional case is

$$n(z, t) = \frac{N_o}{(\pi (4Dt + b^2))^{\frac{1}{2}}} \exp - (z^2/(4Dt + b^2)) \tag{3-21}$$

where $n(z, o)$ was assumed to be

$$n(z, o) = \frac{N_o}{(\pi b^2)^{\frac{1}{2}}} \exp - (z^2/b^2) \tag{3-22}$$

Substituting the experimental values ($D = .0995\ cm^2/sec.$, $t_{max.} = 6 \times 10^{-4}\ sec.$, $b_{min.} = .5\ cm.$) for D, t and b into Equation (3-21) results in b^2 being approximately $4 \times 10^3\ Dt$. Thus diffusion has negligible effect upon the ion distribution in the observation time.

Equation (3-20 b) has the solution

$$n(t) = \frac{n_o}{1 + \alpha n_o t} \tag{3-23}$$

where n_o, the initial ion distribution was assumed to be constant. This latter assumption is more stringent than the actual case. A conservative value for n_o, 10^7 ions/cm.^{3}, is obtained from (3-16) for $\beta = r = o$, $t = 30\ \mu s$ and replacing D_e with $D_{neg.ion}$. If this value for n_o together with $\alpha = 1.4 \times 10^{-6}$ ion per sec. (Von Engel[24]) and $t = 6 \times 10^{-4}$ sec. are substituted into (3-23), then the total change in ion density in the measurement time is only 0.84%. Therefore, recombination, like diffusion, can be neglected with little error.

Since diffusion and recombination are negligible, the ion distribution is identical for all practical purposes to that formed in the initial period. The entire distribution is electrically neutral on a macroscopic scale containing a mixture of equal numbers of both positive and negative ions. It can be concluded that the ion distribution is a suitable tracer element for velocity measurement as it is transported with almost perfect fidelity.

CHAPTER IV

THE DETECTION SCHEME

4.1 Introduction

In the last chapter an ion tracer was generated within the moving air stream by irradiating the flow intermittently with an α-particle source. This tracer was shown to be electrically neutral; it consisted of two equal but oppositely charged superimposed ion distributions. The present chapter is devoted to the task of explaining the mechanism whereby this neutral ionic cloud is detected.

Initially a brief review of the author's earlier detection theories will be presented in order to show the necessity for a more complete consistent theory. These will be referred to as the 'net charge' and 'dielectric' models. As will be shown, each in turn proved to be inadequate in explaining the anomalous experimental behavior. For example, in one instance not only was a predicted characteristic not observed but it resulted in the complete loss of signal. It is for this reason that these models are included and, to indicate the various stages of reassessment necessary, with the accumulation of "misinformation bits"*, to bring theory into line with practice. Hopefully, in a broader sense it may help to explain the confusion that often arises through simple errors in physical interpretation.

The section pertaining to the analysis of the present scheme divides conveniently into two independent parts. The first part relates to forming a net

* "misinformation bit" - coined to describe information available that was missed, misinterpreted, misunderstood, or inadequately explained at the time.

charge density by the action of an electric field on the neutral ionic distribution in a region adjacent to the detector probe. In the second section induced current theory is applied to the developed space charge to compute the voltage between the shield and the detector probe. By comparing the latter predicted characteristic with experimental results, the agreement is particularly favourable.

A few preliminary remarks regarding the type of presentation is in order. The theory develops from the grossest assumptions and finishes on one devoid of mathematical and physical vigor. In particular, it treats a case which is much simplified and abstracted from the real physical situation. It was made simple in order that the mathematics associated with the problem be simple and tractable. Otherwise it would pose a most formidable and difficult task and, in all probability, could be considered as a thesis topic in its own right. It is the author's opinion that these simplifications are sufficient to understand the main characteristics which are important in the detectors use. The final justification lies with experimental verification.

4.2 Review of Detection Theories

4.2.1 Net Charge Model

At the outset of the present investigation, based on the assumptions of that time, computation indicated that a net positive charge density existed in the ion cloud. It was shown that such a charge moving past the detector probe would induce a potential on it. Several different standard AC coupled amplifiers having high input impedance (up to 400 meg. II 2pf)* connected to the detector probe were found to be inadequate to measure this voltage. A cathode follower operating with an open grid, and an 'infinite' input impedance amplifier (see Chapter 5) specially designed for this purpose proved to be sufficient to measure the signal. A typical signal detected by these amplifiers is shown in Figure 4-1. The signal levels, somewhat below that expected, were in the range of 1 to 10 millivolts. Also, it should be noted how the signal is broad-based and lacking in a well defined peak. At this juncture the first "bit of misinformation" entered the picture : An attempt to sharpen the detected pulse by using a driven shield (electrostatic) around the detector probe failed. It failed completely, primarily by reducing the signal level such that it was almost, if not totally, obscured by the noise and secondly, it did not reduce the width. Another and perhaps more significant "misinformation bit" was the signal inversion from that predicted.

The problem of reduced signal levels, from that expected, was readily resolved by examining the original assumptions and making the necessary corrections. That is, it had been assumed that ionization produced electrons and ions from which couple the electrons were deflected out by the earth's field leaving only the heavier ions. The correction involved the realization that vacuum conditions do not prevail and that the attachment mechanism had to be included. However,

---

* II signifies "in parallel with".

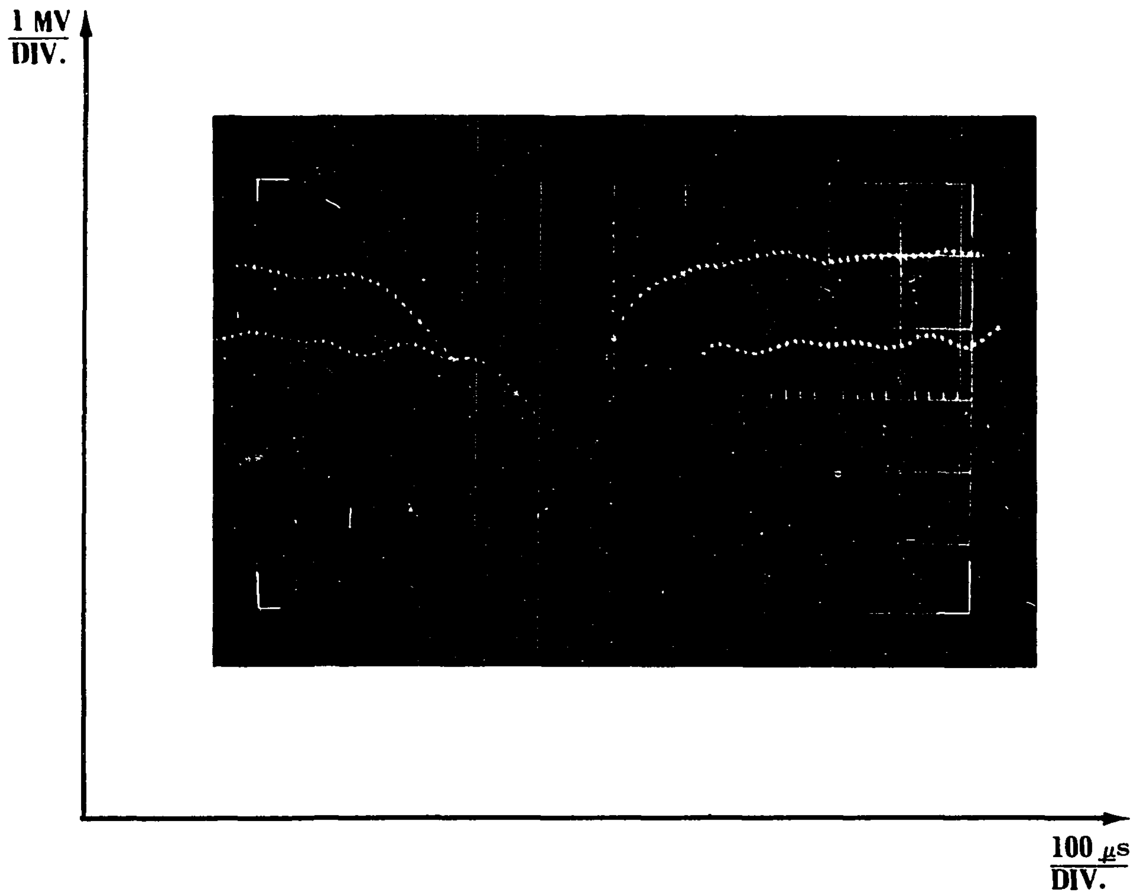

FIGURE 4-1. TYPICAL OUTPUT OF TWO ADJACENT DETECTORS.

this still left a small net positive charge and did not help to resolve the additional "misinformation bits".

The entire ion generation theory was then examined in more detail leading to the results and conclusions of the last chapter. This, together with the unexplained results, proved conclusively the inadequacy of the so-called ' net charge model '.

4.2.2 Dielectric Model

In the search for a suitable detector theory, a "dielectric model" to represent the electrically neutral ion tracer appeared to be more promising. The rationale behind this model is as follows : Firstly, the AC coupled amplifiers did not detect a signal, whereas, both the cathode follower and 'infinite' input impedance amplifiers which are DC coupled did. Secondly, it was found that both these amplifiers had a DC potential at their input terminals, thus applying a voltage to the probe with respect to ground. Hence, the detector probe together with the surrounding shield constitute a capacitive transducer deriving its polarizing voltage from the amplifiers. The dielectric of the transducer is the streaming air which has as a modulating signal the ion cloud. The experimental data already obtained was in good agreement with this model's predictions.

Using this model and a carefully adjusted experimental setup to take full advantage of its characteristics - the last "bit of misinformation" fell by way of signal inversion. That is, a negative signal was predicted for a positive polarizing voltage and vice versa, the result was opposite. In other respects, such as amplitude and waveform, it was in good agreement. The main adjustment involved neutralizing the transducer's capacity by the 'infinite' input impedance amplifier leaving a net impedance of approximately 0.3 pf II megohms. Having learned the lesson from the net charge model, it was concluded that the dielectric model was invalid.

4.3 Present Theory

The detection mechanism can be explained in the following simple manner. The neutral ion cloud moves towards the detector region with a velocity U_o . After entering the detector region the ions are acted upon by an electric field and they perform a non-collective drift in this field. As a result the negative and positive ion distributions move in opposite directions in this interaction region and their densities deviate from one another at any point in this region. A direct consequence of this result is the formation of a space charge density in the region adjacent to the probe. This charge density grows with deeper penetration of the cloud in the detector and then decays as the cloud exits. The space charge may then be considered as a source for voltage on the detector.

4.3.1 Field Considerations

The magnitude for the applied electric field can be estimated from the Debye Length, (25), (26), (27). Here, the random thermal forces acting on the positive and negative ions in the gas are balanced by electrostatic ones for distances and beyond the Debye Length,

$$D = \left(4\pi \sum_{s} \frac{n_s e_s}{kT} \right)^{-\frac{1}{2}} \tag{4-1}$$

For this case the positive and negative ion densities are equal at every point on a macroscopic scale.

When the ionized gas is subjected to a strong externally derived electric field this ideal behavior is destroyed. The charged particles drift in this field, i.e., positive ions with the field and negative ions against the field. This results in the production of a space charge region due to positive and negative ion densities deviating from one another at any field point.

In order to derive the space charge density the behavior of the ions in an external electric field is analyzed. The treatment is for a simple geometrical case abstracted from the actual detection system. It assumes the ions have been created prior to entering the interaction region which is bounded by the electrode system. It is necessary that the external field be larger than the space charge field (28), expressed as,

$$|E_{ex}| > |E_{sc}| , \tag{4-2}$$

where,

$$0\left\{\,|E_{sc}|\,\right\} = \text{max. } [\,4\pi e\, L\, n\,] \tag{4-3}$$

L is the electrode spacing, and n is the ion density.

4.3.2 Space Charge Generation

The problem first considered is to find the distrubance produced in the neutral ion cloud by the field of the detector probe. A cylindrical gaseous beam, having the spatially periodic ion density (positive and negative ions) illustrated in Figure 4-2, flows through the detector region. The detector is assumed to extend infinitely in the Z-direction and is partitioned into sections, one such section is shown in Figure 4-3. It has three thin circular metal plates with small holes at their centers. A, P and B, separated from each other by a distance L. Through the hole in A the beam enters the detector region. It then continues axially through the probe P to exit via B. B now acts as the entrance to the succeeding section.

In the calculations it is assumed that across the beam all the particles have the same velocity, i.e., the beam has a uniform cross-section. In addition it is assumed that the potentials on the electrode system A, P and B cause a field to exist throughout the region directed parallel to the axis of the system and uniform over the entire cross-section. The field being

$$E(z) = -E_o \sin \frac{\pi z}{L} \; . \tag{4-4}$$

These assumptions reduce the analysis to be one-dimensional.

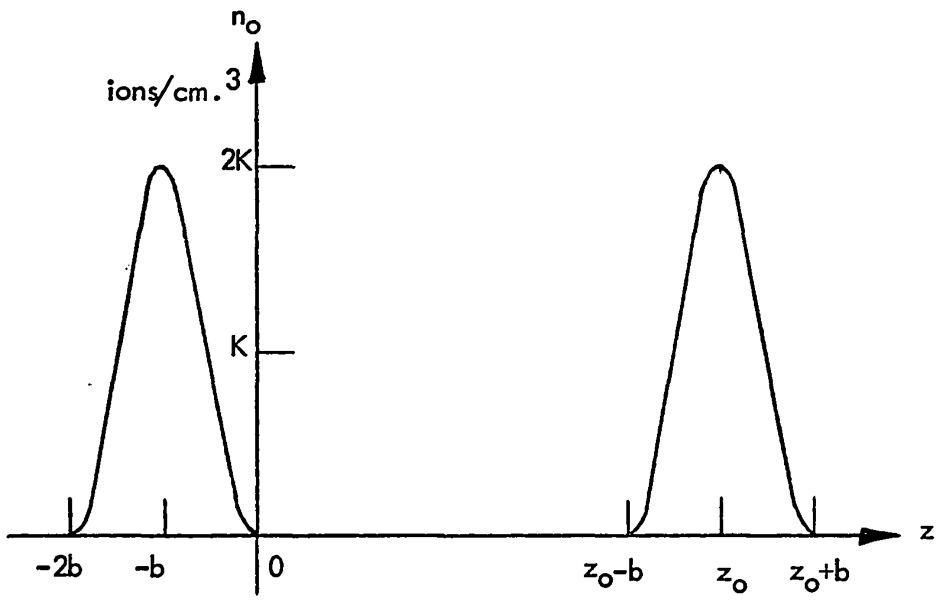

FIGURE 4 - 2 SPATIAL ION DENSITY

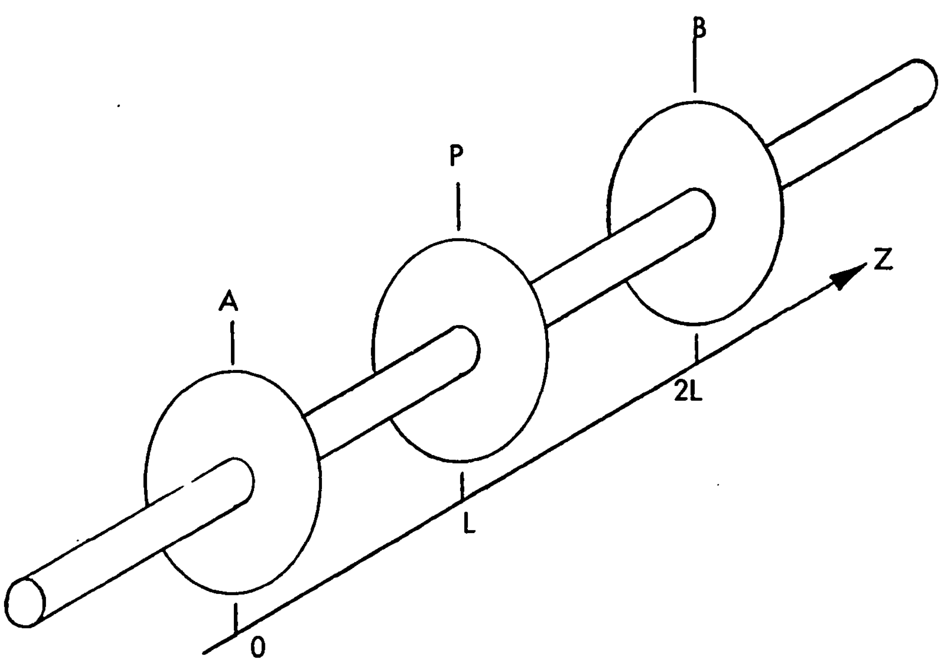

FIGURE 4 - 3 ONE SECTION OF DETECTOR

The neutral ion density distribution (Figure 4-2) consists of two equal but oppositely charged superimposed distributions. Let either of these be represented by

$$n_o(z, o) = K \left[1 + \cos \pi \frac{(z+b)}{b} \right] \qquad -2b < z < 0 \qquad (4\text{-}5)$$

at time, $t = o$, when the leading edge is just about to enter the interaction region ($Z = 0$ at A) in Figure 4-3. At some later time, t', in the absence of an electric field, the amplitude at the entrance plane is

$$n_o(o, t') = 2K \sin^2 \pi \frac{U_o t'}{2b} \qquad (4\text{-}6)$$

When exposed to the electric field the ions have a drift velocity determined by their mobility, the magnitude and direction of the field. For the positive ions the drift velocity is given as

$$\overset{+}{U}_d = -\mu_+ E_o \sin \frac{\pi z_+}{L} , \qquad (4\text{-}7)$$

this results in a total velocity of

$$\overset{+}{U} = \frac{dz_+}{dt} = U_o \left[1 - \delta \sin \frac{\pi z_+}{L} \right] \qquad (4\text{-}8)$$

where $\delta = \frac{\mu_+ E_o}{U_o}$. The solution of (4-8) for $\delta << 1$ is

$$z_+ = U_o t - 2 \frac{L\delta}{\pi} \sin^2 \frac{\pi z_+}{2L} \qquad (4\text{-}9)$$

Since the particles must be conserved, it is necessary that

$$\overset{+}{n}(z_+, t)\, dz_+ = n_o(o, t')\, d\, z_o \tag{4-10}$$

Utilizing (4-6), (4-8), (4-9), and (4-10) results in the new positive ion amplitude

$$\overset{+}{n}(z_+, t) = 2K \left[\sin^2 \frac{\pi (U_o t')}{2b} \right] \left[1 + \delta \sin \frac{\pi z_+}{L} \right] \tag{4-11}$$

A similar development for the negative ions leads to

$$z_- = U_o t + \frac{2 L \delta}{\pi} \sin^2 \frac{\pi z_-}{2 L} \tag{4-12}$$

$$\bar{n}(z_-, t) = 2K \left[\sin^2 \frac{\pi(U_o t')}{2b} \right] \left[1 - \delta \sin \frac{\pi z_-}{L} \right] \tag{4-13}$$

The net charge density, $\rho(z, t)$ is then determined from

$$\rho(z, t) = e \left[\overset{+}{n}(z, t) - \bar{n}(z, t) \right] \tag{4-14}$$

To evaluate (4-14) requires the utilization of (4-11) and (4-13) but, the field points, Z's, must be identical. Examing (4-9) and (4-12) it becomes apparent that $z_- > z_+$. Let t in (4-12) be retarded to $t - \tau$ such that $z_- = z_+$ i.e.,

$$\tau = \frac{4 L \delta}{\pi U_o} \sin^2 \frac{\pi z}{2 L} \tag{4-15}$$

Applying a Taylor's series expansion to $\bar{n}(z, t)$ about $t' + \tau$ and neglecting terms $o\left\{ \delta^2 \right\}$ and higher, leaves

$$\bar{n}(z, t) = 2K \left[1 - \delta \sin \frac{\pi z}{L} \right] \left[\sin^2 \frac{\pi (U_o t')}{2b} + \frac{2L\delta}{b} \sin^2 \frac{\pi z}{2L} \sin \frac{\pi (U_o t')}{b} \right] \tag{4-16}$$

Now evaluating (4-14) by way of (4-11) and (4-16) yields

$$\rho(z, t) = 4 \delta Ke \left(\sin \frac{\pi z}{L} \sin^2 \frac{\pi(U_o t')}{2b} - \frac{L}{b} \sin^2 \frac{\pi z}{2L} \sin \frac{\pi(U_o t')}{b} \right) \tag{4-17}$$

A particular case of interest, $L = b$, which approximates the experimental situation gives the space charge density as (note $U_o t' = U_o t - z$)

$$\rho(z, t) = 4 \delta Ke \left[\sin \frac{\pi(U_o t - 2z)}{2L} \right] \left[\cos \frac{\pi (U_o t - 2z)}{2L} - \frac{\cos \pi U_o t}{2L} \right] \tag{4-18}$$

Equation (4-18) is graphically displayed in Figure 4-4. It should be noted that the space charge has odd symmetry about $z = U_o t/2$ and length $U_o t$. These aspects are of some importance in succeeding section dealing with the voltage and current of the detector circuit. From equation (4-18), it is found that $\rho(z, t)$ has a maximum amplitude at $t = 2L/U_o$, i.e., when the ion cloud fills the entire detector region. Further, at this time all the positive charge is located in the region $0 < z < L$ and all the negative charge in the region $L < z < 2L$.

4.3.3 Calculation of Voltage

As the space charge distribution is known, theory permits an exact calculation of its effect on the probe circuit. Therefore, any errors in the following results

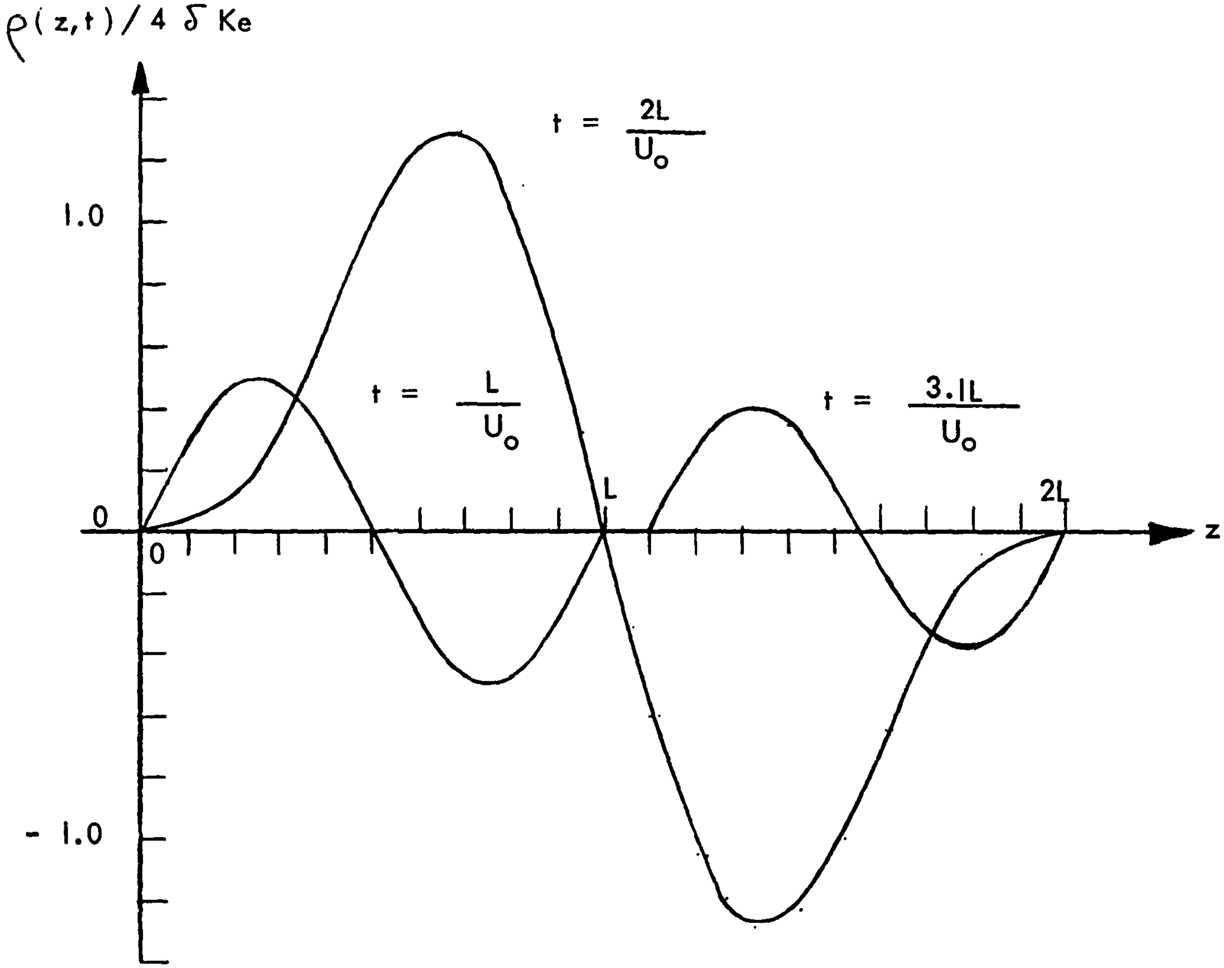

FIGURE 4-4 SPACE CHARGE DENSITY IN THE DETECTOR REGION

should arise from the detector system model. The approximate method which is offered permits reasonable quantitative estimates of the voltage in the detector circuit. The key concepts used here are borrowed from the description of microwave tube behaviour, (29), (30), (31).

4.3.3.1 Voltage Computation

With reference to Figure 4-3, consider that A and B are connected to ground and that A or B then act as one plate of a parallel plate capacitor with P being the other one. The voltage across this capacitor is given by

$$V(t) = -\int_0^L E(z, t)\, dz \tag{4-19}$$

where $E(z, t)$, the space charge field, is determined from the divergence relation

$$\frac{\partial}{\partial z} E(z, t) = \frac{\rho(z, t)}{\epsilon_o} \tag{4-20}$$

Substituting (4-18) and (4-20) into (4-19) one obtains

$$V(t) = -\frac{\delta K e L^2}{\pi \epsilon_o}\left[\frac{1}{\pi}\sin\pi\left(\frac{U_o t}{L}\right)+\left(\frac{U_o t - L}{L}\right)\left(1 + 2\cos^2\pi\left(\frac{U_o t}{2L}\right)\right)\right]$$

$$L < U_o t < 2L \tag{4-21}$$

Equation (4-21) is plotted in the graph of Figure 4-5. Here only half of the voltage waveform is shown due to the symmetry. The waveform is negative, falling slowly, becoming almost linear, and finally peaking.

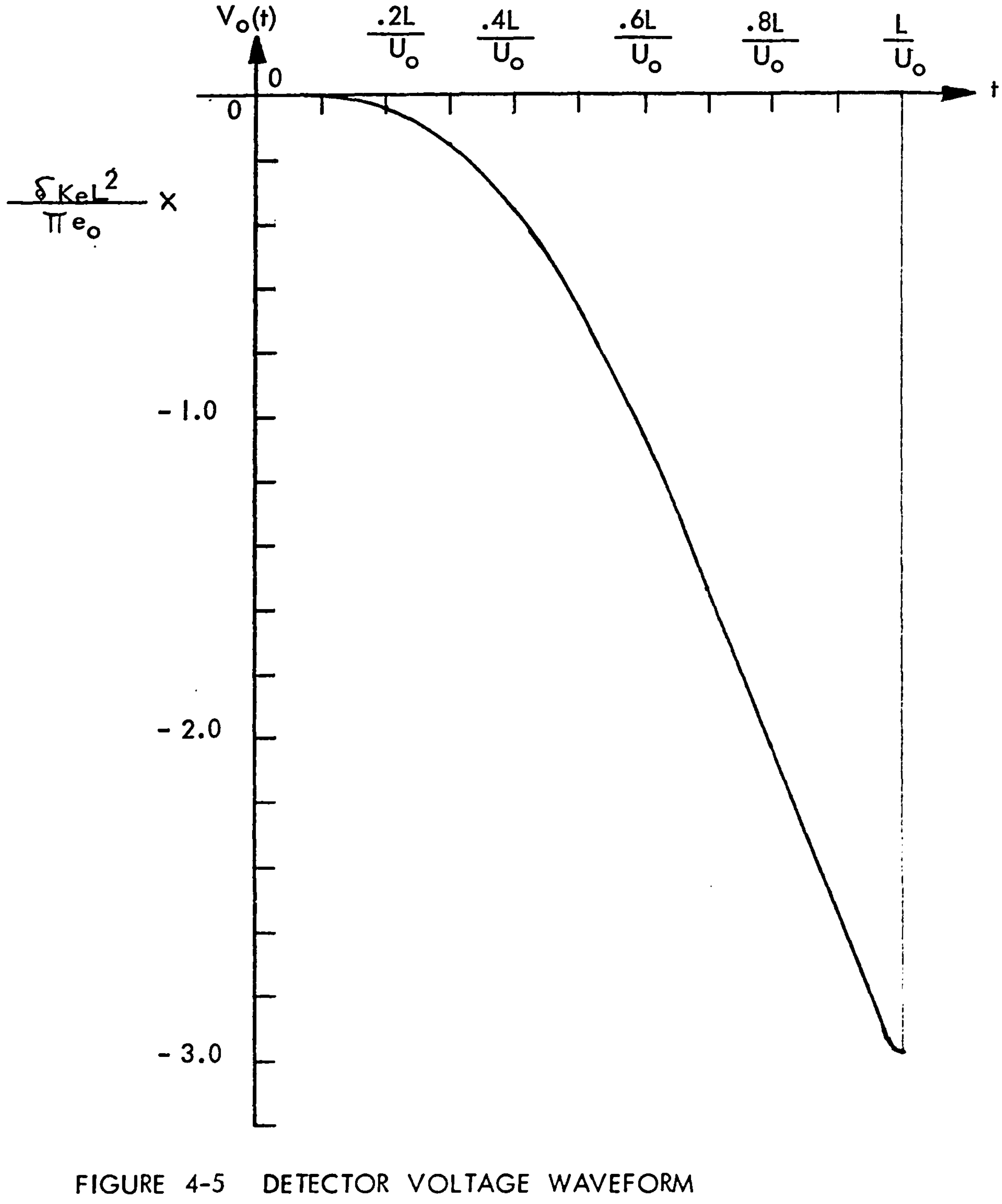

FIGURE 4-5 DETECTOR VOLTAGE WAVEFORM

4.4. Discussion

The results of the simple analysis of the detector mechanism are particularly encouraging. However, the calculations deal with a very simple approximation to the real system; it considers the case of a uniform beam, a uniform electric field and a simple electrode system. In order to pursue this problem more completely, each of these restrictions should be relaxed.

Much useful information has been gleaned from these calculations aside from the favorable verification of experimental results. To begin with, there is the total dependance of the output signal upon the detector amplifier input impedance. Of equal importance, as a measurement technique, the calculations show that the peak of the detected signal is in synchronism with the peak of the ion distribution. In addition, the calculations give estimates of both the signal amplitude and width.

In considering the assumption of a uniform beam much can be said. For example, there is the possible spread in thermal velocities with which to contend. Similarly, the assumption of uniformity across the beam is open to serious question. However, no justification will be given for these assumptions.

The problem of the uniform field does warrant further discussion. For the electrode system postulated, it is easy to visualize that the field would be uniform between the plates and if the holes were sufficiently small, it would also be uniform over the cross section. The field would be given by

$$\begin{aligned} E(z) &= -E_o \qquad 0 < z < L \\ &= +E_o \qquad L < z < 2L \end{aligned} \tag{4-22}$$

Since the field is periodic in z, with period 2 L it can be represented by a Fourier series,

$$E(z) = -\frac{4}{\pi} E_o \sum_{n \text{ odd}} \frac{1}{n} \sin \frac{n \pi z}{L} \qquad (4\text{-}23)$$

The analysis was carried out for the fundamental only, as the harmonics vary as $1/n^3$ in V (t) add little eg. the first would be 1/27 of the fundamental.

More important than the harmonics is the postulated electrode system. The real electrode system, see Figure 4-7, has axial symmetry and gives rise to a two-dimensional field. To determine this field requires the solution of Bessel's equation with mixed boundary (32) conditions. In order to effect a solution, some simplifying assumptions would be made and in the limit would involve a numerical technique (33), (34). The z variation of this two-dimensional field would be exponential and hence could be approximated by a saw tooth waveform. The Fourier series for this saw tooth is

$$E(z) = \frac{2E_o}{\pi} \sum_{n=1} (-1)^n \frac{1}{n} \sin \frac{n \pi z}{L} \qquad (4\text{-}24)$$

Hence, in the main the analysis would be identical to that carried out. Since the express purpose of the development presented was to describe the gross behaviour, the assumptions are justified.

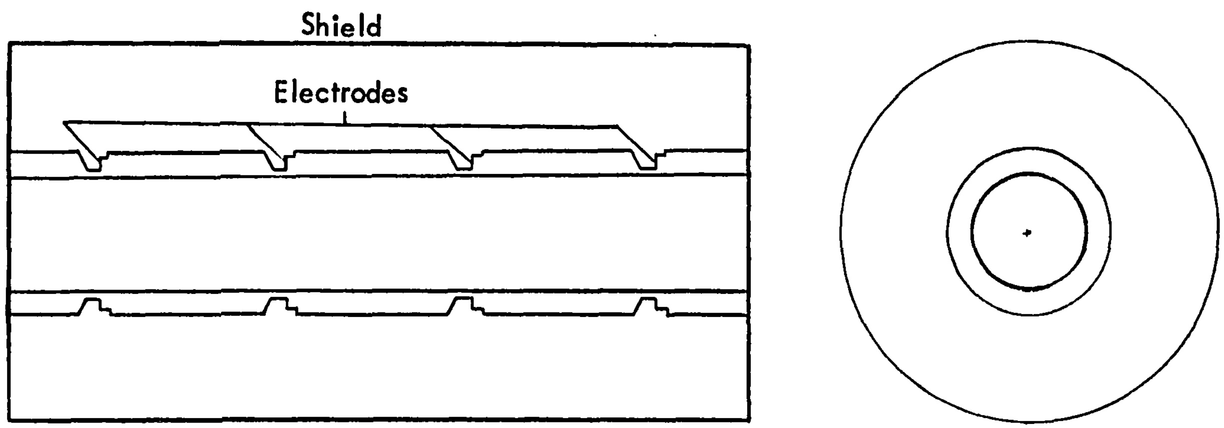

FIGURE 4-7 THE REAL DETECTOR SYSTEM

CHAPTER V

ELECTRONIC CIRCUITRY

5.1 Introduction

Chapter four dealt with the transducer for translating the presence of ions into an electrical signal. Now that an electrical input signal is available, the remaining system can be examined in detail. This entails the problems associated with signal measurement, signal conditioning and signal recording. It is these topics that will be discussed in the present chapter.

A block diagram of the electronic system is shown in Figure 5-1. The system operates as follows: The input signal S(t), from the detector, is a sequence of round topped pulses whose peak time must be accurately determined. To do this, the signal is first measured and amplified. The amplified signal is then differentiated - which transforms the peak time to the zero crossing time. The zero crossing detector generates a narrow standardized pulse at the zero crossing which is applied to an R-S Flip-Flop. For example, signal $S_1(t)$, from detector 1, would set the Flip-Flop and $S_2(t)$, from detector 2, would then reset the Flip-Flop. The output from this Flip-Flop is a train of equal amplitude rectangular pulses whose width is the ion transit time between detectors l and 2. These pulses are now filtered by a low-pass filter and the result recorded. A continuous recording of the ion transit time is thus obtained from which the velocity can be determined.

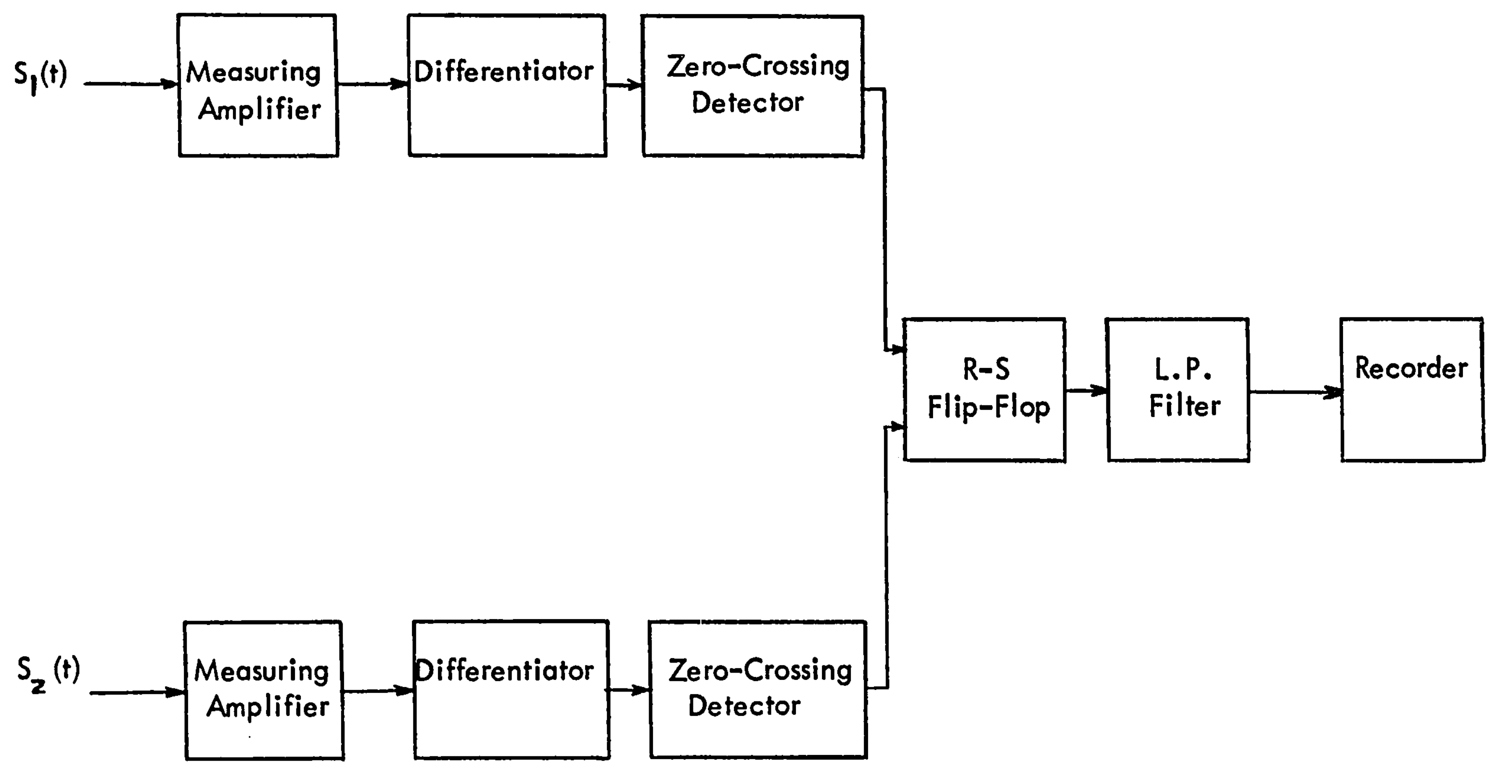

FIGURE 5-1 - ELECTRONIC SYSTEM BLOCK DIAGRAM.

5.2 Signal Measurement

Chapter four indicated that the detector can be represented electrically by a high impedance voltage source. The signal from the source can have a high rate of rise. Hence, it is imperative to have an amplifier with an effective impedance in excess of the transducer's and a risetime less than that of the transducer.

5.2.1 General Considerations

In order to ensure the faithful reproduction of the signal at the amplifier output, it is necessary that -

1. The amplifier be linear.
2. The amplifier input impedance be much greater than the transducer's.
3. The amplifier bandwidth be in excess of the signal's.
4. The amplifier risetime be considerable less than the signal's.
5. The amplifier input noise, forever present, be less than the signal amplitude.

Amplifier circuits are available (35), (36), which can meet two or more conditions but not all five. One such amplifier is the simple cathode follower shown in Figure 5-2. It was utilized initially but had to be replaced because of microphonics activated by vibrations during wind tunnel operation. A replacement circuit was developed to meet all five conditions.

The development originated with a high input impedance amplifier to which positive feedback was applied. The effect of the positive

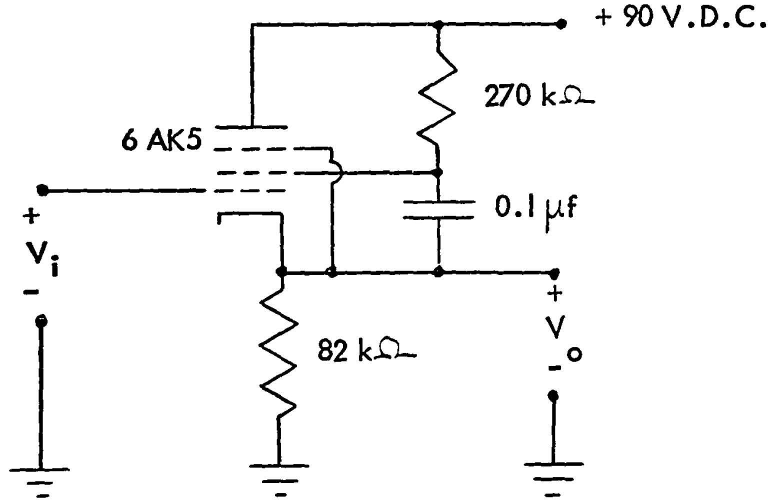

FIGURE 5-2 CATHODE FOLLOWER

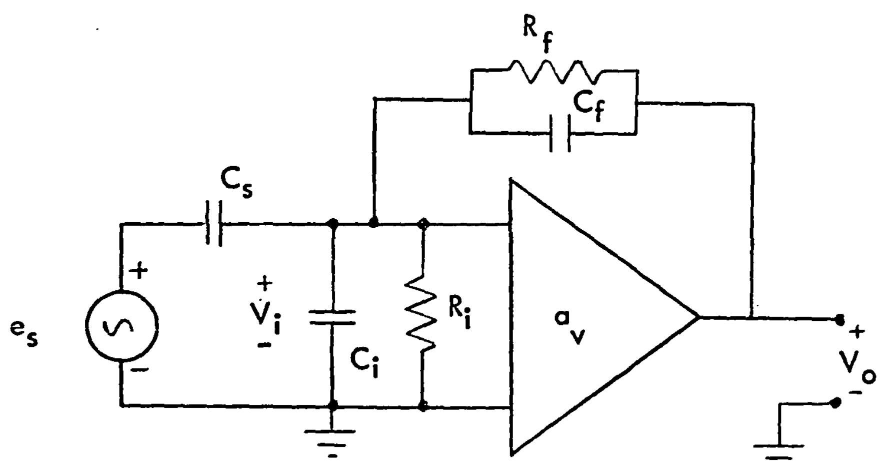

FIGURE 5-3 POSITIVE FEEDBACK CIRCUIT

feedback is to neutralize the input impedance of the amplifier. If sufficient feedback is applied, then not only is the amplifier's input impedance neutralized but also, any additional impedance attached to the input, such as the transducer's. This latter aspect results in what may be called a bonus. Furthermore, the DC polarization for the detector can be easily included in the design.

5.2.2 Neutralization - Negative Admittance Generation

The theory for neutralization and negative input admittance generation are identical. The general circuit applicable in the present case is shown in Figure 5-3. With reference to Figure 5- 3, a_v is the voltage gain of the ideal amplifier which has infinite input impedance, zero output impedance, infinite bandwidth and zero phase shift. R_i and C_i represent the total resistance and capacitance from the input terminal to ground, which includes the actual input impedance of the amplifier. R_f and C_f together make up the feedback network between the output and the input. The transducer is modelled here by e_s in series with c_s.

Summing the currents at the amplifier input node,

$$(e_s - V_i)SC_s + (V_o - V_i)(G_f + SC_f) - V_i(G_i + SC_i) = 0 \tag{5-1}$$

$$V_o/V_i = a_v \tag{5-2}$$

where s is the complex Laplace transformer variable.

Using (5-1) and (5-2) for the closed loop gain A_v,

$$A_v = \frac{V_o}{e_s} = \frac{a_v C_s}{C_s + C_i - C_f(a_v - 1)} \bullet \frac{S}{S + \dfrac{G_i - G_f(a_v - 1)}{C_s + C_i - C_f(a_v - 1)}} \tag{5-3}$$

and for the input admittance Y_{in},

$$Y_{in} = G_i - G_f (a_v - 1) + S (C_i - C_f (a_v - 1)) \qquad (5\text{-}4)$$

There are three cases of particular interest:

Case a

If, $$G_f (a_v - 1) = G_i \qquad (5\text{-}5)$$

and, $$C_f (a_v - 1) = C_i \qquad (5\text{-}6)$$

then $$Y_{in} = 0 . \qquad (5\text{-}7)$$

That is, the amplifier circuit presents an infinite impedance to the source and the output voltage V_o is

$$V_o = a_v e_s \qquad (5\text{-}8)$$

This case is suitable for measuring the voltage V(t) derived in chapter four as is the next case.

Case b

If equation (5-5) is valid and

$$C_f (a_v - 1) > C_i \qquad (5\text{-}9)$$

then $$Y_{in} = - S (C_f (a_v - 1) - C_i) = - SC \qquad (5\text{-}10)$$

Here the amplifier supplies a negative susceptance to the source which tends to reduce the source susceptance, SC_s. The overall voltage gain becomes,

$$A_v = \frac{a_v C_s}{C_s - C} \qquad (5\text{-}11)$$

This situation results in signal enhancement at the input to the amplifier. There are practical limits for this case associated with the amplifier system stability.

Case c

Here we select $G_f (a_v - 1) < G_i$ (5-12)

and $C_f (a_v - 1) = C_i + C_s$ (5-13)

which results in $Y_{in} = G_i - G_f (a_v - 1) - SC_s$ (5-14)

The negative input susceptance then completely neutralizes the source susceptance leaving a net input impedance somewhat smaller than G_i . This case is not ideal as it loads the source e_s with the conductance of (5-14). Similar to case b, there are stability limits on the reduction of G_i in addition to noise limits, that is, noise increases with a reduction in G_i .

In the above analysis it was assumed that a_v is frequency independent. Since practical amplifiers have a finite bandwidth, its effect must be taken into account . This is best done by considering the actual amplifier.

5.2.3 The Amplifier

Since high input and low output impedance are desired, then the amplifier should be a series-shunt feedback amplifier (37). Conceptually, this would be as illustrated in Figure 5-4. The gain of such an amplifier (41) is

$$A_v = \frac{V_o}{V_i} = \frac{a_v}{1 + a_v f_b} \tag{5-15}$$

where, a_v is the open loop voltage gain and f_b is the feedback factor.

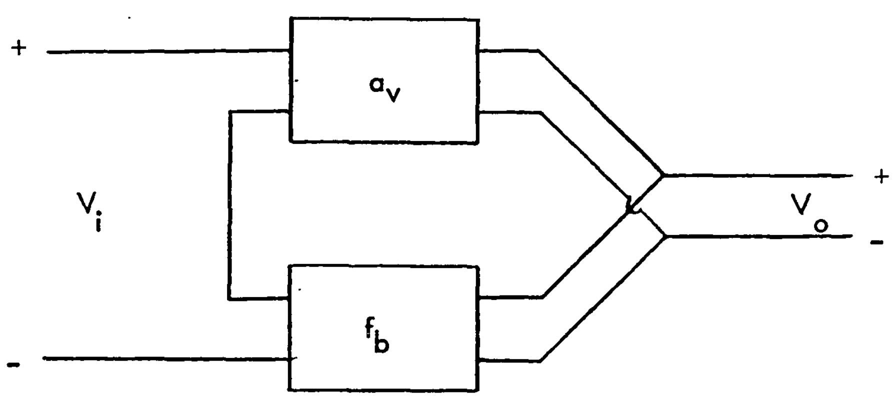

FIGURE 5-4. SERIES - SHUNT FEEDBACK AMPLIFIER.

Neglecting the bias network, such an amplifier circuit is shown in Figure 5 - 5. Practically, this is the simplest as it has the two stages required for a positive voltage gain in excess of unity. The FET input stage is used in order to realize high input impedance without feedback and to prevent loading of the feedback network made up of R_1 and R_2.

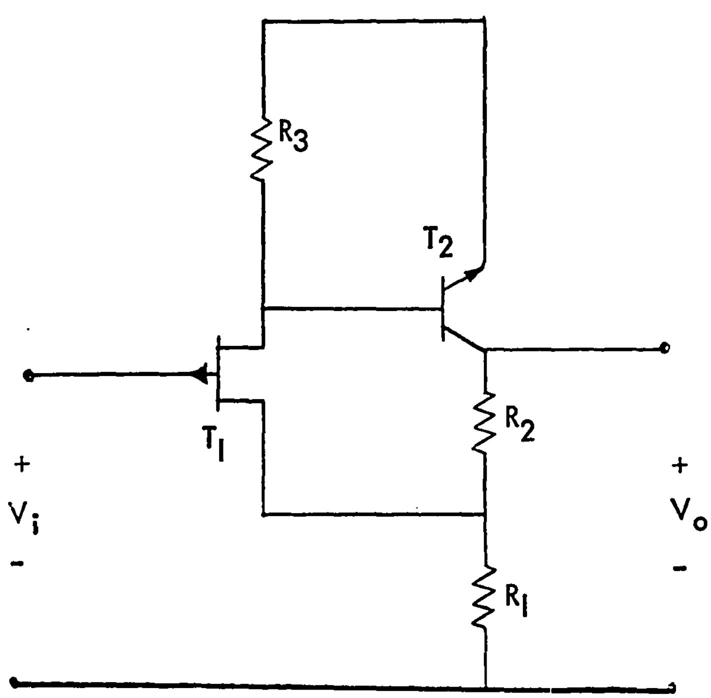

FIGURE 5-5 SIMPLE POSITIVE GAIN AMPLIFIER

For the purpose of analysis both the FET (T_1) and bipolar transistor (T_2) may be represented by the incremental model of Figure 5 - 6. Substitution of this model into the 'OPEN LOOP' amplifier determined from Figure 5-5 results in the circuit of Figure 5-7(a). In Figure 5-7(b) is the feedback network for the amplifier and its parameters.

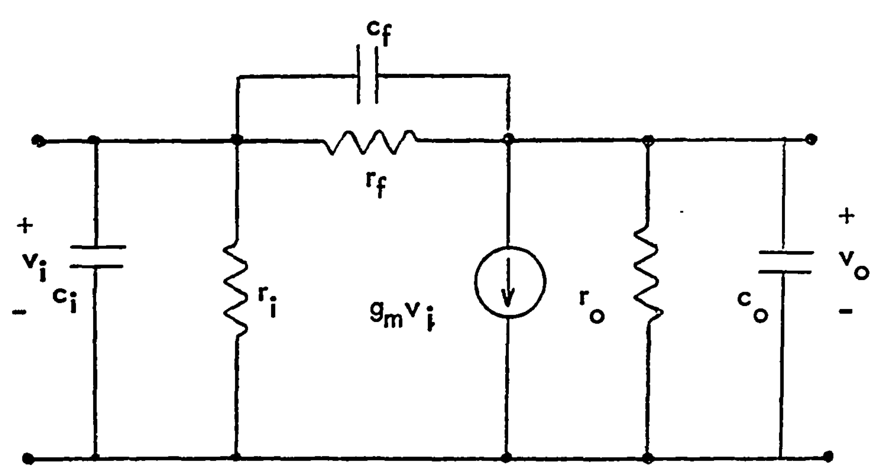

r_{i1} =	700 MΩ	c_{i1} =	18 pf
r_{i2} =	5.1 kΩ	c_{i2} =	350pf
r_{f1} =	700 MΩ	c_{f1} =	7 pf
r_{f2} =	14 MΩ	c_{f2} =	8 pf
r_{o1} =	125 kΩ	c_{o1} =	4 pf
r_{o2} =	32.7 kΩ	c_{o2} =	2 pf
g_{m1} =	0.5 m℧	g_{m2} =	66.5 m℧

M = 10^6, k = 10^3, m = 10^{-3}, p = 10^{-12},

Ω = ohms, ℧ = mhos, f = farads

FIGURE 5-6 TRANSISTOR MODEL

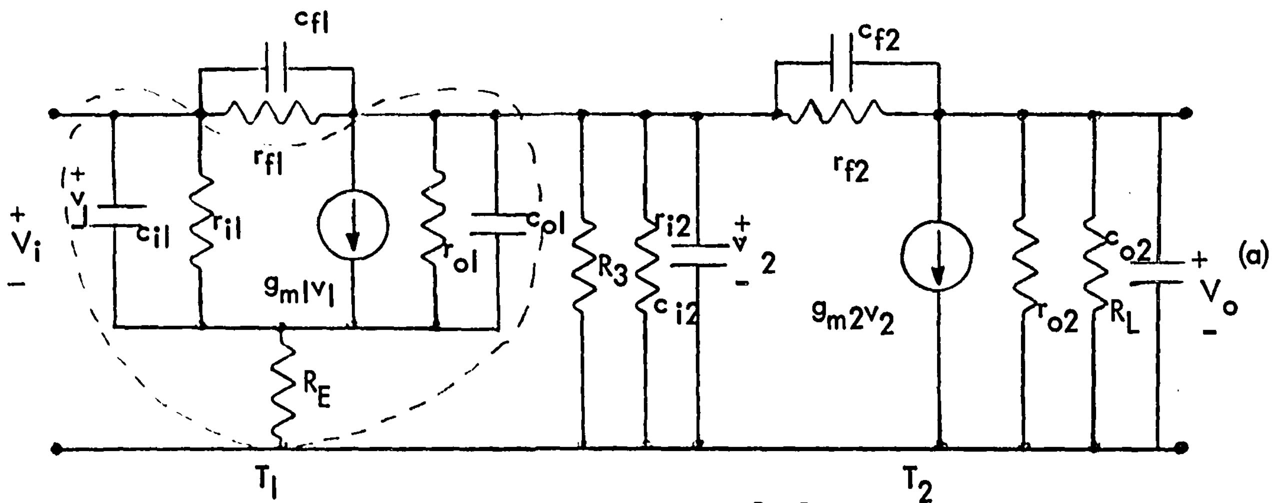

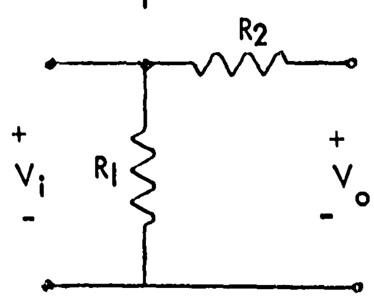

$$h_i = \frac{R_1 R_2}{R_1 + R_2} = R_E$$

(b)

$$h_o = \frac{1}{R_1 + R_2} = \frac{1}{R_L}$$

$$h_r = f_\beta = \frac{R_1}{R_1 + R_2}$$

$$h_f = - \frac{R_1}{R_1 + R_2}$$

FIGURE 5-7 INCREMENTAL MODEL OF PREAMPLIFIER

The circuit in Figure 5-7(a) is reduced to that in Figure 5-8 by assuming the following:

1. $g_{m1} + G_e \gg g_{o1} + g_{i1}$
2. $\dfrac{g_{o1} + sc_{o1}}{1 + g_{m1} R_E} \ll \dfrac{1}{R_3 \parallel r_{i2}} + sC_T$
3. $C_T = c_{i2} + c_{f2}(1 + g_{m2} R_L)$
4. $r_{o2} \gg R_L$
5. $r_{f2} \gg h_{21e} R_L$
6. $s(c_{o1} + c_{i1})$ is negligible.
7. c_{f1} and c_{i1} are dominant with respect to r_{f1} and r_{i1}.

The OPEN LOOP gain, a_v, computed from Figure 5-8 is

$$a_v = \frac{V_o}{V_i} = \frac{g_{m1} g_{m2} R_L R_\pi}{1 + g_{m1} R_E} \times \frac{1 - s\dfrac{c_f(1 + g_{m1} R_E)}{g_{m1}}}{1 + sR_\pi C_T} \tag{5-16}$$

The CLOSED LOOP gain A_v,

$$A_v = \frac{A_{v(o)}\left(1 - s/2P\right)}{\left(1 + s/P\right)} \approx \frac{A_{v(o)}}{1 + s/P} \tag{5-17}$$

where $A_{v(o)} = \dfrac{R_1 + R_2}{R_1}$, $P = \dfrac{g_{m1}}{2c_{f2}\left(1 + g_{m1} R_E\right)}$ and

the zero has been removed as the pole is dominant. The high frequency cutoff determined by P was computed to be 2.5×10^7 rad./sec.

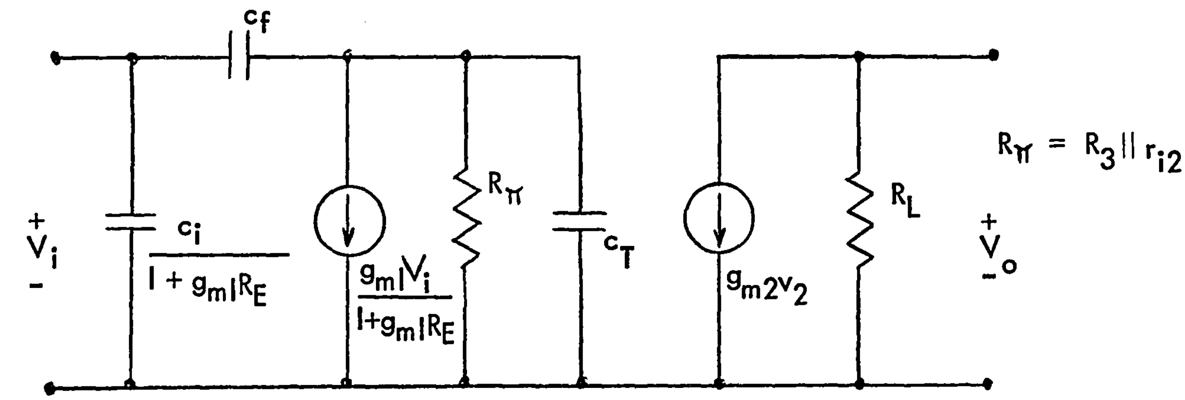

FIGURE 5-8 AMPLIFIER OPEN LOOP MODEL

The amplifier frequency response is shown in Figure 5-9. It should be noted that the computed response via (5-17) compares very favourably with that obtained experimentally.

5.2.4 Neutralization with a Finite Bandwidth Amplifier

Incorporating (5-17) into (5-3) and (5-4) the gain A_v,

$$A_v = \frac{V_o}{e_s} = \frac{2\,SC_s}{G_i - G_f + S\left(C_s + C_i - C_f + \frac{G_i + G_f}{P}\right) + S^2\left(\frac{C_s + C_i + C_f}{P}\right)} \qquad (5\text{-}18)$$

and the input admittance Y_{in},

$$Y_{in} = G_i - G_f + S\left(\frac{G_i + G_f}{P} + C_i - C_f\right) + S^2\left(\frac{C_i + C_f}{P}\right) \qquad (5\text{-}19)$$

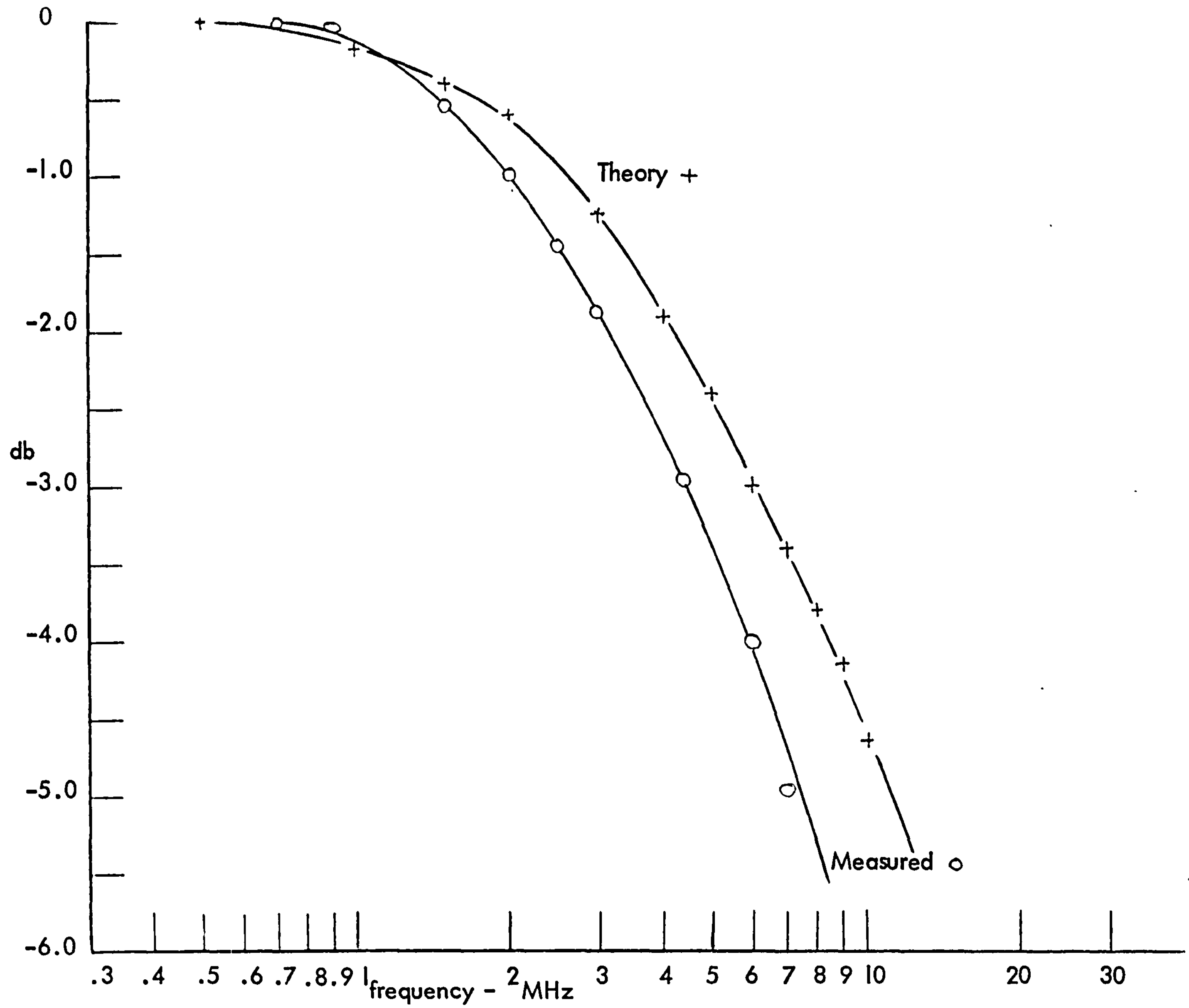

FIGURE 5-9 AMPLIFIER FREQUENCY RESPONSE

Case a $\quad G_i = G_f\,,\ C_i = C_f\,.$

$$A_v = \frac{2C_s}{C_s + \frac{2G_i}{P} + \frac{S(C_s + 2C_i)}{P}} \approx \frac{2}{1 + \frac{S(C_s + 2C_i)}{PC_s}} \qquad (5\text{-}20)$$

$$Y_{in} = \frac{S2G_i}{P} + S^2\frac{2C_i}{P} \approx \frac{S2G_i}{P} \qquad (5\text{-}21)$$

The amplifier bandwidth has been decreased but the input admittance is small and effectively susceptive.

Case b $\quad G_i = G_f\,,\ C_f > C_i\,.$

$$A_v \approx \frac{1}{\left(1 + \frac{S(C_s + C_i + C_f)}{P(C_s + C_i - C_f)}\right)} \cdot \frac{2C_s}{(C_s + C_i - C_f)} \qquad (5\text{-}22)$$

$$Y_{in} \approx - S\,(C_f - C_i) \qquad (5\text{-}23)$$

Here the midband gain has increased, the bandwidth decreased, but the input admittance is negative and susceptive.

Case c $\quad G_f < G_i\,,\quad C_f = C_i + C_s$

The input admittance which now includes C_s is

$$Y_{in} = G_i - G_f + \frac{S(G_i + G_f)}{P} + \frac{S^2 2(C_i + C_s)}{P} \qquad (5\text{-}24)$$

This input admittance can be modelled by a small conductance in parallel with a very small capacitance, where the conductive component is dominant. The gain A_v for this case is

$$A_v = \frac{2SC_s}{G_i - G_f + \frac{S(G_i + G_f)}{P} + \frac{S^2 2(C_s + C_i)}{P}} \tag{5-25}$$

$$A_v \approx \frac{S\,2C_s}{G_i - G_f} \tag{5-25 a}$$

Here the amplifier behaves like a differentiator, which is unsuitable.

5.2.5 The Circuit

The complete amplifier circuit is shown in Figure 5-10. From the circuit it is readily apparent that the input terminal has a dc potential. This potential consists of two parts, the one from the biasing network for the FET, and the second, the external polarizing potential Vp. These two sources act in series to supply the detector polarizing potential. The potentiometer is the adjustment for G_f, it accomplishes this by changing the gain associated with the conductance of (5-4). C_f on the other hand is directly adjustable.

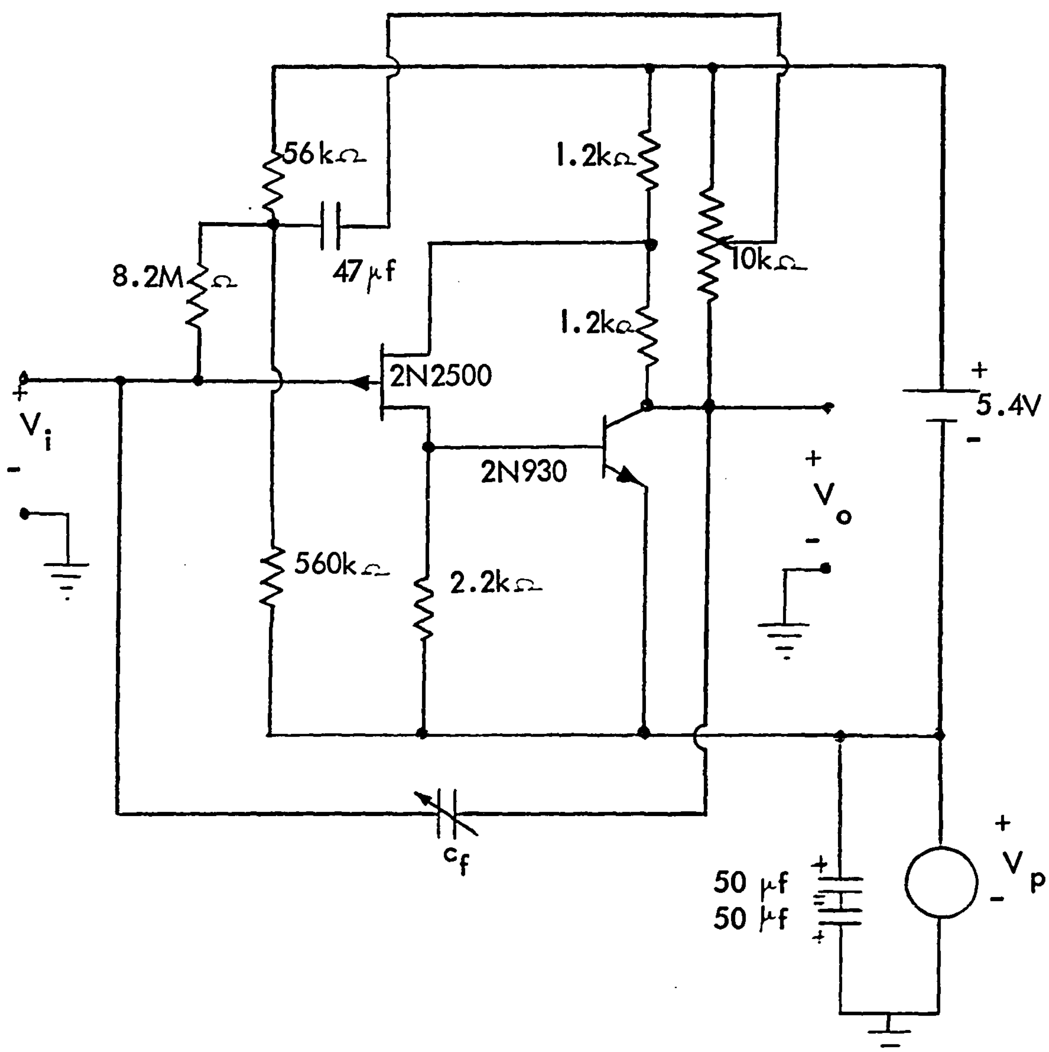

FIGURE 5-10 COMPLETE PREAMPLIFIER

5.3 Signal Conditioning

Due to variations in amplitude, arrival time and rather broad shallow curvature of the detected pulses from the transducer, signal 'conditioning' is required. Further, the amplifier input impedance is extremely high, thus susceptible to noise. The noise manifests itself in several ways. Firstly, there is the low frequency noise or drift, composed of frequencies somewhat below that of the fundamental signal frequency, particularly at the line frequency and its harmonics. Then there is the standard noise associated with the components and circuitry. Lastly, there is that noise associated with the signal itself.

The problem therefore is to develop some technique for determining the time at which the peak of the signal is reached without noise, or at least a minimum of noise interference. There are of course numerous solutions or partial solutions to this problem. For example, extreme care in the shielding of the detector and amplifier. The use of a bandpass filter may prove valuable. Since the signal is almost periodic, sampling, averaging, or one of statistical processing techniques can be used to good advantage. However, these methods are either too costly, complex, insufficient, or require a considerable processing time. Figure 11 illustrates a relatively simple, economic and effective system for 'conditioning' the detected pulses. The purpose of this section is to present that system and the required circuitry.

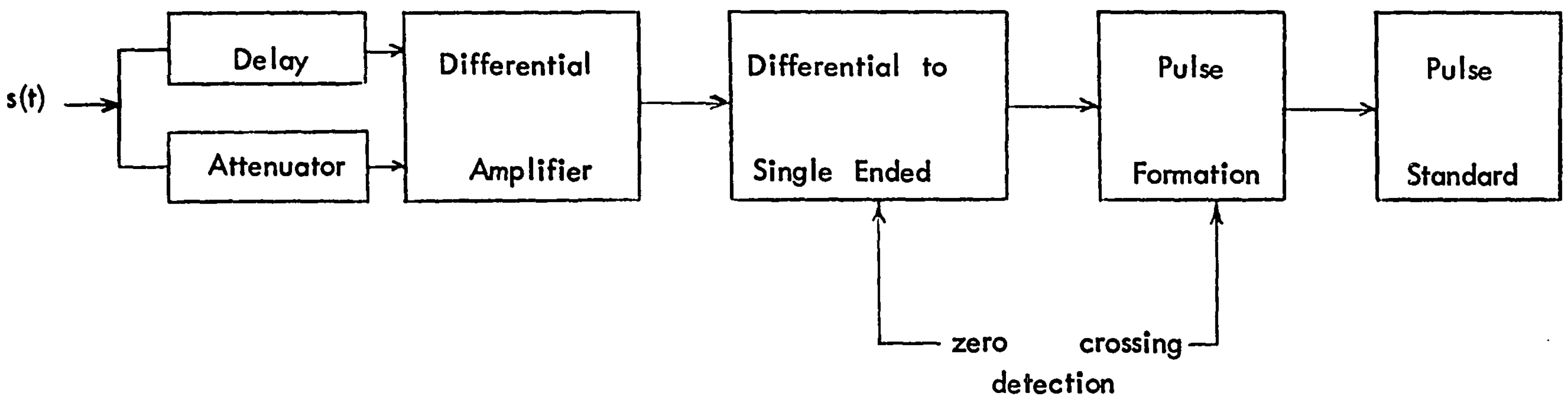

FIGURE 5 - 11 SIGNAL CONDITION

5.3.1 System Design

Referring to Figure 5-11, the basic idea is as follows: The input signal, S(t) is a sequence of pulses. In practice it is found that there is some randomness associated with the amplitude, duration and spacing. It is the purpose of the system to obtain a narrow ($< 1\mu s$) pulse of fixed amplitude whose leading edge bears a known fixed time relationship referred to the signal peak, with a minimum of noise. In order to accomplish this the signal is split twofold. Both paths the one through a delay line and the other through an attenuator, lead to a differential amplifier. The differential amplifier together with delay and attenuator act as a quasi-differentiator. This 'differentiated' signal, is then applied to a zero crossing detector from which a pulse is obtained at the zero crossing of the 'differentiated' signal. This latter pulse is then fed to a monostable multivibrator for standardization. The standardized pulse then has its leading edge delayed by $\tau/2$ from the signal peak, where τ is the time delay of the line. As the amplitude of any component of S(t), including noise, after 'differentiation' is approximately $A\omega\tau$ where A is the amplitude and ω the angular frequency, then it is readily apparent that noise much below the signal frequencies is attenuated by the factor ω_n/ω_s relative to the signal. The noise much above that of the signal frequency, on the other hand, is reduced by the amplifier high frequency cutoff.

To summarize, in the absence of the desired signal, the differential amplifier is presented with approximately equal signals and produces a stable dc level at the output about which some high frequency noise is present. The drift caused by low frequency noise is reduced by a factor of τ , the delay time. The high frequency noise is reduced via the low pass amplifier characteristic. When the signal is present the differential amplifier is presented with unequal signals in such a manner that it yields the approximate derivative of the signal pulse at the output. The zero crossing of this latter signal is delayed by $\tau/2$ from the signal peak and upon detection in the zero crossing detector generates a pulse at $\tau/2$ from the signal peak.

5.3.2 Design Considerations and Circuit Realization

The signal from the detector's amplifier is low level, millivolts, which after 'differentiation' would become microvolts. Hence, it is advisable to additionally amplify the signal prior to 'differentiation'. In this manner the differentiated signal is less susceptible to noise. A high gain amplifier, Keithley model 102BR, with a bandpass characteristic having a high frequency cutoff at either 150KHZ or 1.5MHZ, is placed ahead of the quasi-differentiator.

In order to implement the signal splitting it was necessary to consider the amplifier loading as well as the delay line terminations. The maximum amplifier loading is 4kΩ for full output. The delay line has a characteristic impedance of 1kΩ. As the differential amplifier likes to see balanced sources, then the arrangement illustrated in Figure 5-12 was used. The 500 ohm potentiometer is carefully adjusted to assure equal amplitude signals at e_1 and e_2, otherwise proper 'differentiation' will not take place.

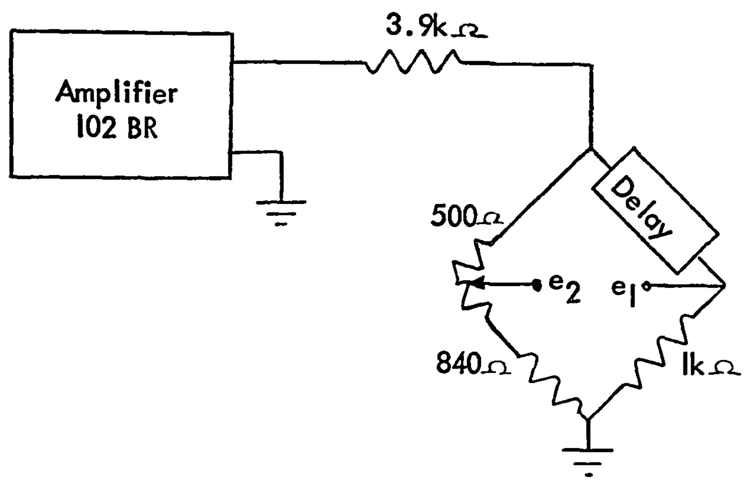

FIGURE 5-12 SIGNAL SPLITTER

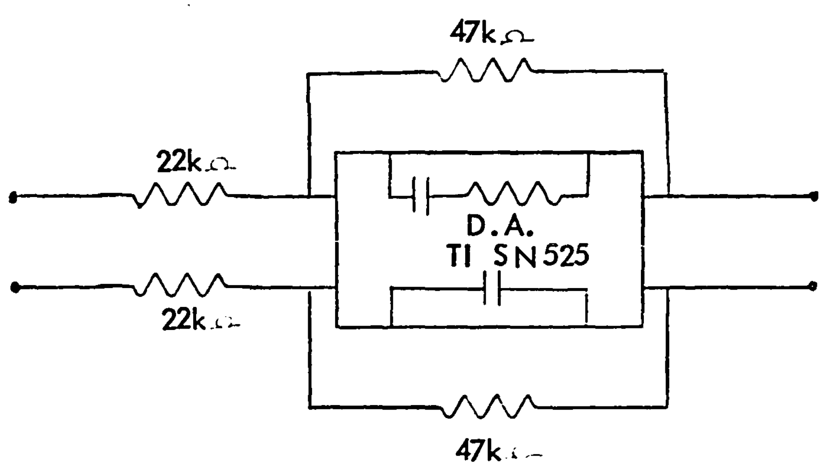

FIGURE 5-13 DIFFERENTIAL AMPLIFIER

The differential amplifier was a Texas Instrument SN525 operational amplifier arranged to have a gain of 2, and being frequency compensated, shown in Figure 5-13. The zero crossing detector (see Figure 5-14) is made up from a high gain limiting amplifier, or clipper, followed by a differentiator and clipper. The limiting amplifier is a three stage non saturating differential amplifier as shown in Figure 5-15. The transistors were carefully selected in pairs for matching with respect to both h_{FE} and V_{BE} so that the limiting of the basic unit would be symmetrical. The overall amplifier then had dc shunt feedback applied to maintain the proper bias levels for symmetrical limiting. The overall gain is approximately 35×10^4. A millivolt change at the input gave rise to 3.5 volt swing at the output. The bias was arranged such that the maximum collector swing was less than $\pm$ 5 volts, otherwise the maximum V_{BE} will be exceeded for these transistors.

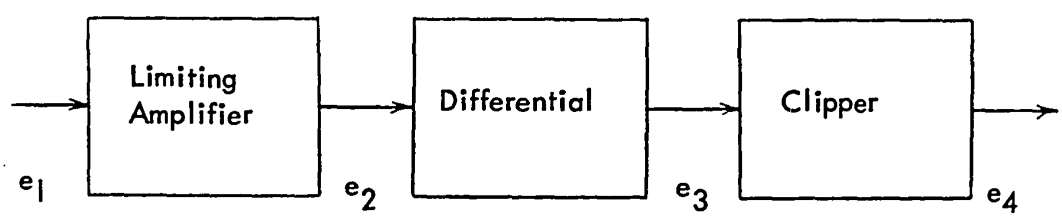

FIGURE 5-14 ZERO - CROSSING DETECTOR

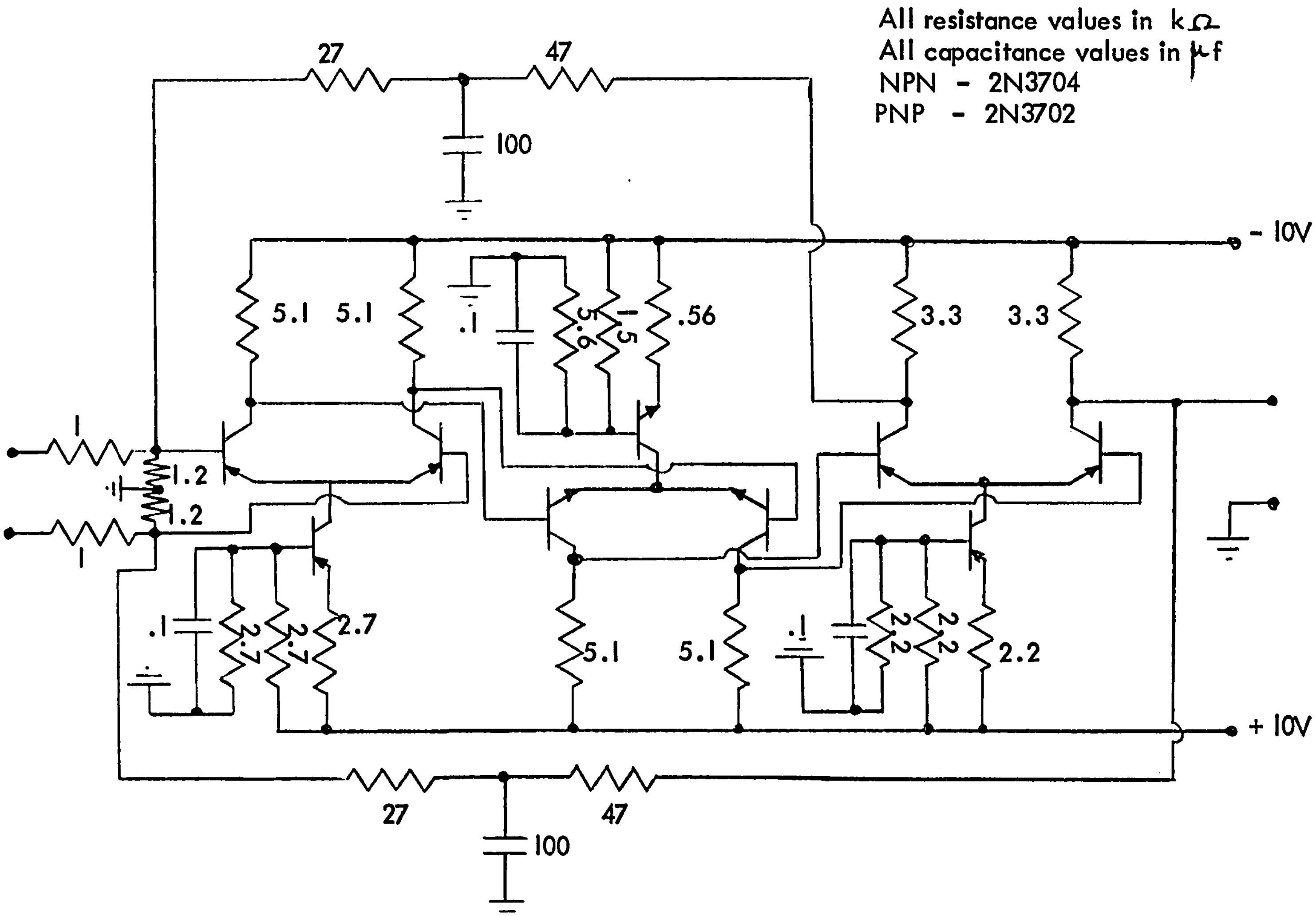

FIGURE 5-15 LIMITING AMPLIFIER

The differentiator was a simple RC network with diode clipper as illustrated in Figure 5-16. The additional transistor switch was used to amplify the pulse in order to drive the monostable pulse standardizer shown in Figure 5-11. The monostable is a Wang Laboratories type 5204.

Four identical stages were required to complete the measurements over three intervals. After constructing the second unit, the selection of additional matched transistors for the limiting amplifier became impossible for lack of additional stock. This led to the Texas Instruments SN525 operational amplifier with its intrinsic large gain, that is, 5×10^4 which was not being fully utilized. It was found that with only dc feedback, as shown in Figure 5-17, almost the full loop gain could be utilized. The only change necessary was additional gain before differentiating and clipping. The arrangement for this circuitry is shown in Figure 5-18.

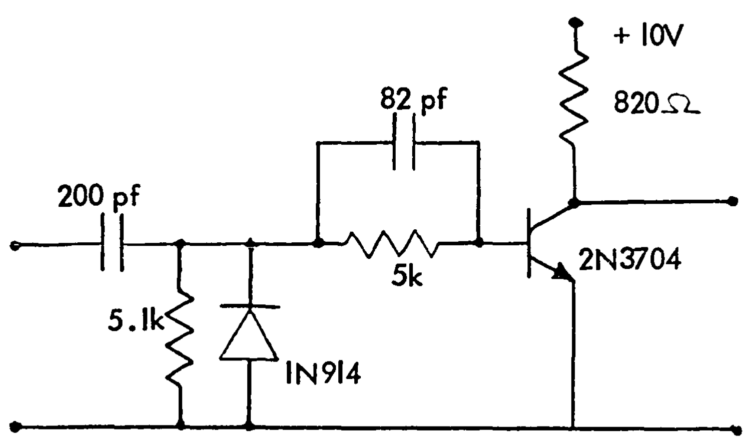

FIGURE 5 - 16 DIFFERENTIATOR

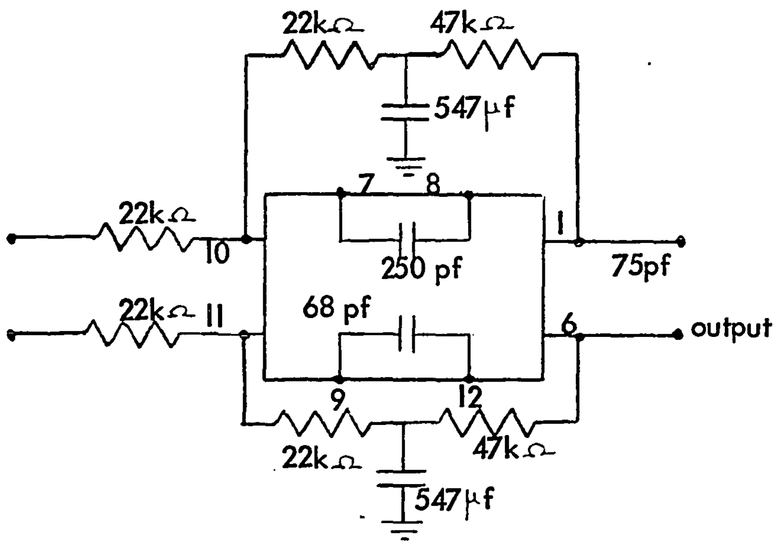

FIGURE 5-17 DIFFERENCE AMPLIFIER AND LIMITER

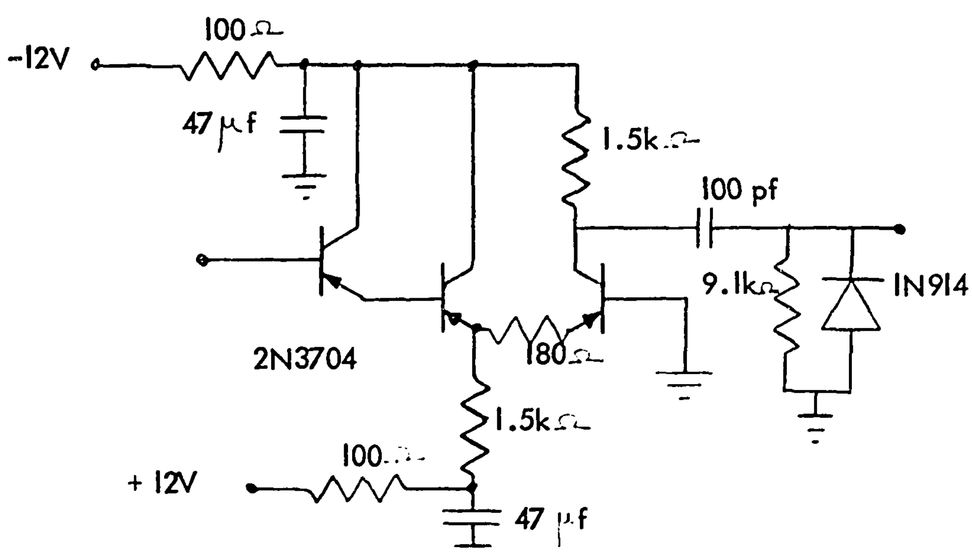

FIGURE 5-18 AMPLIFIER, DIFFERENTIATOR AND CLIPPER

The system performance was reasonably satisfactory. A 50 millivolt signal level at the amplifier (Keithly 102BR) output was more than ample to repetitiously generate a 0.5μs pulse at the signal peak. However, a slight frequency dependance was observed; it was particularly noticeable in the 0.5 kHz to 1 kHz band. Once adjusted for a particular operating frequency, then providing the frequency did not vary by more than ten per cent it was well within the accuracy limitations.

5.3.3 Signal Recording

The recording system is straightforward and simple as illustrated in Figure 1-19. The transit time information is contained in the pulse width of the Flip Flop output. The output from the Flip Flop is filtered, amplified and then recorded.

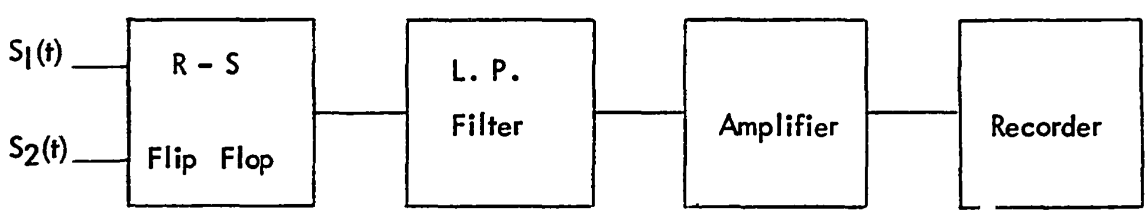

FIGURE 5-19 THE RECORDING SYSTEM

The R-S Flip Flop is a Wang Laboratories type 5201. The filter incorporated into the unit was a Burnell TCL 10K, with a 200 Hz cutoff frequency. A 1kHz low pass filter was also utilized. The amplifier is a Sanborn model 656-3400 and the recorder is a Honeywell model 906B visicorder.

The output from the Flip Flop is equivalent to pulse duration modulation (38) (39). The signal that is modulated is the average transit time and the modulating signal is the variation in it. The simplest and most common method for deriving the signal is the one used here, a low pass filter. Hence, variations in transit time to 1kHz can be detected.

Some difficulty was experienced in using the recorder particularly prevalent at low writing speeds. The record was rather broad, which reduced the readout accuracy considerably. The recording system was calibrated by using a test circuit to generate known transit times at various frequencies. The scheme is shown in Figure 5-20and the calibration curves in Figure 5-21. Additionally, the signal frequency was recorded on one channel of the recorder.

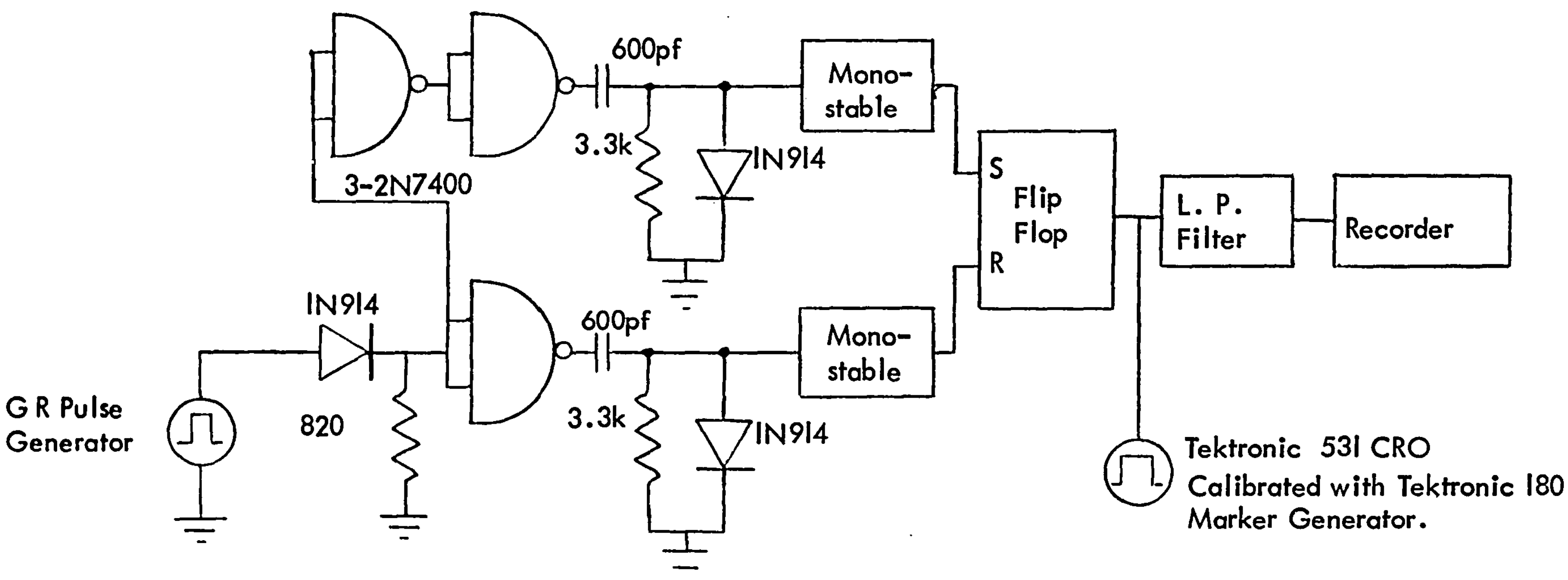

FIGURE 2D TEST CIRCUIT

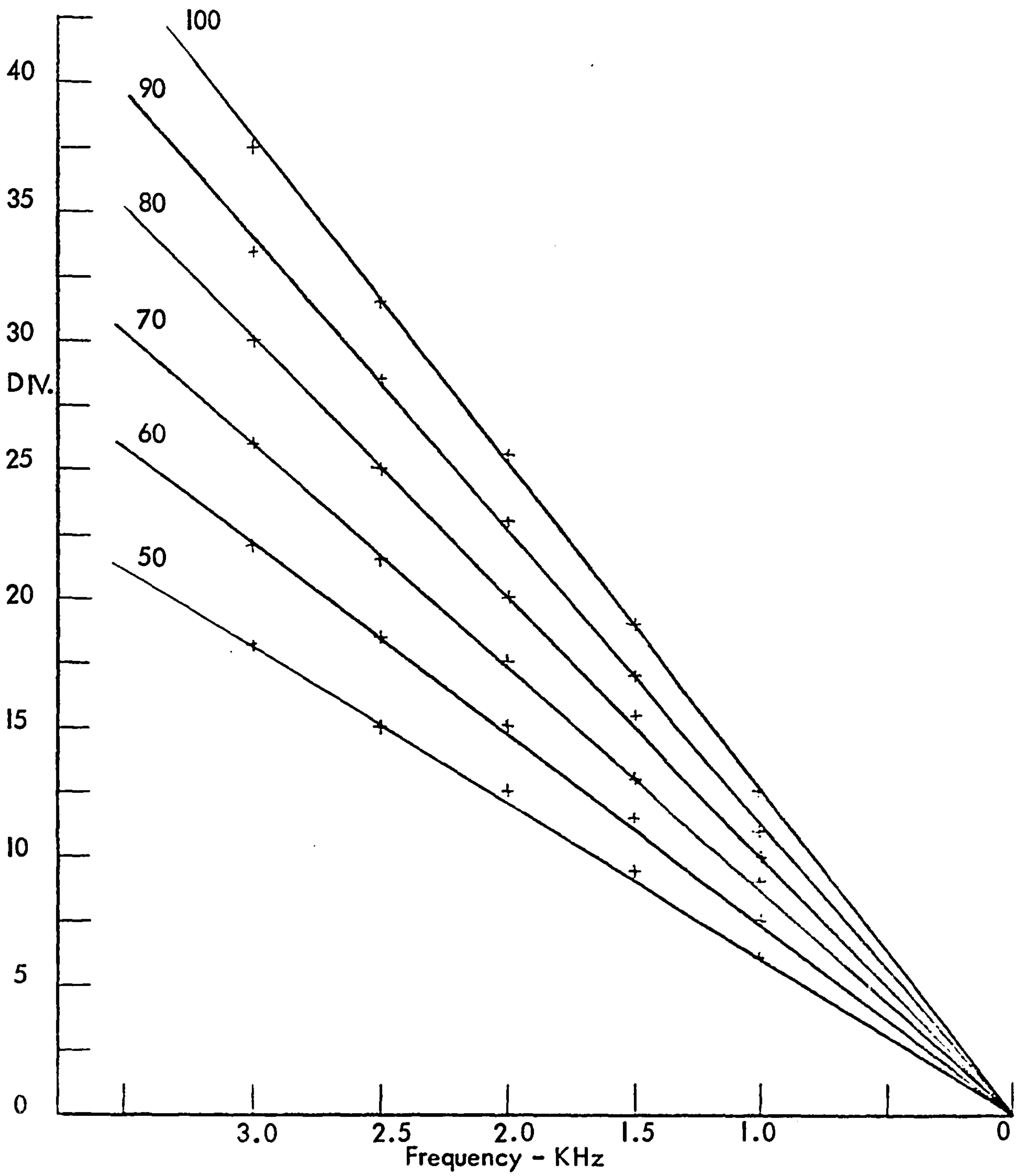

FIGURE 21 RECORDER CALIBRATION

CHAPTER VI

EQUIPMENT, OPERATION AND RESULTS

6.1 Introduction

A simple intermittent wind tunnel was specifically constructed to investigate the Ion Tracer Technique for measuring supersonic air velocities. The details and calibration of this wind tunnel are described, and the equipment and its arrangement for the tracer method are similarly set forth. This is followed by a description of the operating procedure and the results thus obtained are given.

6.2 Wind Tunnel Description

The wind tunnel used in the tests was of the intermittent type (40). The vacuum intermittent system used has one end open to the atmosphere and the other connected to a vacuum tank. The advantages with this type are found in its simplicity, high pressure ratios and constant stagnation conditions (atmospheric). The main disadvantage is the short running time.

The schematic diagram for such a system is shown in Figure 6-1. Atmospheric air is drawn into the system by the vacuum tank. The air passes through a convergent-divergent nozzle where it is speeded up from the intake to the test section speed. The nozzle mach number determines the speed in the test section. The flow remains supersonic providing the ratio of vacuum tank pressure to atmospheric pressure is less than the critical ratio (41).

The test section is a constant area cylinder. This cylinder is connected to the vacuum receiver by a fast opening valve. In addition, the vacuum tank is connected to a vacuum pump through a shutoff valve.

The actual experimental system operation is considerably more complex than just described. The complexity arises from the friction present in the system. With friction in the test section, the requirements for supersonic shockless flow are that, (i) the test length be less than $L_{max.}$, the length for which the exit mach number is l, (ii) the test section exit pressure be less than p^*, the pressure for mach l, (iii) the vacuum tank pressure be less than the tube exit pressure, and (iv) the inlet mach number be sufficiently large that the exit mach number is greater than 1 (4l).

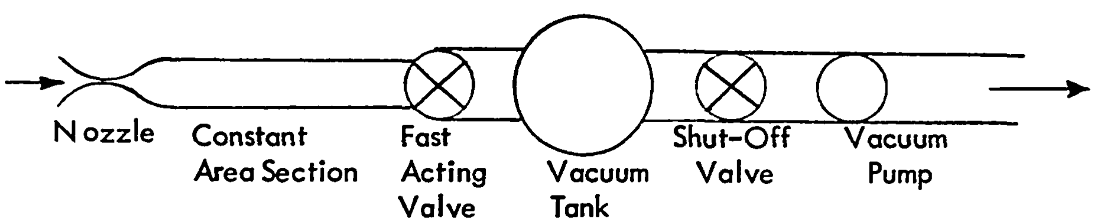

FIGURE 6 - 1 WIND TUNNEL SCHEMATIC

The nozzle was constructed from polystyrene. Two units were made, the one designed for mach 1.8, and the other for mach 3.0. The mach 1.8 nozzle has an area ratio of 1.439 and the other 4.234, corresponding to isentropic mach numbers of 1 .8 and 3.0 (42) respectively. The mach 3.0 nozzle was rarely used because of its poor design (short, sharp expansion characteristic), and to avoid possible condensation problems . The complete inside dimensions for the mach 1.8 nozzle are listed in Table 6-1. The exit diameters of both units were 0.615 inches to match the test section diameter.

The test section was a length of polystyrene tubing with nominal dimensions - $^7/8$ "O.D. by $^5/8$" I.D. Its length was arrived at only after determining the most suitable length free of shock waves. This was accomplished experimentally through a preliminary test series using successively shorter lengths and measuring the static wall pressures. This length was found to be 8.5 inches.

The arrangement of wall pressure taps for calibrating the test section is shown in Figure 6-2. The wall static pressures were measured using the multiple mercury manometer, illustrated in Figure 6-3. The readings were frozen by a clamping device for ease in recording the results. The static wall pressure measurements for the 8.5 inch length are given in Table 6-2. From the table, it will be noted that the first tap pressure for the mach 3.0 nozzle is inconsistent with the remainder. This can be attributed to its inadequate expansion characteristic.

Utilizing the pressure measurements in Table 6-2, the velocity in the test section was computed. This required determining the test section inlet

TABLE 6 - 1

CONVERGING		DIVERGING	
x in.	y in.	x	y
0	0.5126	0	0.5126
0.1536	0.5139	0.0512	0.5127
0.2564	0.5165	0.1024	0.5134
0.3588	0.5200	0.1641	0.5153
0.4613	0.5250	0.2153	0.5181
0.5637	0.5322	0.2564	0.5213
0.6665	0.5423	0.3468	0.5302
0.7655	0.5568	0.4717	0.5431
0.8407	0.5709	0.5927	0.5556
0.8818	0.5806	0.7177	0.5677
0.9225	0.5919	0.7983	0.5750
0.9838	0.6129	0.9233	0.5846
1.0443	0.6387	1.0443	0.5935
1.1088	0.6713	1.1693	0.6004
1.1693	0.7132	1.2902	0.6060
1.2298	0.7637	1.4959	0.6120
1.2902	0.8213	1.6612	0.6144
1.3548	0.8818	1.8144	0.6150
1.3950	0.9225		

CONTRACTION xx = 0 EXPANSION

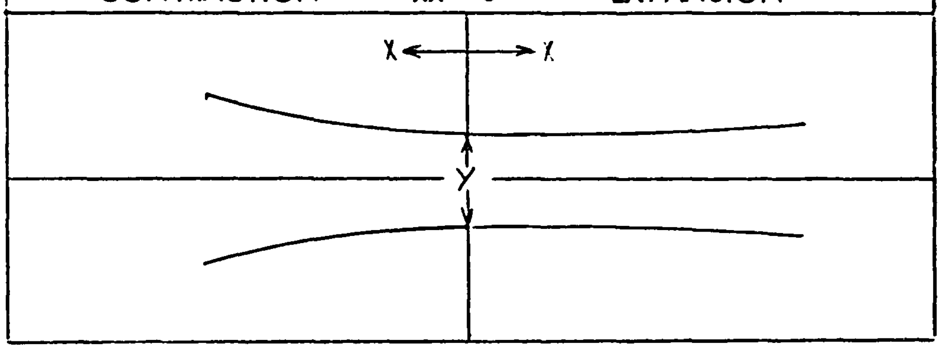

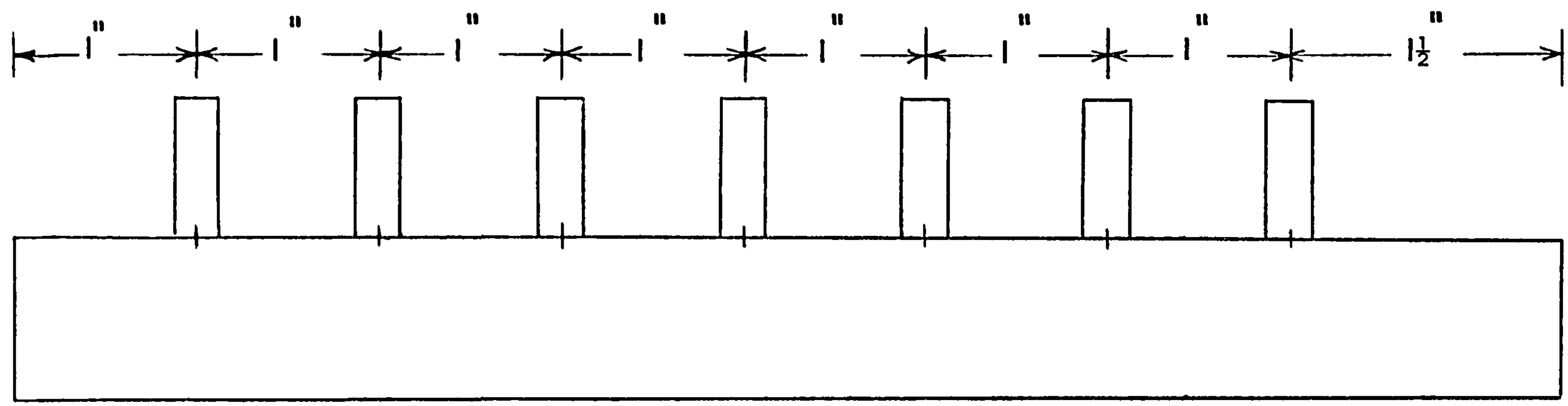

FIGURE 6-2 PRESSURE TAP ARRANGEMENT

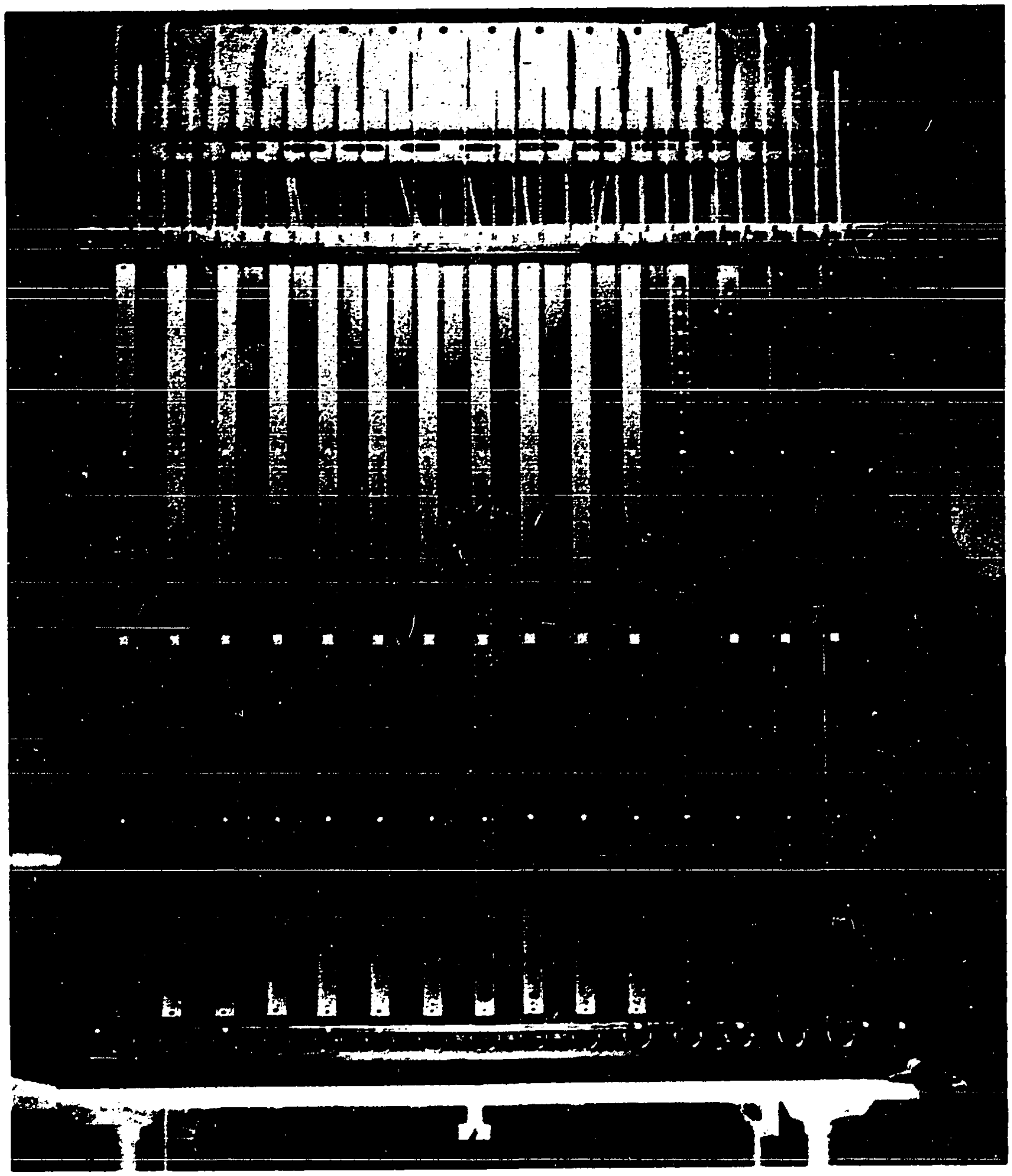

FIGURE 6-3. MULTIPLE MERCURY MANOMETER.

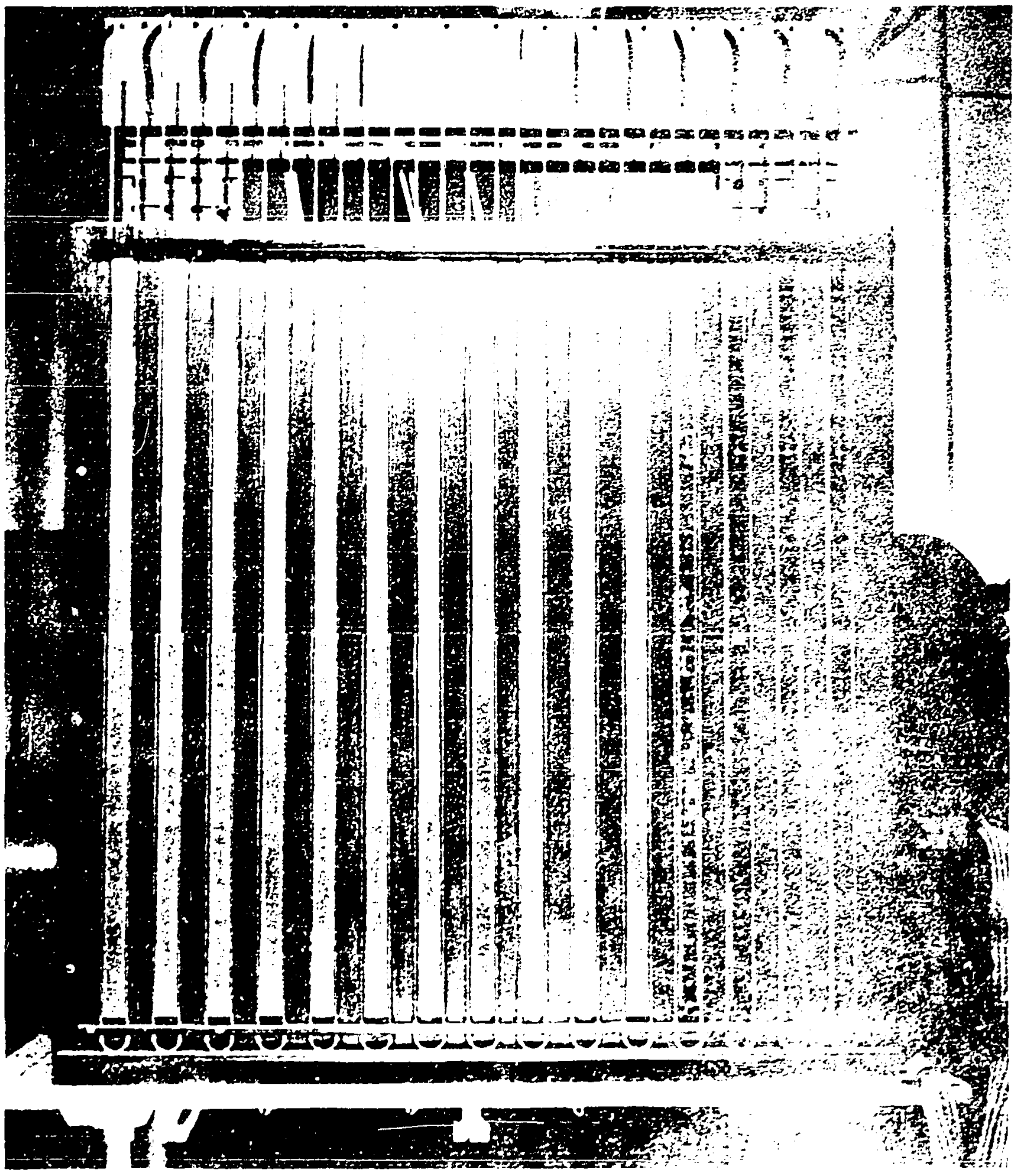

FIGURE [illegible]. MULTIPLE MERCURY MANOMETER

TABLE 6-2 TEST SECTION - STATIC WALL PRESSURE MEASUREMENTS --- in. Hg.

	1	2	3	4	5	6	7	Ref.
1.	5.65	5.40	5.20	4.60	4.10	3.80	3.65	-17.95
2.	5.65	5.40	5.20	4.65	4.10	4.00	3.75	-18.00
3.	5.65	5.40	5.20	4.70	4.15	3.90	3.70	-18.00
4.	3.85	3.63	3.24	2.97	2.58	2.35	1.87	-19.85
5.	3.83	3.60	3.23	2.97	2.58	2.37	1.90	-19.85
6.	3.85	3.60	3.23	3.00	2.60	2.40	1.90	-19.85
7.	6.90	7.10	6.85	6.68	6.40	6.10	6.10	-19.85
8.	6.93	7.10	6.85	6.70	6.35	6.20	6.15	-19.85
9.	6.93	7.10	6.88	6.70	6.40	6.30	6.20	-19.90
10.	7.00	7.20	6.95	6.83	6.50	6.35	6.15	-19.88
11.	7.00	7.20	6.95	6.83	6.55	6.37	6.17	-19.85
12.	7.00	7.20	6.95	6.83	6.55	6.37	6.15	-19.85

NOTES: For Runs 1 - 3 P_o = 29.600 in. Hg., T = 80.7 °F., M = 1.8 Nozzle
4 - 6 P_o = 29.732 in. Hg., T = 71.0 °F., M = 1.8 Nozzle
7 - 9 P_o = 29.745 in. Hg., T = 70.5 °F., M = 3.0 Nozzle
10 - 12 P_o = 29.788 in. Hg., T = 70.1 °F., M = 3.0 Nozzle

conditions. The inlet pressure, synonymous with the nozzle exit pressure, was found by extrapolating the listed pressures. The tube inlet mach number for the mach 1.8 nozzle was computed by assuming the flow is isentropic to the nozzle throat and the flow is adiabatic in the entire system. However, for the mach 3.0 nozzle isentropic flow was assumed throughout and the mach number then determined solely by the pressure ratio. This appeared to be the only valid approximation in keeping with the experimental evidence. The resultant longitudinal velocity profile for each nozzle is shown in Figure 6-4. The velocities in Figure 6-4 have been standardized to an ambient temperature of 71°F. and the vertical lines shown indicate the spread in values.

The velocity profile for the mach 1.8 case, including the spread, indicated a linear relationship with distance. This result is in good agreement, 4%, with

$$\frac{dU_2}{U_2} \Bigg/ \frac{dU_1}{U_1} = \frac{M_2^2}{1 - M_2^2} \Bigg/ \frac{M_1^2}{1 - M_1^2} \qquad (6\text{-}1)$$

derived from Shapiro's[4] Equation (6-13). U is the velocity, M is mach number, and the subscript is the measurement point.

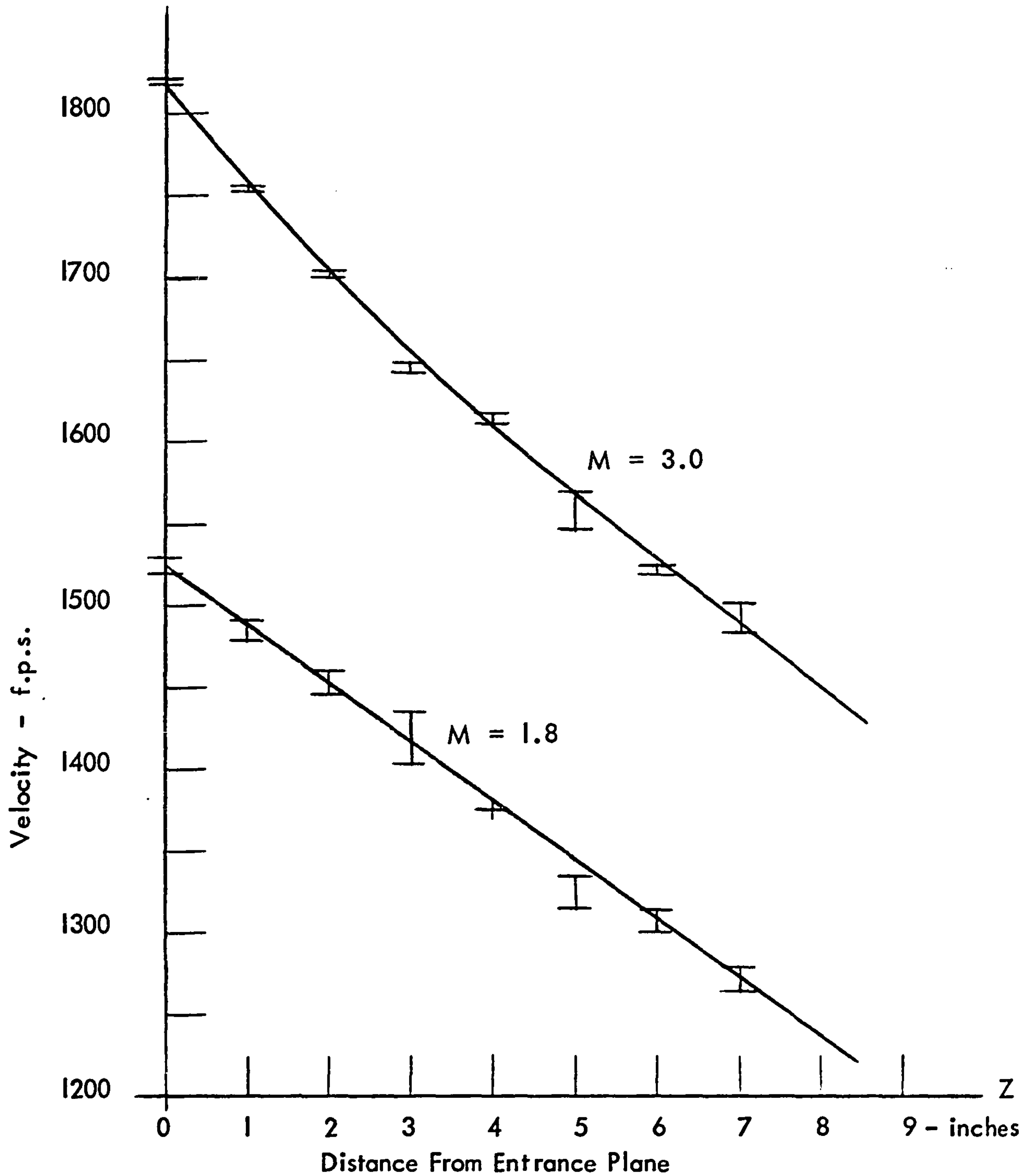

FIGURE 6-4 VELOCITY IN THE TEST SECTION

6.3 Ion Tracer Technique Equipment

The general arrangement of equipment specifically used for the measurement of air velocity by the ion tracer method is shown in Figure 6-5. The following are indicated in this illustration: On the extreme left is an oscilloscope for monitoring and measuring any signal voltages in the system. Adjacent to the oscilloscope is the wind tunnel consisting of the nozzle and constant area test section contained in a lucite enclosure. Next to the tunnel is the rack cabinet which supports the electronic circuits and apparatus for the shutter. The compressed air cylinder for the shutter supply can barely be seen through the legs of the lucite enclosure. On the right hand side is the recorder with its amplifier. Last but not least is the vacuum tank, making up the entire background.

6.3.1 Test Section

Starting with the first item of consequence, the tunnel, it is better illustrated in Figure 6-6 and 6-7. The lucite enclosure, in the main, serves as an added safety feature for the Po -210 source. The auxiliary functions are to support both the test section and the three-dimensional platform. The constant area section is modified from that shown in Figure 6-2 to that of Figure 6-8, and shown pictorially in Figure 6-9. Mention should be made that test sections with 1.5 inch and 1.25 inch detector probe spacing were also used. These changes were necessary in order that the alpha particles could be injected, and the silver detector probes be deposited on the machined wall edges.

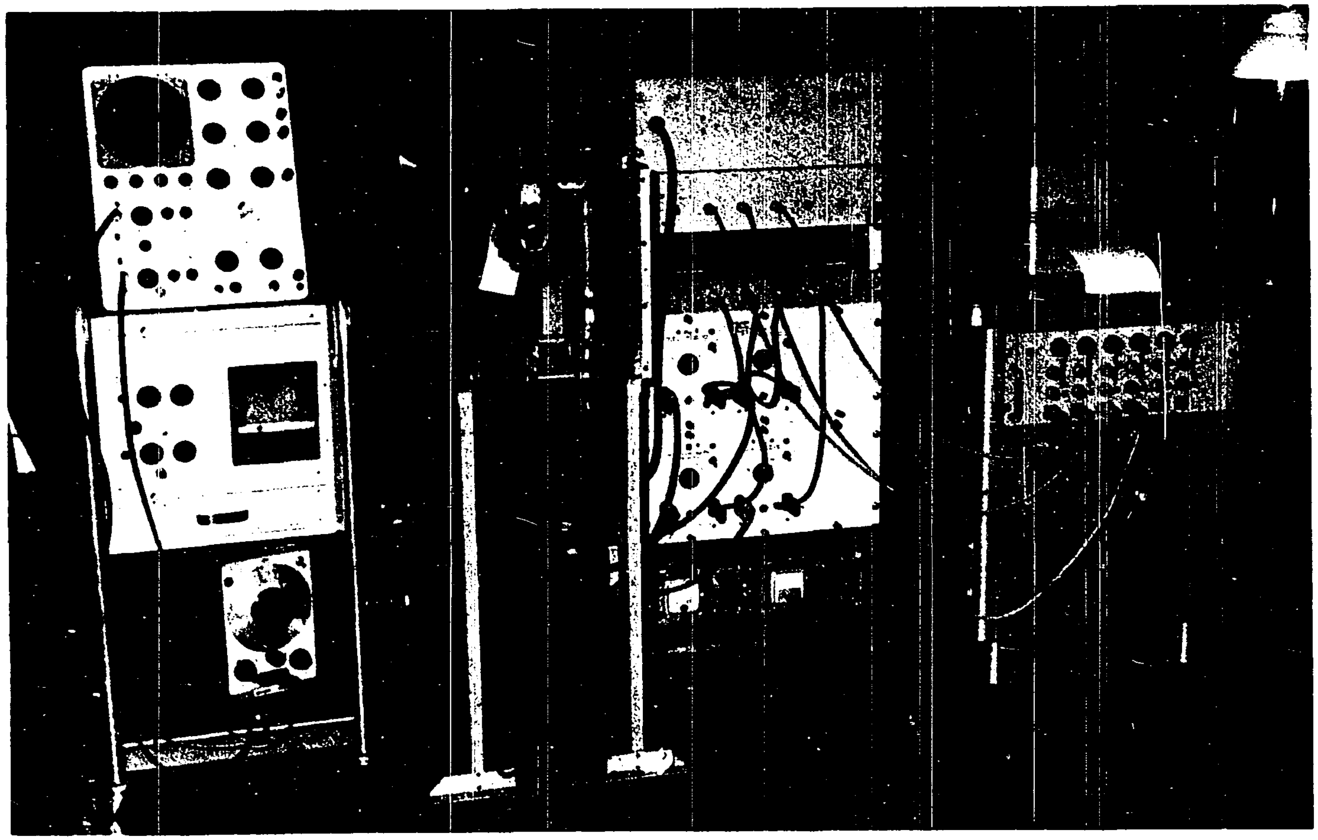

FIGURE 6-5. GENERAL ARRANGMENT OF APPARATUS.

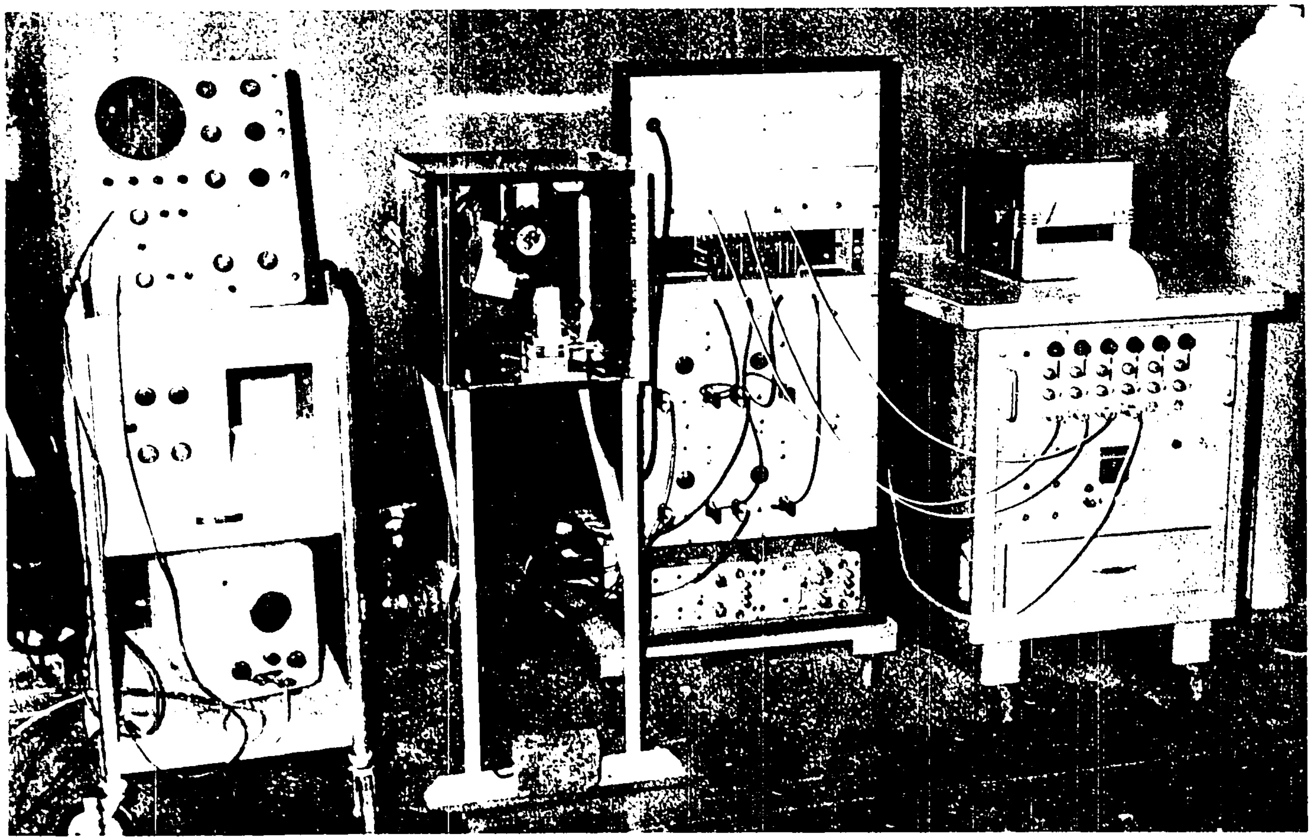

FIGURE 6-5. GENERAL ARRANGMENT OF APPARATUS.

FIGURE 6-6.
TEST SECTION
FRONT VIEW.

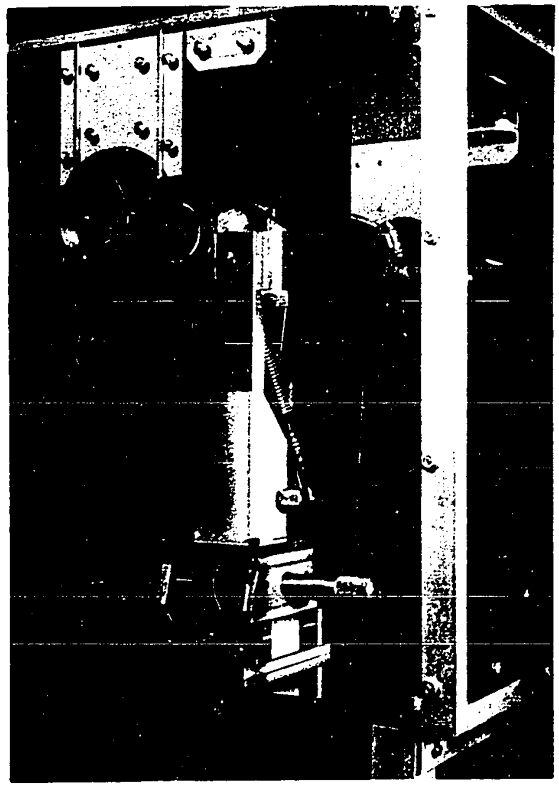

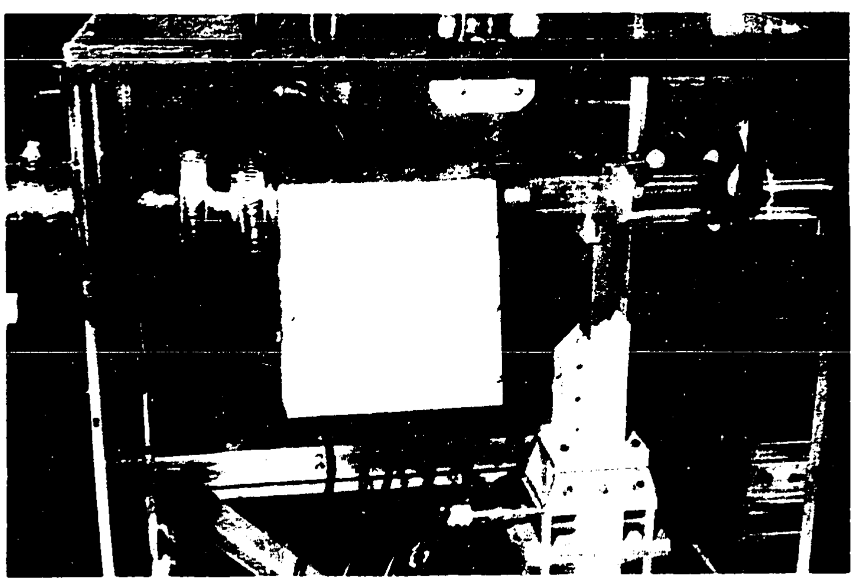

FIGURE 6-7. TEST SECTION SIDE VIEW.

FIGURE 6-6.
TEST SECTION
FRONT VIEW.

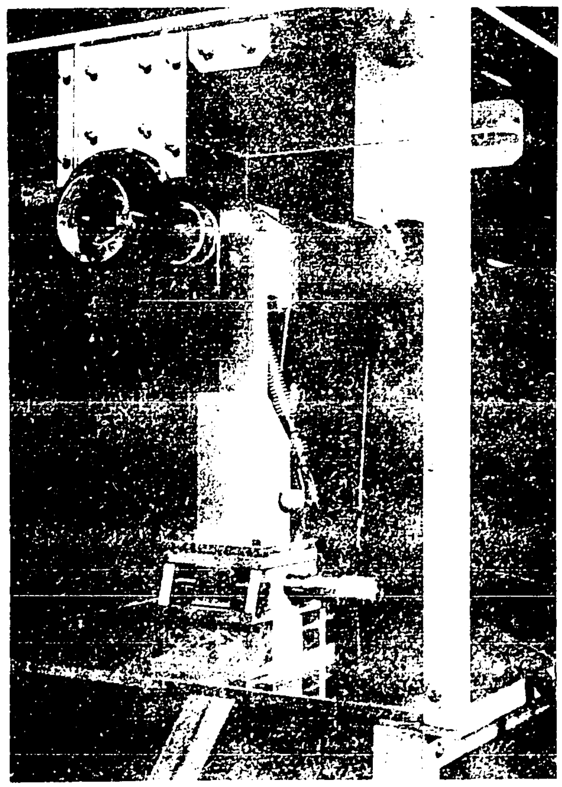

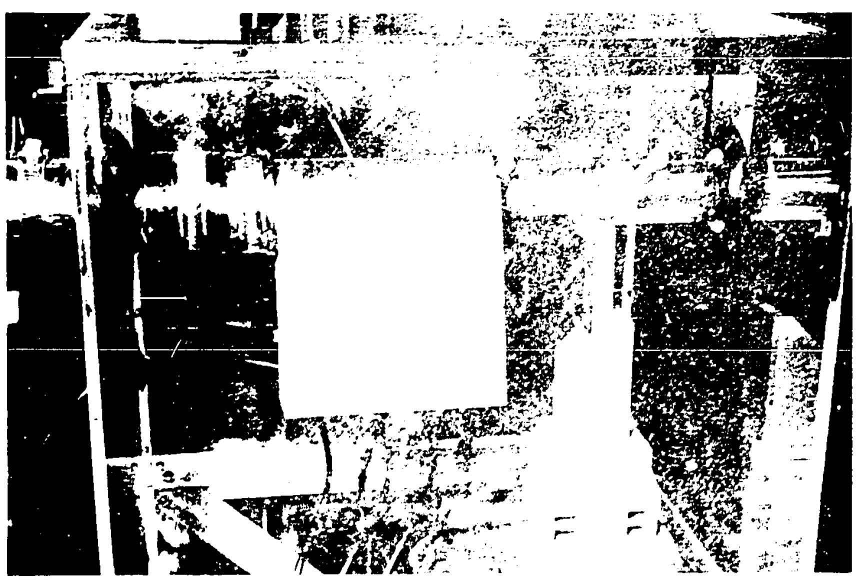

FIGURE [illegible]

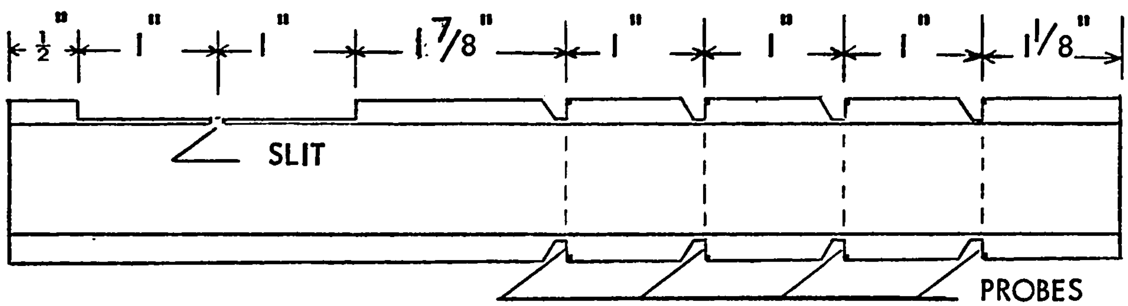

FIGURE 6-8 TEST SECTION PROBES

The test section area containing the detector probes is surrounded by a 2 inch diameter brass shield, 5 inches long. The test section is held in the shield by two supports, one at the front and the other at the rear. However, these supports are isolated from direct contact with the shield by rubber "O" rings, as seen in Figures 6-10 and 6-11. The "O" rings were used to reduce the transmission of vibrations to the shield, which is physically connected to the preamplifiers. The rear support, a 2 inch O.D. aluminum coupling, is joined to the fast acting valve extension by a piece of trygon tubing as seen in Figure 6-7.

6.3.2 Alpha Particle Injection and Interruption

The Po -210 source slides into the dental turbine support block, which in turn is attached to the three-dimensional platform, as shown in Figures 6-6 and 6-12.

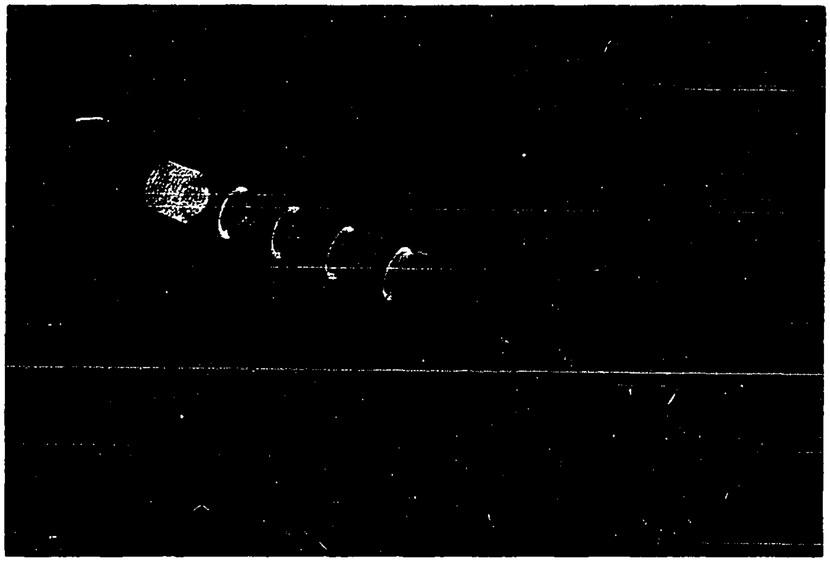

FIGURE 6-9. CONSTANT AREA TEST SECTION – FANNO TUBE.

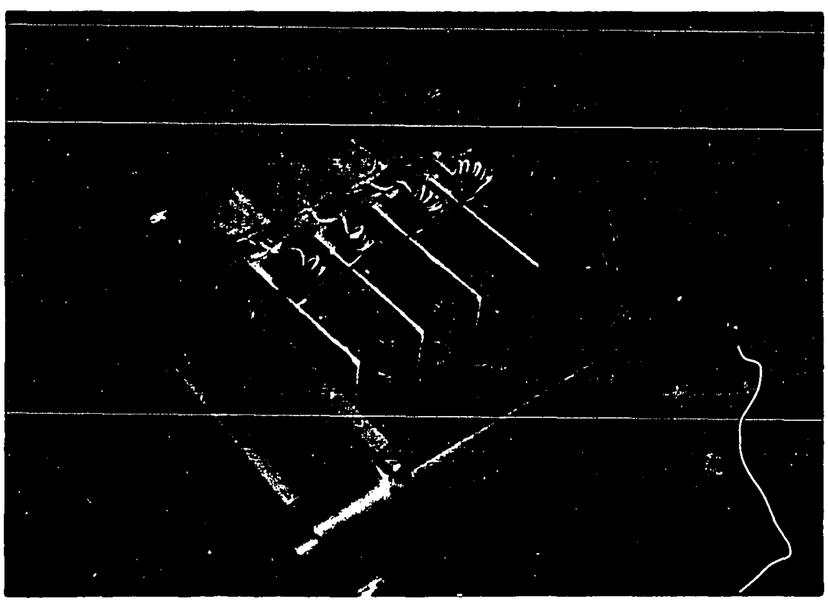

FIGURE 6-10. DETECTOR SHIELD AND AMPLIFIERS.

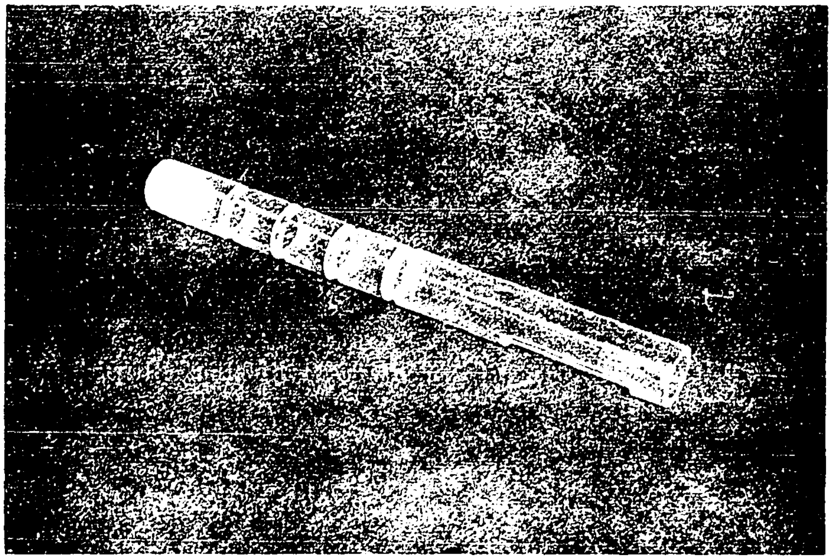

FIGURE 6-9. CONSTANT AREA TEST SECTION – FANNO TUBE.

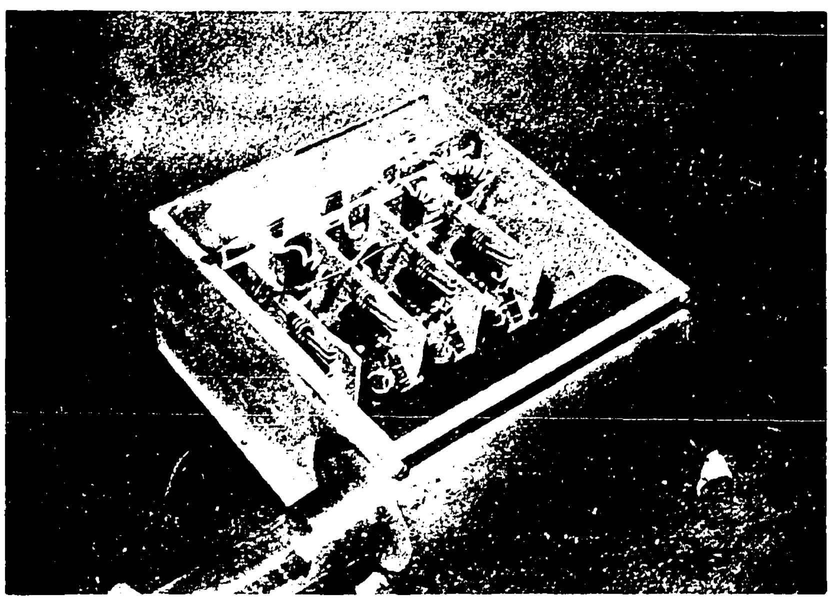

FIGURE 6-10. DETECTOR SETUP AND AMPLIFIERS

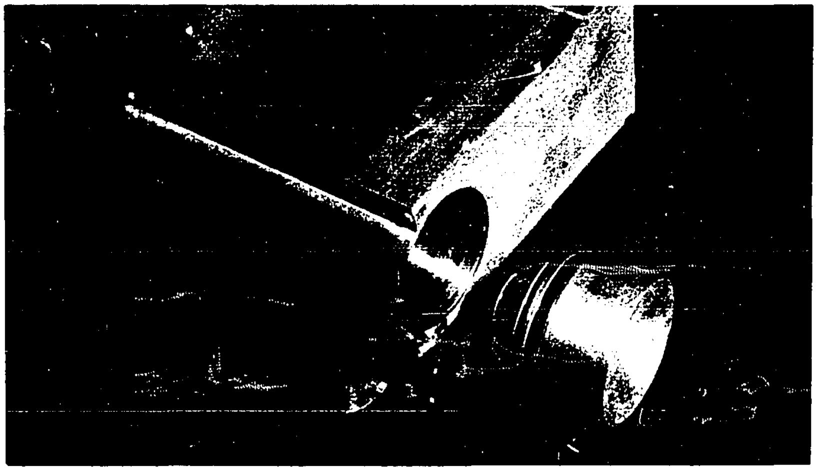

FIGURE 6-11. COUPLING WITH 'O' RINGS AND SHIELD.

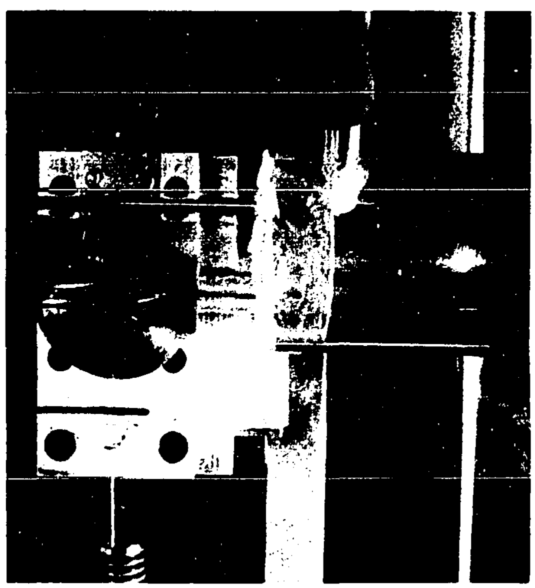

FIGURE 6-12. ALIGNMENT OF SOURCE, SHUTTER AND SLIT.

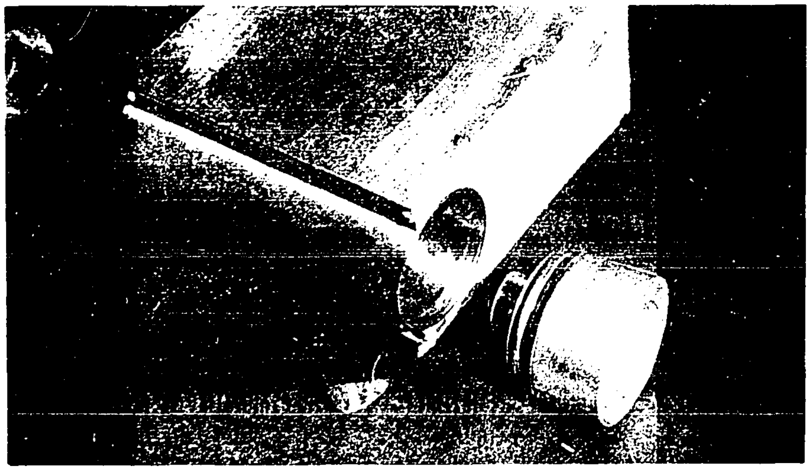

FIGURE 6-11. COUPLING WITH 'O' RINGS AND SHIELD.

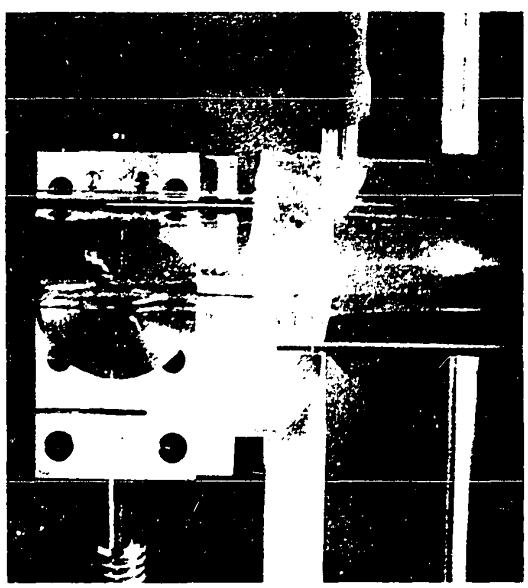

FIGURE 6-12. ALIGNMENT OF SOURCE, SHUTTER AND SLIT.

The collimated alpha particle beam from the Po -210 source is injected into the test duct through the slit shown in Figure 6-8. The slit was milled out on one side only of the constant area tube. The outside wall around the slit was milled flat to better accomodate the shutter. The slit is sealed with a 1.5×10^{-4} inch mylar film glued to the tube wall with epoxy. This arrangement was found more than adequate to maintain the prevailing pressure conditions, and to allow the free passage of alpha particles into the duct. Alignment of the beam and shutter with the slit, Figure 6-12, is carried out with the three-dimensional platform illustrated in Figure 6-6.

The beam is interrupted by a rotating shutter. The shutter is a thin aluminum disc driven by a Siemens Sirona D dental turbine. The disc is 3.0 cm. in diameter, having either 2 or 4 equally spaced slits 1 x 10 mm. The disc is attached to a mandrel and held by a friction grip sleave to the turbine rotor. The complete air system for the turbine is shown in Figure 6-13. The compressed air for the unit is obtained from a high pressure air cylinder. A coarse reducing valve limits the supply pressure to 60 p.s.i., the maximum allowed. Following this valve there is a filter, another reduction valve, oil nebulizer and oil separator. The filter removes any dust or moisture remaining in the air. The fine reduction valve controls the pressure between shutoff and 60 p.s.i. The nebulizer mixes the air with a light oil required for the turbine bearings. Lastly, the oil separator removes any residual oil from the returning spent air before allowing it to escape. The system is mounted on a panel and located at the top of the rack in Figure 6-15.

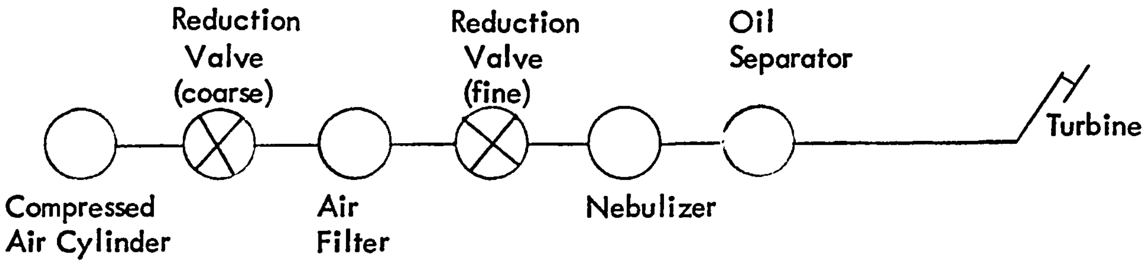

FIGURE 6-13 TURBINE DRIVE SCHEMATIC

6.3.3 Electronic Apparatus

The preamplifiers are situated directly below the detector shield and housed in an integrally connected aluminum case, as illustrated in Figures 6-10, 6-11 and 6-14. Their physical arrangement is shown in Figure 6-10. It should be noted that the amplifiers are fixed to an aluminum plate which is firmly held in two rubber lined grooves to reduce vibration. These amplifiers are powered by individual 5.4 volt mercury batteries contained in a plastic case at the bottom. The probes are connected to the amplifier with No. 44 wire through holes in the shield. The amplifier impedance adjustments referred to in Chapter V are made through the holes shown in Figure 6-14. The outgoing signal is taken from the four BNC connectors seen in Figure 6-14. The additional connector shown is for supplying the polarizing voltage.

The rack cabinet, Figure 6-15, contains the major share of electronic components. Starting from the bottom, there are two D.C. power supplies for the signal conditioning circuits. Directly above, and occupying approximately half the

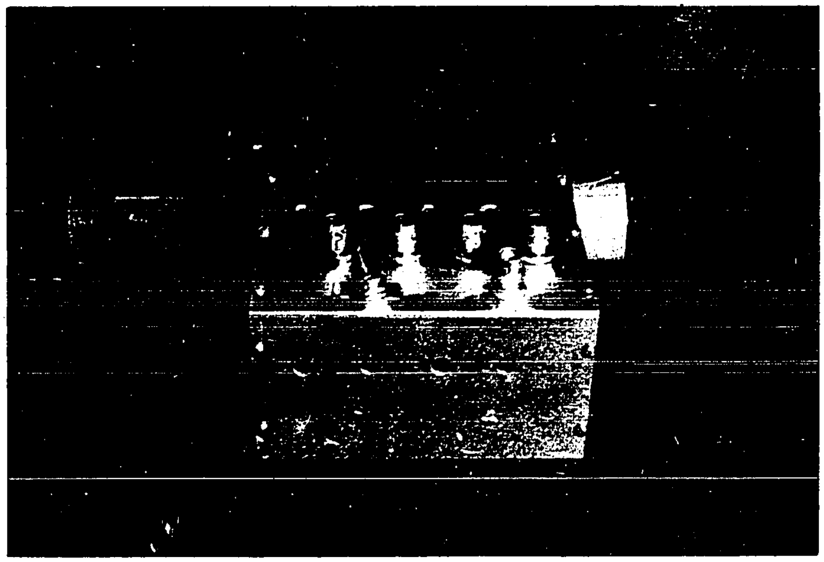

FIGURE 6-14. AMPLIFIER ADJUSTMENT HOLES.

FIGURE 6-15. ELECTRONIC COMPONENTS AND SHUTTER CONTROL.

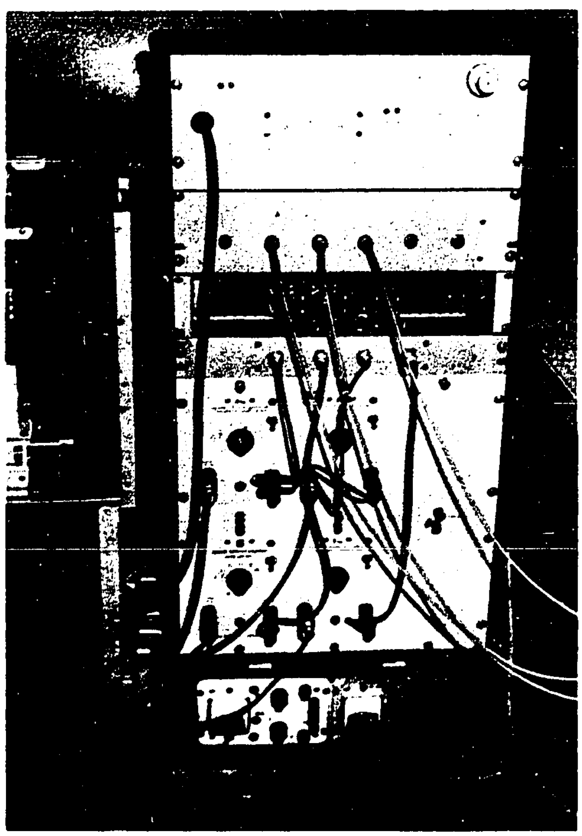

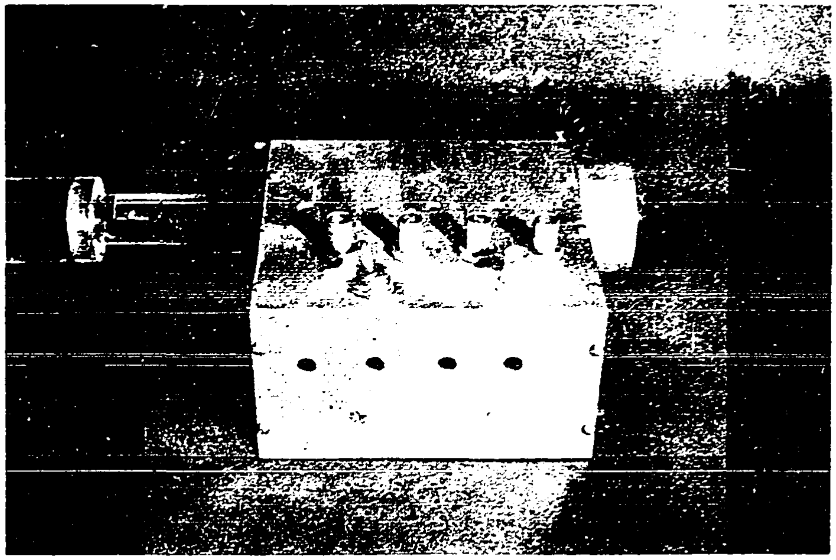

FIGURE 6-14. AMPLIFIER ADJUSTMENT HOLES.

FIGURE 6-15. ELECTRONIC COMPONENTS AND SHUTTER CONTROL.

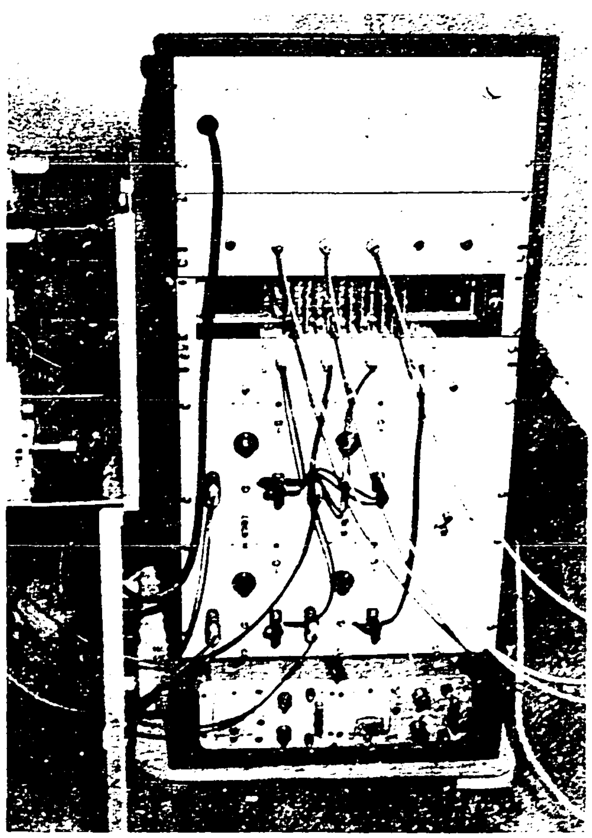

cabinet, are four Keithly Model 102BR amplifiers. Their respective input signals are supplied by coaxial cables from the detectors. After amplification, the signal moves up one level on the rack for signal conditioning. Following this, it goes up another step to where the monostable multivibrators are located for pulse standardization. Interleaved between the monostables are the R-S Flip Flops for the transit time determination. Also, a simple four stage binary counter for signal frequency division is located at this stage. The next level up consists of the filters. From this stage, the filtered signals, together with the frequency information, are fed via coaxial cables to the recorder.

6.4 Operating Instructions

The experimental procedure to carry out a measurement using the Ion Tracer Method will now be given. There are two parts to consider; the one relates to the wind tunnel, and the other to the measuring technique.

6.4.1 The Tunnel Operation

Referring to Figure 6-1, the quick opening valve is closed, the shutoff valve is opened and the vacuum pump turned on. Air in the vacuum tank is thus exhausted. Once the pressure in the tank is reduced to the desired value indicated by a vacuum gauge, the shutoff valve is closed and the vacuum pump turned off. The lower the pressure in the tank, the longer will be the running time, usually it was reduced to near vacuum conditions. The wind tunnel is now operational.

6.4.2 Equipment Operation

All the electronic equipment is switched on and allowed to stabilize. A quick circuit test is carried out by placing a single wire lead from a lKHz rectified sinusoidal source in the test section and monitoring all the resultant voltages on the oscilloscope.

The Po.-210 source is placed into the turbine block and aligned with the slit using the three-dimensional platform. Referring to Figure 6-13, the compressed air supply for the shutter is turned on and adjusted to 60 p.s.i. with the coarse reduction valve. The shutter is now rotating at near the desired speed, as the fine control valve located on the top front panel in the rack cabinet was set previously. Additional adjustments to shutter speed are made during a trial run.

The recorder paper drive is now switched on. The room temperature and pressure are noted. At this stage the experiment is ready to proceed. The final step is to operate the fast opening valve of Figure 6-1, and watch the results.

6.5 Results

In this section there will be reported some results obtained by the method described. It must be emphasized at the outset that considerable improvement could have been realized if the detector mechanism had been better understood. For this reason, these results are presented to show the nature of the results that may be expected and the difficulties encountered, rather than to report a large body of data that has been reliably and accurately measured. Partially to blame was the manner in which most of the work was carried out, channeled in the direction of developing an instrument based on the Ion Tracer Method, rather than the more all inclusive approach associated with an investigation of the method.

While the experimental work was being done, it became apparent that the results could not be considered compatible with the accepted detector theory. The principal suspicion naturally fell on the theory. Normally, unexplained inconsistencies would make the whole technique suspect. However, the results were found to be in reasonably good agreement with those obtained by pressure measurements. It is these that will be presented. There are two separate phases associated with the presentation. The first is the system characterization, and the second is the more specific measurement data.

6.5.1 System Characterization

The detector voltage waveforms taken during the early period of the instrumentation development are shown in Figures 6-16 and 6-17 for the mach 1.8 and 3.0 cases respectively. These are for a 1.5 inch detector probe spacing with a mean distance of 5 inches from the tube inlet. Their general features are typical of all the waveforms independent of probe spacing, whether 1.5, 1.25 or 1 inch, providing the velocity exceeds 500 f.p.s. A major aspect of these waveforms is their negative voltage polarity. Next is the rather broad ill-defined minimum point. The pulse appears to be symmetrical about this minimum, and tends to increase linearly towards the baseline. Near the baseline the increase is considerably slower, giving a wide based pulse. The right hand side is the leading edge, which is faster than the trailing edge. The voltage ripples on the baseline are caused by vibration.

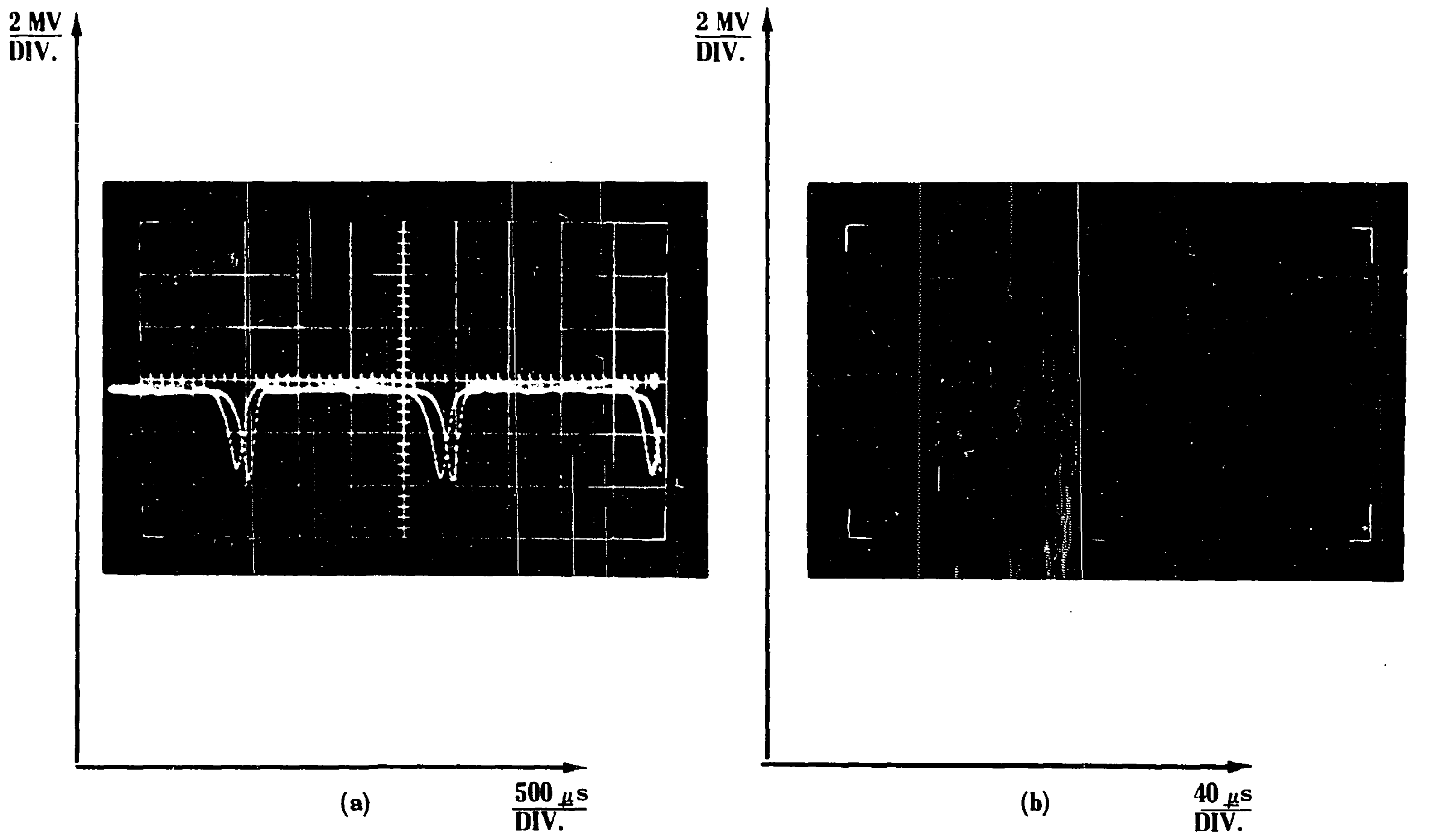

FIGURE 6-16. TYPICAL OUTPUT FROM TWO ADJACENT DETECTORS (M≃1.8).

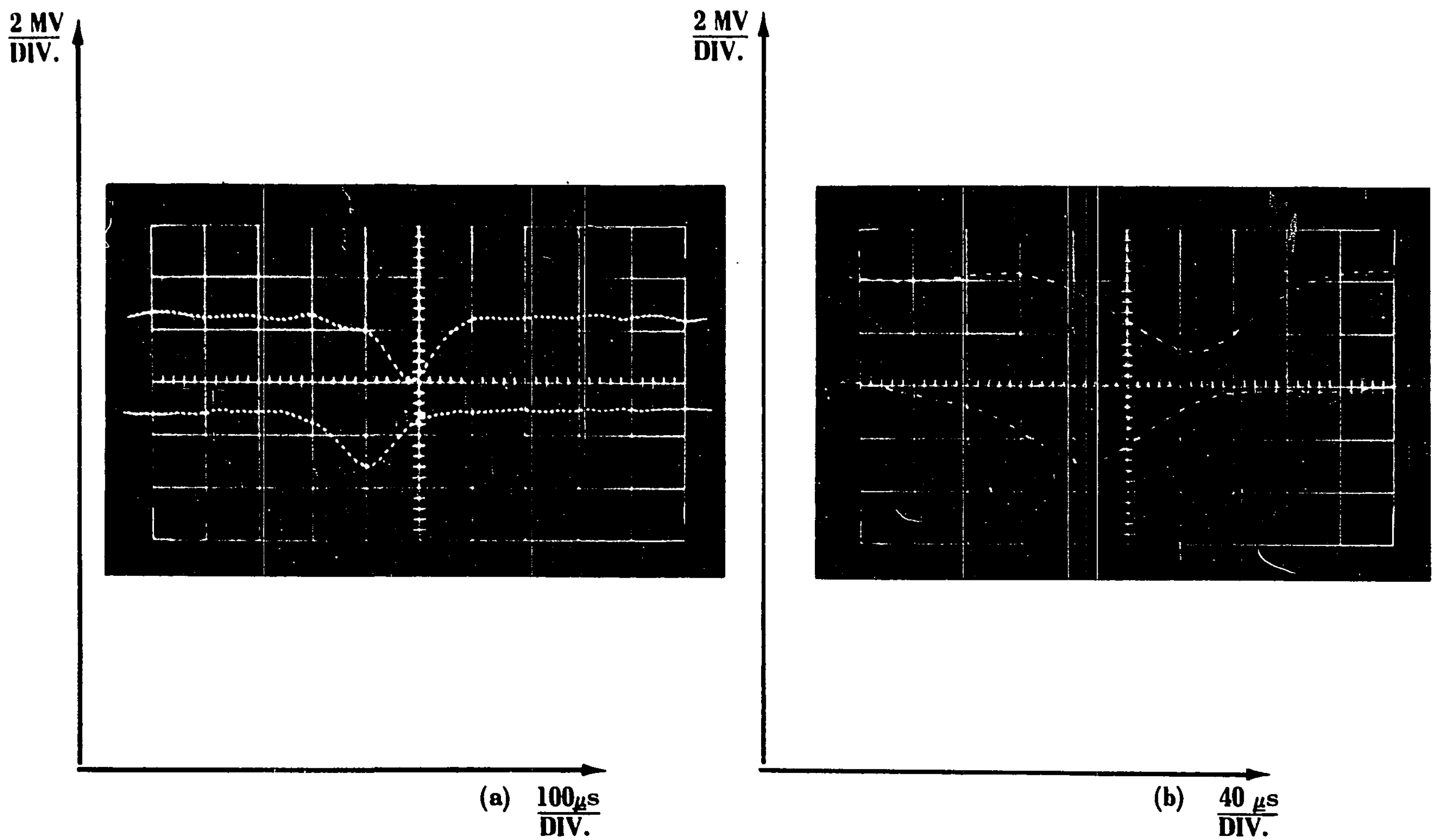

FIGURE 6-17. TYPICAL OUTPUT FROM TWO ADJACENT DETECTORS (M≃3.0).

The overall waveform characteristic shown in Figure 6-16 and Figure 6-17 is in accord with that predicted by the Voltage Model in chapter 4. However, specific differences lie in the magnitudes of the quantities considered. For example, the pulse width is greater than that expected. This wider width can be related to the shutter, which is a rotating one rather than the linear one assumed. That is, the bottom of the slit on the rotating disc gives a longer opening time. The broad minimum can only be due to a more complex detector field pattern, as the expected ion concentration (Figure 2-7) is well represented by the 'cosine' concentration used in the theory. The almost linear portion adjacent to the minimum is as expected. The variation in shutter speed did not affect the quality, only the quantities associated with the waveform, for example, amplitude and width.

The fact that the voltage pulse was negative, together with some additional information as described in chapter 4, led to the re-examination of the detector mechanism. In attempting to resolve the detector problem, an external polarizing source was applied between the probe and ground, as shown in Figure 5-10. The resultant detector waveforms for positive and negative polarizing voltage are shown in Figure 6-18 and Figure 6-19. Figure 6-18 has been touched up to remove some background caused by false triggering of the oscilloscope. These waveforms were taken at subsonic flow and low shutter speed. These conditions were necessary in order to obtain observable signal levels above the noise. The author is unable to explain why in this instance it did not work at supersonic speeds, except to comment that it may rest with either the new lower intensity source, 5 mc., or with the different adjustments to the

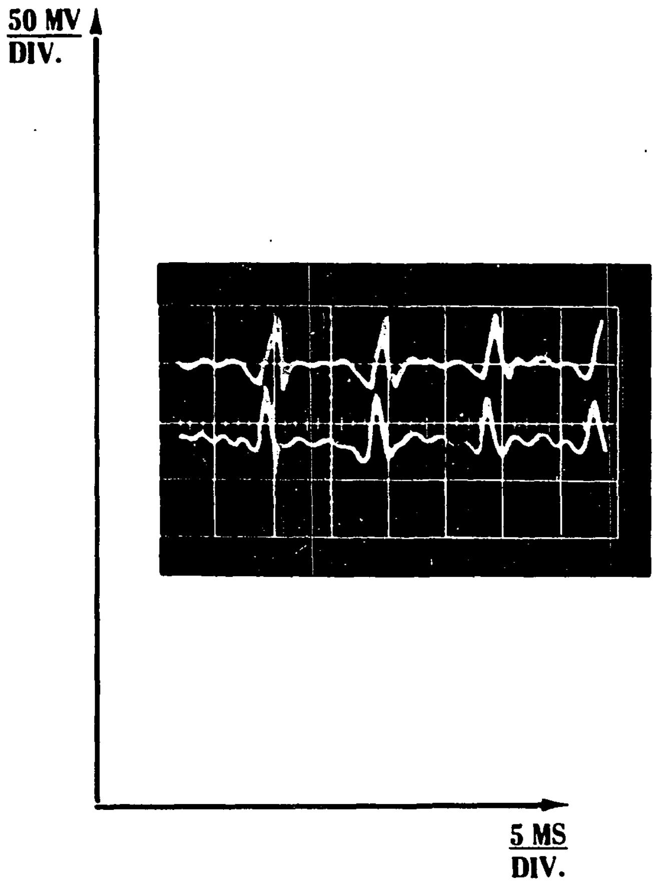

FIGURE 6-18. TYPICAL OUTPUT
(+ 100 V POLARIZING VOLTAGE).

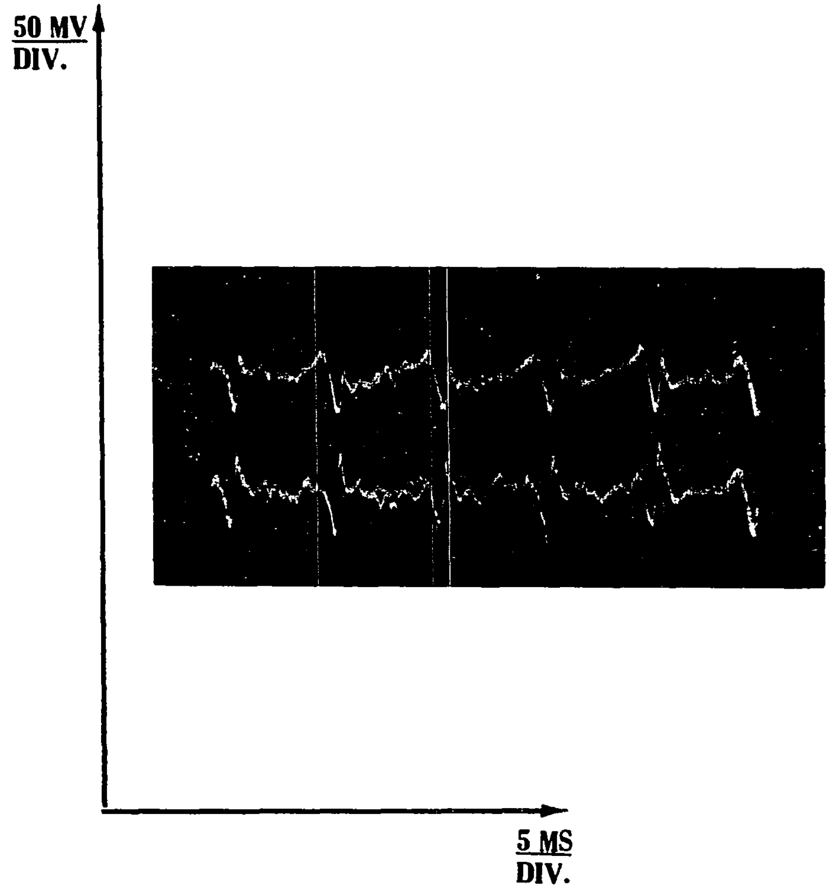

FIGURE 6-19. TYPICAL OUTPUT
(– 100 V POLARIZING VOLTAGE).

'infinite' impedance preamplifier. The source range was checked and found to be ample, however, the intensity could not be checked.

The particular feature worthy of note in these figures is the signal dip (or rise) at both the leading and trailing edge of the pulse. As the flow is speeded up, these dips tend to disappear. This behaviour is identical to that found earlier under similar conditions, except that no external polarizing voltage was used. One could say that if the detector responded to charge that the waveform is indicative of ambipolar diffusion.

Aside from the fact that Figure 6-18 has been 'touched up', positive polarizing voltages gave sharper, less noisy, pulses than the negative ones. The noise was caused by flow conditions and was lowered by reducing the preamplifier input resistance. This was accompanied by a reduction in signal level, requiring readjustment upwards.

The effect of the polarizing voltage amplitude on the signal level was found to be linear. With subsonic flow and a fixed shutter speed, the polarizing voltage was varied between 0 and 100 V.D.C., first for positive voltage and then repeated for negative voltage. The measurements were taken with the oscilloscope and the results are shown in Figure 6-20. Identical flow conditions could not be obtained for the positive and negative polarities, as the flow had been shut off while the polarity was reversed. Thus the slopes shown in Figure 6-20 are different in the first and third quadrant. However, on a normalized scale they would be the same, giving the linear variation of signal level with polarizing voltage.

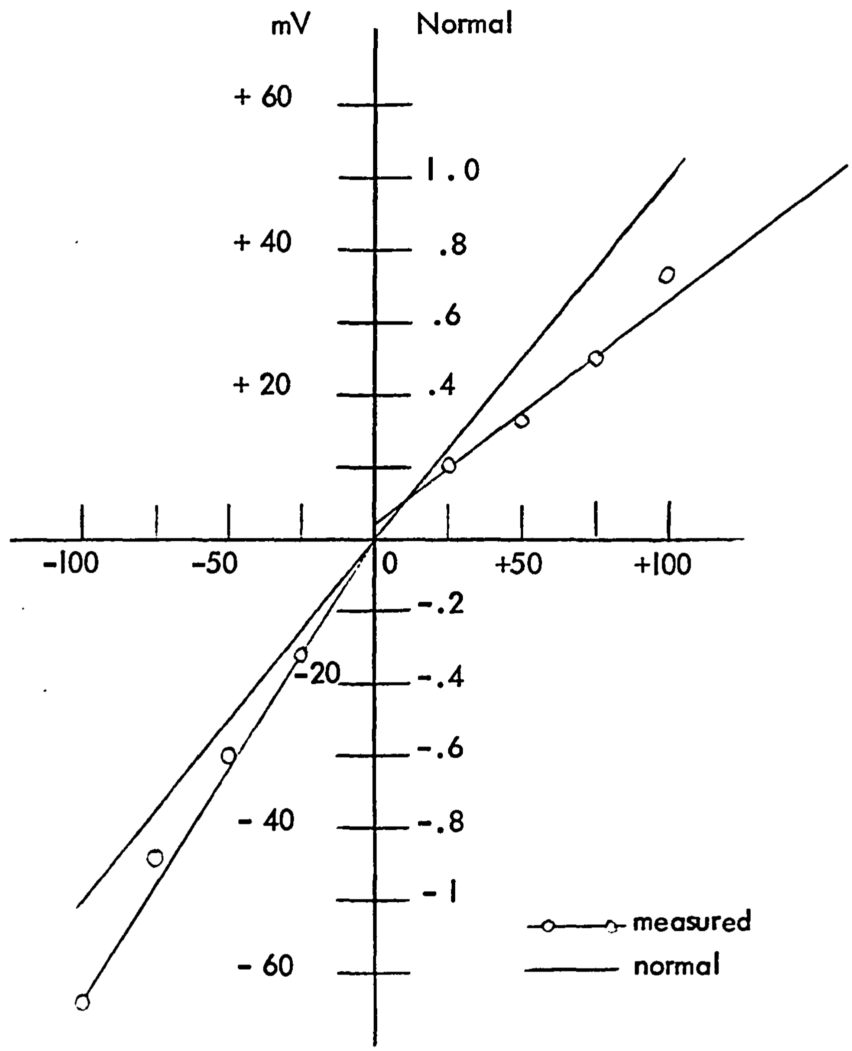

FIGURE 6-20 DETECTOR SIGNAL VARIATION WITH POLARIZING VOLTAGE

The initial data obtained was found to be in considerable disagreement with the pressure deduced velocities. This is illustrated in Figure 6-16 and Figure 6-17. It was discovered that the major share was contributed by the oscilloscope used in the measurements, which had an inaccurate time base calibration. Thereafter, this calibration was carefully maintained. It was also noted that the most reliable and reproduceable data was taken at the beginning of a run. There still remained approximately a 5% discrepancy for which an error analysis was developed. Unfortunately, in the end this analysis proved to be incorrect.

6.5.2 Data

It was intended to take the final data for presentation after all the encountered difficulties were eliminated. The detector mechanism had been a major problem, and to a minor extent, the recorder resolution. The recorder was replaceable. Unfortunately, the actual portrayal of the expected results did not materialize. The Po-210 source was too low an intensity. It is well to mention that this final 5 mc. source was expected to be more than ample as there was supposedly a better understanding of the detector mechanism. Thus the results are sparse and leave much to be desired.

The velocities measured with the Ion Tracer Technique are shown in Figure 6-21 and Figure 6-22. These are computed from the transit time measurements taken directly with the oscilloscope. Figure 6-21 is for the 1.5 inch probe

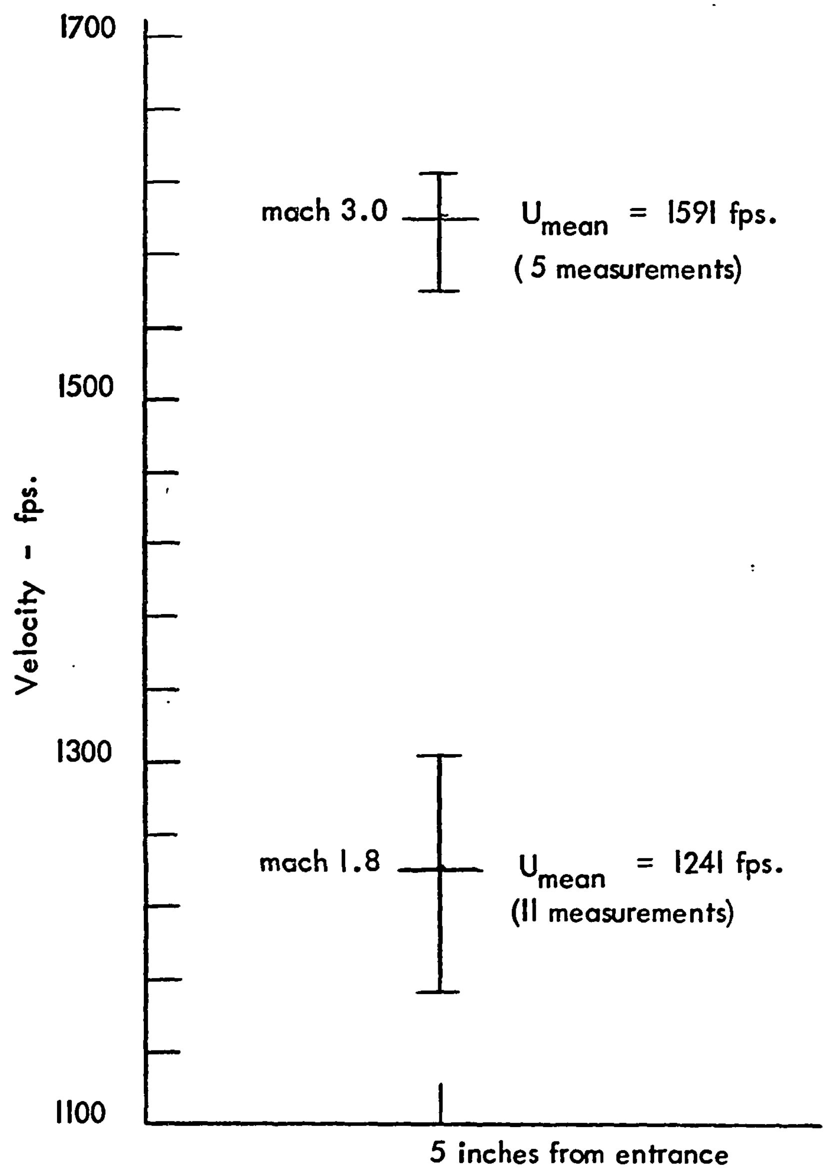

FIGURE 6-21 VELOCITY MEASUREMENT - 1.5 inch probe spacing

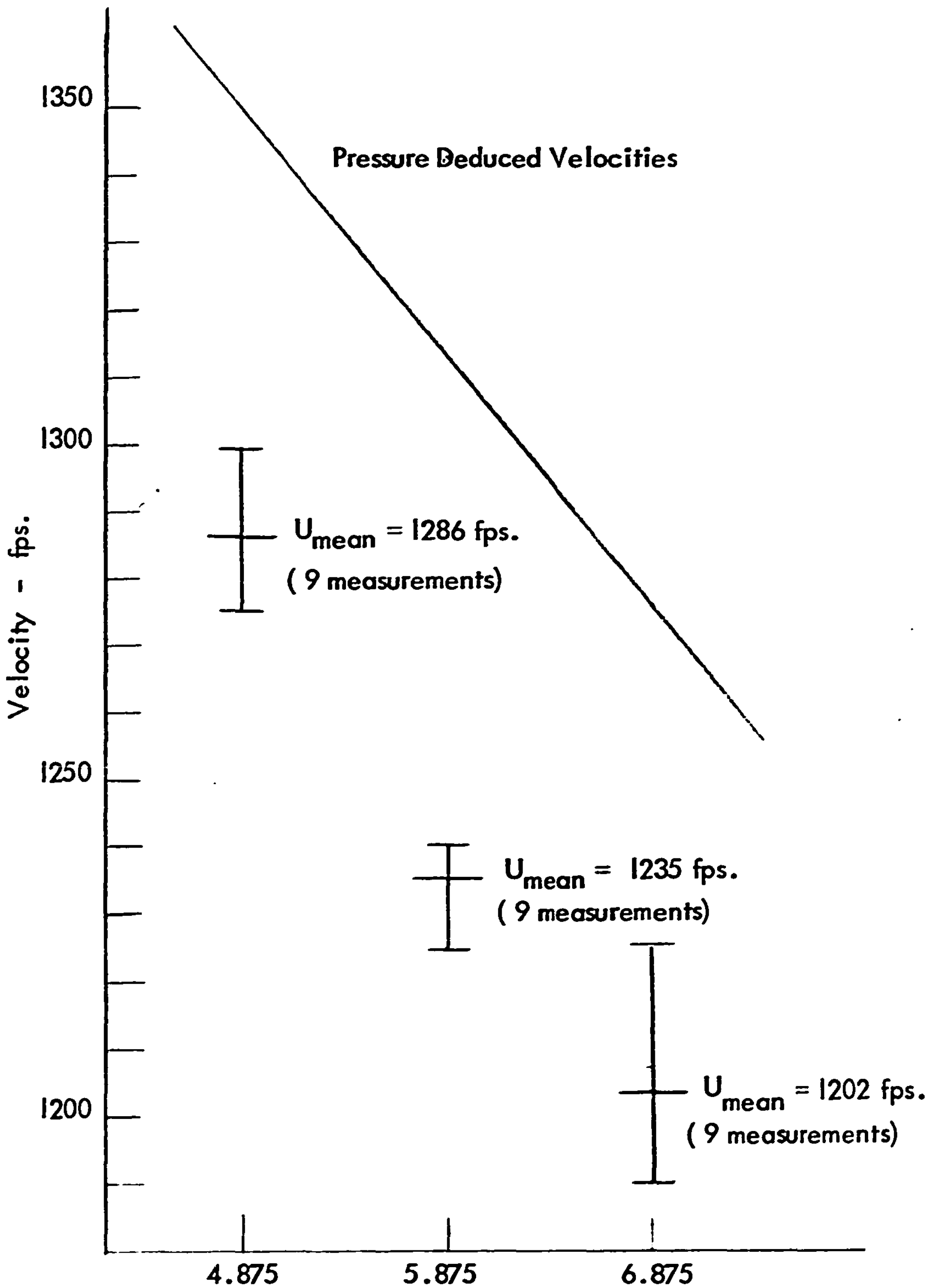

FIGURE 6-22 LONGITUDINAL VELOCITY MEASUREMENTS - mach 1.8

spacing located a mean distance of 5 inches from the tube inlet plane, and illustrates the spread in measurements for the mach 1.8 and 3.0 cases. Comparing the mean measured velocities in Figure 6-21 with the pressure deduced velocities, results in a discrepancy of 7.7 % and 1.3% for the mach 1.8 and 3.0 cases respectively. There is little confidence in the mach 3.0 case . Figure 6-22 shows the results obtained in three adjacent regions using 1 inch probe spacing and the mach 1.8 nozzle. This data was taken under similar conditions, that is, during the initial period of a run. Hence the difference between the mean measured and pressure deduced velocities lies between 5% and 6%. The data shown in both Figure 6-21 and Figure 6-22 has not been standardized to any ambient temperature, however, any deviation due to this should not exceed 2%.

6.5.3 Conclusion

As mentioned previously, the expected results to be used for publication did not materialize with the new 5 m.c. Po-210 source. The choice of a 5 m.c. source was based upon a desire to use as low a source density as possible, yet sufficient for the measurements. The low density specification was set in order to reduce the possibility of source leakage, prevalent at higher densities, with its attendent hazards. In addition, the assumed better understanding of the detection mechanism supported this supposition. Prior to ordering this last source, the supplier, The Radio Chemical Center, in the United Kingdom, as well as others, had stopped production of Po-210 due to its unsafe nature. A special appeal had to be made to obtain this source, which in the end proved inadequate.

However, in spite of this above-mentioned setback, the earlier results proved the measurement technique to be good. The existing discrepancy in relation to the pressure deduced velocities stands unresolved, whether fundamental to the measurement technique or arising from the static wall pressure measurements. The ion tracer technique gives a continuous measurement of the average velocity under dynamic conditions.

CHAPTER VII

CONCLUSION

An instrumentation technique has been presented for the continuous measurement of supersonic air velocities. The method involved the periodic production of an ion density distribution as a tracer element in the air stream. The ion tracer was detected by induction external to the flow boundary, thus the transit time between two fixed positions downstream is determined by a pulse width modulation technique. All the pertinent details of the method are given.

The thesis has demonstrated that ions produced by alpha particles from Po-210 are suitable tracers for measuring supersonic velocities. It was shown that the ions are unaffected by diffusion and recombination for the times under consideration. However, they are affected by an electric field which separates the ions of opposite sign, rendering them detectable. The detection system is particularly suitable; its output signal is directly proportional to the ion density present and the magnitude of the polarizing voltage, and its output is in synchronism with the ion densities. The intrinsic errors in the method were shown to be negligible. The errors incurred are measurement errors per se.

Since Po-210 is no longer available as a source for creating ions, it is imperative to look for an alternative. There are other radioactive alpha emitters available, however, one should look beyond these to the laser. The laser offers advantages aside from the safety features. One is the small localized volume ionization enabling the velocity measurement of a particular streamline, not possible with a radioactive source. Thus the entire cross-section velocity profile could be measured. Additionally, it would generate sharper ion pulses with a much better frequency stability. It is therefore recommended that any future work involved in the measurement of supersonic speeds utilize the laser device.

APPENDIX I

DETERMINATION OF ION CONCENTRATION

The problem is to determine the ion concentration in air. Effectively, this reduces to calculating the total number of alpha particles impinging upon any element of air during its exposure to the beam. The ion concentration is then determined by a scale change given by the number of ions produced per alpha particle.

In the absence of the shutter, the beam intensity along the axis in the air stream is that shown in Figure A.I-I. This characteristic was computed using the configuration shown in Figure A.I-2. The assumptions were that the source, I, can be subdivided into elemental sources Idz/a and each source emits alpha particles isotropically. Thus the number of alpha particles per second impinging upon the element dz at z is

$$I(z) = \frac{Idz}{4\pi aL}\left(\frac{z}{\sqrt{1+(z/2L)^2}} + \frac{a-z}{\sqrt{1+(\overline{a-z}/2L)^2}}\right) \qquad \frac{a}{2} < z < a \quad \text{(A.I-Ia)}$$

$$= \frac{Idz}{4\pi aL}\left(\frac{z}{\sqrt{1+(z/2L)^2}} - \frac{2(z-a)}{\sqrt{1+(\overline{z-a}/L)^2}}\right) \qquad a < z < 2a \quad \text{(A.I-Ib)}$$

and $z = a/2$ is the symmetry axis. These expressions reduce to

$$I(z) \approx \frac{I dz}{4 \pi L} \qquad \frac{a}{2} < z < a \qquad \text{(A.1-2a)}$$

$$\approx \frac{I dz}{4 \pi La} (2a - z) \qquad a < z < 2a \qquad \text{(A.1-2b)}$$

as $(z/2L)^2$, $(\overline{a - z}/2L)^2$, $(\overline{z - a}/L)^2 << 1$. Equation A.1-2 is the characteristic displayed in Figure A.1-2.

The intensity characteristic is altered both in magnitude and width during the time the source is being interrupted. The interrupter is assumed to move with uniform velocity U_s and to be in such close proximity that its only effect is to expose the source. With these conditions the intensity at time t_1 is

$$I(z, t_1) = \frac{I U_s t_1}{4 \pi La} dz \qquad a - \frac{U_s t_1}{2} < z < 2a - U_s t_1 \text{ (A.1-3a)}$$

$$= \frac{I dz}{4 \pi L} (2a - z) \qquad 2a - U_s t_1 < z < 2a \qquad \text{(A.1-3b)}$$

$$0 < U_s t_1 < a$$

Each alpha particle incident on the flowing air produces M_o ions per unit volume per unit path length. These ions being an integral part of the air move with the air velocity U. Therefore, the ion concentration generated at t_1 and moving with velocity U is

$$n(z, t_1) = \frac{M_o I dz}{4\pi L a} \begin{cases} u(z + (U+U_s)t_1 - Ut)\ (z + (U+U_s)t_1 - Ut) \\ -u(z + Ut_1 - Ut)\ (z + Ut_1 - Ut) \\ -u(z - 2a + (U+U_s)t_1 - Ut)\ (z - 2a + (U+U_s)t_1 - Ut) \\ +u(z - 2a + Ut_1 - Ut)\ (z - 2a + Ut_1 - Ut) \end{cases}$$

$$0 < t_1 < t$$

The ion concentration as a function of position is

$$n(z) = \int_0^{t_1} n(z, t_1)\ dt_1$$

Carrying out the integration, the result is

$$n(z) = \frac{M_o I dz T_e}{4\pi L \quad K(K+1)} \begin{cases} 2K - .25 - z^2/a^2 & 0 < z < a/2 \\ 0.5\,(.25\,(16K - 1) - z/a - z^2/a^2) & a/2 < z < (3/2)\,a \\ 2\,(K + .5 - z/a) & 1.5a < z < (K-.5)\,a \\ 0.5\,(K + 1.5 - z/a)^2 & (K-0.5)a < z < (K+1.5)\,a \end{cases}$$

$$T_e = \frac{a}{U_s}, \quad K = \frac{U}{U_s}$$

$n(z)$ is plotted in Figure 2-7 for several values of the parameter K.

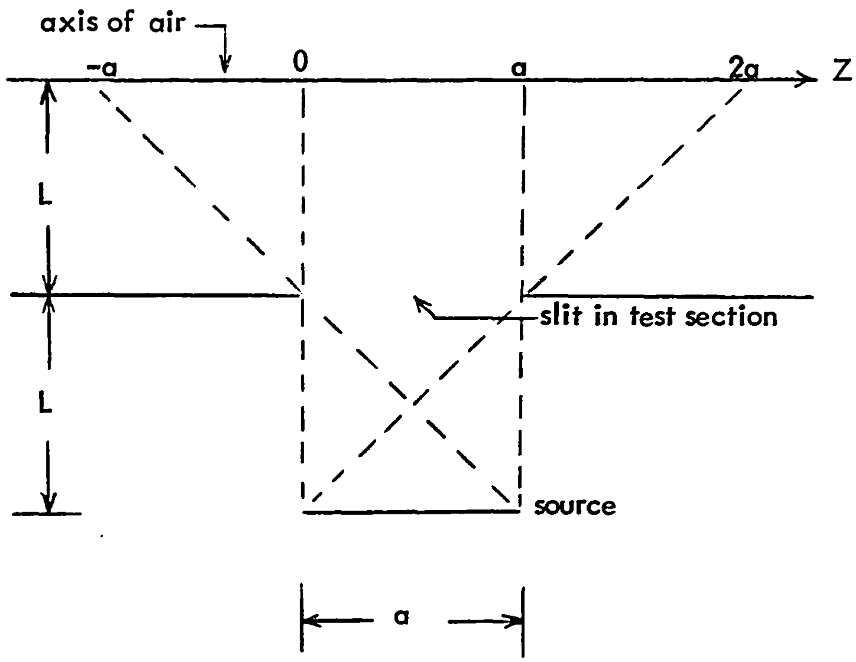

FIGURE A.1-1 CONFIGURATION TO COMPUTE INTENSITY IN AIR

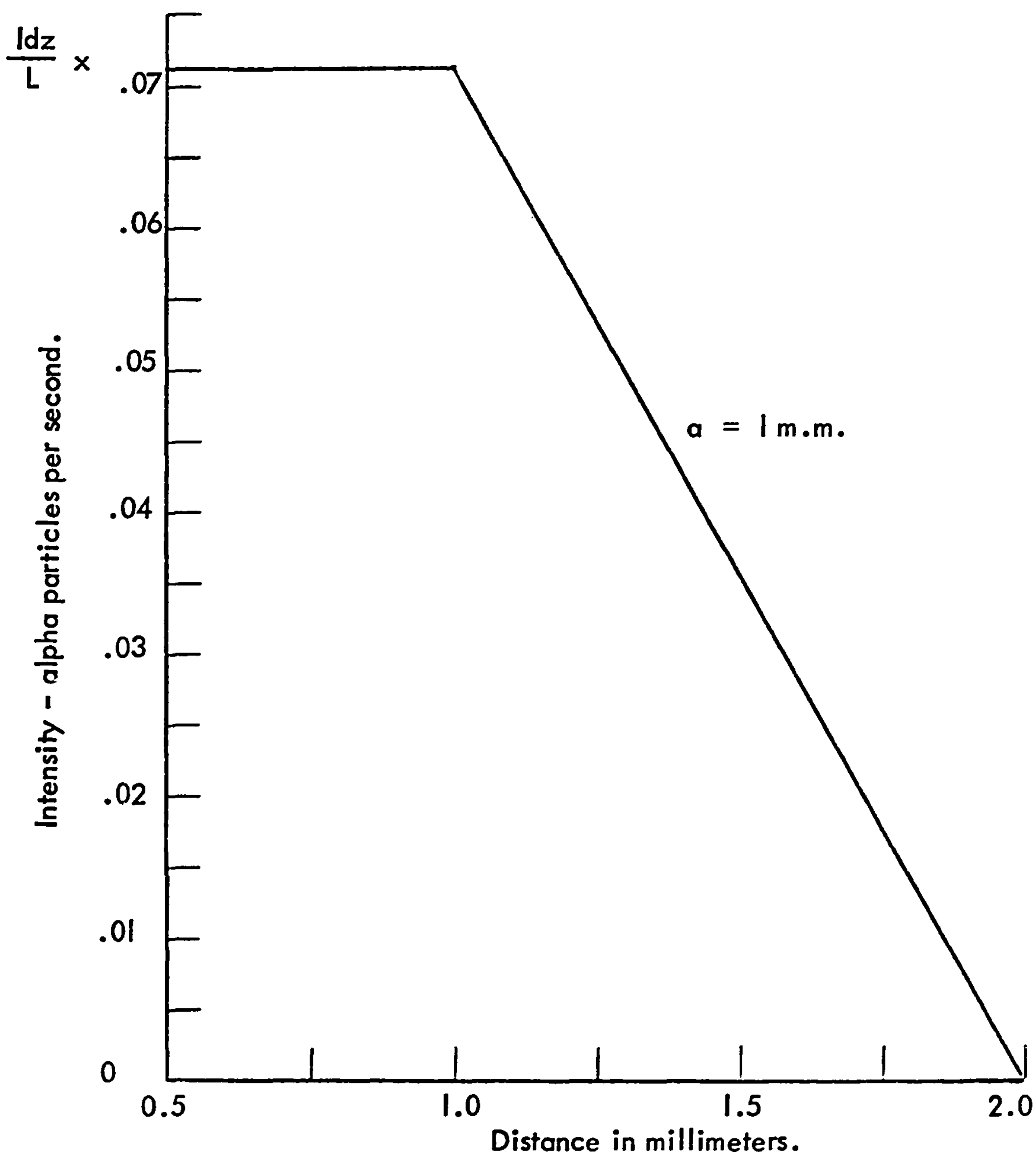

FIGURE AI - 2 INTENSITY CHARACTERISTIC

APPENDIX II

THE EFFECT OF A VELOCITY FIELD

This section examines the measurement errors caused by a longitudinal variation in velocity.

Assume the ion concentration n,

$$n(z) = \frac{M_o}{\sqrt{\pi b^2}} \exp - \left(\frac{z}{b}\right)^2 \qquad (A.2\text{-}1)$$

is centered about the first detector ($z = 0$), and this signifies $t = 0$. M_o is the number of ions per unit depth and b is a measure of the distribution width. Let the velocity variation in the flow direction be linear and given by

$$U = \frac{dz}{dt} = U_o - Hz \qquad (A.2\text{-}2)$$

where U_o is the velocity at $z = 0$ and H is the change in velocity per unit length.

Equation A.2-2 has the solution

$$z = z_1 \exp - (Ht) + \frac{U_o}{H} (1 - \exp -(Ht)) \qquad (A.2\text{-}3)$$

z is the position at time $t = t$ of a particle which started from z_1 at time $t = 0$. Thus the position of the maximum ion concentration at any time t is

$$z_p = \frac{U_o}{H} (1 - \exp -(Ht)) \qquad (A.2-4)$$

This peak concentration moves a distance L in a time T to reach the second detector. The resultant average velocity is U_M

$$U_M = \frac{L}{T} = \frac{U_o}{TH} (1 - \exp - (HT)) \qquad (A.2-5)$$

A.2-5 is valid providing the relative position of the peak concentration remains fixed in spite of velocity modulation during the transport time.

The effect of velocity modulation on the concentration is determined from particle conservation, that is,

$$n_1 \, d z_1 = ndz \qquad (A.2-6)$$

Utilizing A.2-2, A.2-3, A.2-5 and A.2-6, shifting the coordinate reference to the second detector and some algebraic manipulation including neglecting terms $O\left\{ \left(\frac{H}{U_o}\right)^2, \ (HT)^2, \ z^2 \right\}$ and higher, the new ion concentration is

$$n(z) = \frac{M_o}{\sqrt{\pi b^2}} \left(1 + \frac{HL}{U_o} \right) \left(1 - z \frac{H^2 T}{U_o} \right) \exp - \left(\frac{z}{b} \right)^2 \qquad (A.2-7)$$

The maximum concentration from A.2-7 is located at

$$z = - \frac{H^2 T b^2}{2 U_o} \qquad (A.2-8)$$

For the experimental values $H = 35$ f.p.s./in., $T = 70\ \mu s$, $b = 0.25$ in. and $U_o = 1300$ f.p.s., z is -2.5×10^{-5} inch, which is negligible.

The second source of error relates to the difference between time and space average velocities. The space average from A.2-2 is

$$U_A = U_o - \frac{HL}{2} \tag{A.2-9}$$

Replacing U_o and L in terms of U_M from A.2-5 gives

$$U_A = U_M TH \left(\left(1 - \exp - (HT) \right)^{-1} - \tfrac{1}{2} \right) \tag{A.2-10}$$

Substituting the first three terms of the series for the exponential gives

$$U_A = U_M \left(\left(1 - HT/2\right)^{-1} - HT/2 \right) \tag{A.2-11}$$

Expanding $(1 - HT/2)^{-1}$ and again retaining only the first three terms leads to

$$U_A = U_M \left(1 + (HT/2)^2 \right)$$

$$U_A \simeq U_M$$

as HT is small.

APPENDIX III

EVALUATION OF CONSTANTS

A.3.1 To show $\beta \gg \alpha_e n_i$

β the fraction of electrons lost by attachment per unit time according to (12) is

$$\beta = \varphi f_{co} \left(\frac{\rho}{\rho_o}\right) \left(\frac{T}{T_o}\right)^{\frac{1}{2}} \qquad \text{(A.3-1)}$$

where f_{co} is the electron collision frequency at known conditions, φ is the attachment probability per collision, ρ_o and T_o are the density and temperature at known conditions ρ and T their values at test conditions. Thus,

$$\beta = 5 \times 10^{-6} \times 2.15 \times 10^{11} \times 0.3557 \times 0.66138^{\frac{1}{2}}$$

$$= 3.11 \times 10^{5} \text{ per sec.}$$

The maximum value of $\alpha_e = 10^{-7}$ cm.^{3}/ (ion . sec.) and the maximum value of $n_i = 1.36 \times 10^{8}$ ions/cm.^{3} , which yields $\alpha_e n_i = 13.6 \ll \beta = 3.11 \times 10^{5}$.

A.3.2 Evaluation D_e, D_+ and D_-

According to Loeb[43] the diffusion coefficient varies inversely with density and directly with the square root of absolute temperature. Therefore, the coefficient may be written as

$$D = D_o \left(\frac{\rho_o}{\rho}\right) \left(\frac{T}{T_o}\right)^{\frac{1}{2}}$$

where the subscript o refers to known conditions.

D_e at 0°C. and 760 mm. is 200 cm.^{2}/sec. At test conditions

$$D_e = 200 \times \left(\frac{530.7}{491.7}\right)^{\frac{1}{2}} \left(\frac{1}{.35573}\right) (.66138)^{\frac{1}{2}}$$

$$= 477 \text{ cm.}^2/\text{sec.}$$

$$D_+ = .029 \left(\frac{1}{.35573}\right) (.66138)^{\frac{1}{2}}$$

$$= 0.0663 \text{ cm.}^2/\text{sec.}$$

$$D_- = .0434 \left(\frac{1}{.35573}\right) (.66138)^{\frac{1}{2}}$$

$$= 0.0995 \text{ cm.}^2/\text{sec.}$$

REFERENCES

(1) Volluz, R.J., Wind Tunnel Instrumentation and Operation, Section 20, Handbook of Supersonic Aerodynamics Naval Report 1488 (Vol. 6), A Bureau of Naval Weapons Publication.

(2) Cady, W.M., Physical Measurements in Gas Dynamics and Combustion Vol. IX, High Speed Aerodynamics and Jet Propulsion, Princton University Press.

(3) Dean, R.C. Jr., Aerodynamic Measurements, Gas Turbine Laboratory, - Massachusetts Institute of Technology 1959.

(4) Lilley, G.M. and Morton, D., The Response Time of Wind Tunnel Pressure Measuring Systems; The College of Aeronautics Cranfield COA Report No. 141 , Nov. 1960.

(5) Markovin, M.V., Fluctuations and Hot Wire Anemometry in Compressible Flows, London 1956, Agardograph No.24.

(6) Boyd, B., Dorsch, R.G., and Brodie, True Airspeed Measurement by Ionization Tracer Technique, NACA Research Memo E 52C31, Lewis Flight Propulsion Laboratory, Cleveland, Ohio, 1952.

(7) Mellen, G.L., Gas Flow Speedometer, Electronics, Vol.23, No.2, Feb. 1950, p.80.

(8) Lawrence, R.B., Measurement of Gas Velocity by a Pulsed Ionization Technique, Final Report to ONR from the National Research Corporation, Contract N 70nr - 478, 1951.

(9) Lilienfeld, P., Solon, L.R., and Di Giovanni, H.J., Ion Tracer Anemometer for the Measurement of Low Density Air Flow, Review Scientific Instruments, Vol. 38, No.3, Mar. 1967.

(10) Kunkel, W.B., and Talbot, L.M., Ion Tracer Technique for Air Speed Measurements at Low Densities, University of California, Institute of Engineering Research, Berkeley Cal., Series 19, Issue 8, Feb. 20, 1953, Report HE - 150-95.

(11) Cooley, W.C., and Stever, H.G., Determination of Air Velocity by an Ion Transit Time Measurement, Review Scientific Instruments, Vol.23, No. 4, April 1952.

(12) Cooley, W.C., Measurement of Supersonic Velocities by Ion Transit Time Methods, May 1951, D.Sc. Thesis submitted to Mechanical Engineering Department, M.I.T.

(13) Wright, F.H., A Method of Measuring the Rate of Ion Diffusion in a Turbulent Air Stream, Ph.D. Thesis, California Institute of Technology, 1948.

(14) Jesse, W.P., Forstat, H., and Sadauskis, J., The Ionization in Argon and in Air by Single Alpha-Particles as a Function of their Energy, Physics Review, Vol. 77, No. 6, March 1950.

(15) Perlman, I., Ghiorso, A., Seaborg, G.T., Systematics of Alpha-Radioactivity, Physics Review, Vol. 77, No.1, Jan. 1950.

(16) Bagnall, K.W., Polonium, Endeavour, Vol. XXII, No. 86, May 1963.

(17) Bagnall, K.W., Chemistry of the Rare Radioelements, Butterworths, London 1957.

(18) Rossi and Ellis, Dosimetry of Thin Polonium Sources, Neucleonics 7, 21 Sept. 1950.

(19) Hoag, J.B., and Korff, S.A., Electron and Nuclear Physics, Third Edition, D. Van Nostrand Company, New York, 1948.

(20) Kaplan, I., Nuclear Physics, Addison - Wesley, 1955.

(21) Rutherford, Chadwick and Ellis, Radiations from Radioactive Substances, Cambridge University Press, 1930.

(22) Jaffe, G., Zur Theorie der Ionization in Kolonnen, Annalen der Physik 42, 303, 1913.

(23) Jaffe, G. , On the Joint Action of Diffusion and Recombination of Ions, Physics Review, Vol. 59, April 1941.

(24) Engel, A. Von, Ionized Gases, Second Edition, Oxford Clarendon Press, 1965.

(25) Cambel, A.B., Plasma Physics and Magetofluidmechanics, McGraw Hill, 1963.

(26) Spitzer, L., Physics of Fully Ionized Gases, Interscience, New York, 1966.

(27) Delcroix, J.L., Introduction to the Theory of Ionized Gases, Interscience, 1960.

(28) Wilhelm, H.E., Non-Collective Motion of Electrons and Ions in an Electric Field, Int. J. Electronics, 1970, Vol.28, No.3.

(29) Hamilton, D.R., Knipp, J.K. and Kuper, J.B., Klystrons and Microwave Triodes, Vol. 7, M.I.T. Radiation Laboratory Series, McGraw Hill, 1948.

(30) Pierce, J.R., Travelling Wave Tubes, D. Van Nostrand, 1950.

(31) Farnell, G.W., Microwave Amplifiers and Oscillators, Unpublished Notes, Mc Gill University.

(32) Jackson, J.D., Classical Electrodynamics, John Wiley and Sons Inc., 1962.

(33) Rowe, J.E., Nonlinear Electron Wave Interaction Phenomenon, Academic Press, 1965.

(34) Cermak, I.A., Solution of Unbounded Field Problems, Ph.D. Thesis, Mc Gill University, March 1969.

(35) Guld, C., Cathode Follower and Negative Capacitance as High Input Impedance Circuits, Proc. IRE, Vol. 50, Sept. 1962.

(36) Crawford, R.H., High Input Impedance Techniques for Transistor Circuits, Texas Instruments Application Report, Aug. 1962.

(37) Thornton et al, Multistage Transistor Circuits, Vol. 5, SEEC. Series, John Wiley and Sons Inc., 1965.

(38) Black, H.S., Modulation Theory, D. Van Nostrand Co. Inc., Aug. 1953.

(39) Panter, P.F., Modulation, Noise and Spectral Analysis Applied to Information Transmission, Mc Graw Hill, 1965.

(40) Liepmann, H.W. and Roshko, A., Elements of Gas Dynamics, John Wiley and Sons, 1957.

(41) Shapiro, A.H., The Dynamics and Thermodynamics of Compressable Fluid Flow, Vol. I, Ronald Press Company, 1953.

(42) Keenan, H.H. and Kaye, J., Gas Tables, John Wiley and Sons, May 1960.

(43) Loeb, L.B., Basic Processes of Gaseous Electronics, University of California Press, 1961.